The Development of Active Integrated Antennas and a Design Methodology

By
David J. Roscoe

A Thesis

Submitted to the Faculty of Graduate Studies

In Partial Fulfillment of the Requirements for the Degree of

Doctor of Philosophy in Electrical Engineering

University of Manitoba

Department of Electrical and Computer Engineering

Winnipeg, Manitoba

Canada

June, 1993

ISBN 0-315-86119-3

Canada

Name DAVID J. ROSCOE ("THE DEVELOPMENT OF ACTIVE INTEGRATED ANTENNAS AND A DESIGN METHODOLOGY")

Dissertation Abstracts International is arranged by broad, general subject categories. Please select the one subject which most nearly describes the content of your dissertation. Enter the corresponding four-digit code in the spaces provided.

ELECTRONICS AND ELECTRICAL — SUBJECT TERM

0544 — SUBJECT CODE

U·M·I

Subject Categories

THE HUMANITIES AND SOCIAL SCIENCES

COMMUNICATIONS AND THE ARTS
Architecture 0729
Art History 0377
Cinema 0900
Dance 0378
Fine Arts 0357
Information Science 0723
Journalism 0391
Library Science 0399
Mass Communications 0708
Music 0413
Speech Communication 0459
Theater 0465

EDUCATION
General 0515
Administration 0514
Adult and Continuing 0516
Agricultural 0517
Art 0273
Bilingual and Multicultural 0282
Business 0688
Community College 0275
Curriculum and Instruction 0727
Early Childhood 0518
Elementary 0524
Finance 0277
Guidance and Counseling 0519
Health 0680
Higher 0745
History of 0520
Home Economics 0278
Industrial 0521
Language and Literature 0279
Mathematics 0280
Music 0522
Philosophy of 0998
Physical 0523
Psychology 0525
Reading 0535
Religious 0527
Sciences 0714
Secondary 0533
Social Sciences 0534
Sociology of 0340
Special 0529
Teacher Training 0530
Technology 0710
Tests and Measurements 0288
Vocational 0747

LANGUAGE, LITERATURE AND LINGUISTICS
Language
- General 0679
- Ancient 0289
- Linguistics 0290
- Modern 0291

Literature
- General 0401
- Classical 0294
- Comparative 0295
- Medieval 0297
- Modern 0298
- African 0316
- American 0591
- Asian 0305
- Canadian (English) 0352
- Canadian (French) 0355
- English 0593
- Germanic 0311
- Latin American 0312
- Middle Eastern 0315
- Romance 0313
- Slavic and East European 0314

PHILOSOPHY, RELIGION AND THEOLOGY
Philosophy 0422
Religion
- General 0318
- Biblical Studies 0321
- Clergy 0319
- History of 0320
- Philosophy of 0322

Theology 0469

SOCIAL SCIENCES
American Studies 0323
Anthropology
- Archaeology 0324
- Cultural 0326
- Physical 0327

Business Administration
- General 0310
- Accounting 0272
- Banking 0770
- Management 0454
- Marketing 0338

Canadian Studies 0385
Economics
- General 0501
- Agricultural 0503
- Commerce-Business 0505
- Finance 0508
- History 0509
- Labor 0510
- Theory 0511

Folklore 0358
Geography 0366
Gerontology 0351
History
- General 0578
- Ancient 0579
- Medieval 0581
- Modern 0582
- Black 0328
- African 0331
- Asia, Australia and Oceania 0332
- Canadian 0334
- European 0335
- Latin American 0336
- Middle Eastern 0333
- United States 0337

History of Science 0585
Law 0398
Political Science
- General 0615
- International Law and Relations 0616
- Public Administration 0617

Recreation 0814
Social Work 0452
Sociology
- General 0626
- Criminology and Penology ... 0627
- Demography 0938
- Ethnic and Racial Studies 0631
- Individual and Family Studies 0628
- Industrial and Labor Relations 0629
- Public and Social Welfare 0630
- Social Structure and Development 0700
- Theory and Methods 0344

Transportation 0709
Urban and Regional Planning 0999
Women's Studies 0453

THE SCIENCES AND ENGINEERING

BIOLOGICAL SCIENCES
Agriculture
- General 0473
- Agronomy 0285
- Animal Culture and Nutrition 0475
- Animal Pathology 0476
- Food Science and Technology 0359
- Forestry and Wildlife 0478
- Plant Culture 0479
- Plant Pathology 0480
- Plant Physiology 0817
- Range Management 0777
- Wood Technology 0746

Biology
- General 0306
- Anatomy 0287
- Biostatistics 0308
- Botany 0309
- Cell 0379
- Ecology 0329
- Entomology 0353
- Genetics 0369
- Limnology 0793
- Microbiology 0410
- Molecular 0307
- Neuroscience 0317
- Oceanography 0416
- Physiology 0433
- Radiation 0821
- Veterinary Science 0778
- Zoology 0472

Biophysics
- General 0786
- Medical 0760

EARTH SCIENCES
Biogeochemistry 0425
Geochemistry 0996
Geodesy 0370
Geology 0372
Geophysics 0373
Hydrology 0388
Mineralogy 0411
Paleobotany 0345
Paleoecology 0426
Paleontology 0418
Paleozoology 0985
Palynology 0427
Physical Geography 0368
Physical Oceanography 0415

HEALTH AND ENVIRONMENTAL SCIENCES
Environmental Sciences 0768
Health Sciences
- General 0566
- Audiology 0300
- Chemotherapy 0992
- Dentistry 0567
- Education 0350
- Hospital Management 0769
- Human Development 0758
- Immunology 0982
- Medicine and Surgery 0564
- Mental Health 0347
- Nursing 0569
- Nutrition 0570
- Obstetrics and Gynecology .. 0380
- Occupational Health and Therapy 0354
- Ophthalmology 0381
- Pathology 0571
- Pharmacology 0419
- Pharmacy 0572
- Physical Therapy 0382
- Public Health 0573
- Radiology 0574
- Recreation 0575
- Speech Pathology 0460
- Toxicology 0383

Home Economics 0386

PHYSICAL SCIENCES
Pure Sciences
Chemistry
- General 0485
- Agricultural 0749
- Analytical 0486
- Biochemistry 0487
- Inorganic 0488
- Nuclear 0738
- Organic 0490
- Pharmaceutical 0491
- Physical 0494
- Polymer 0495
- Radiation 0754

Mathematics 0405
Physics
- General 0605
- Acoustics 0986
- Astronomy and Astrophysics 0606
- Atmospheric Science 0608
- Atomic 0748
- Electronics and Electricity 0607
- Elementary Particles and High Energy 0798
- Fluid and Plasma 0759
- Molecular 0609
- Nuclear 0610
- Optics 0752
- Radiation 0756
- Solid State 0611

Statistics 0463

Applied Sciences
Applied Mechanics 0346
Computer Science 0984
Engineering
- General 0537
- Aerospace 0538
- Agricultural 0539
- Automotive 0540
- Biomedical 0541
- Chemical 0542
- Civil 0543
- Electronics and Electrical 0544
- Heat and Thermodynamics ... 0348
- Hydraulic 0545
- Industrial 0546
- Marine 0547
- Materials Science 0794
- Mechanical 0548
- Metallurgy 0743
- Mining 0551
- Nuclear 0552
- Packaging 0549
- Petroleum 0765
- Sanitary and Municipal 0554
- System Science 0790

Geotechnology 0428
Operations Research 0796
Plastics Technology 0795
Textile Technology 0994

PSYCHOLOGY
General 0621
Behavioral 0384
Clinical 0622
Developmental 0620
Experimental 0623
Industrial 0624
Personality 0625
Physiological 0989
Psychobiology 0349
Psychometrics 0632
Social 0451

THE DEVELOPMENT OF ACTIVE INTEGRATED ANTENNAS AND A DESIGN METHODOLOGY

BY

DAVID J. ROSCOE

A Thesis submitted to the Faculty of Graduate Studies of the University of Manitoba in partial fulfillment of the requirements for the degree of

DOCTOR OF PHILOSOPHY

ABSTRACT

A study of active integrated antennas has been undertaken.These antennas provide a control mechanism for antenna performance which is not possible with passive radiators. This research is directed towards active antennas which permit the current distribution along the structure to be altered in a controlled manner.

A design methodology has been developed and verified as a useful engineering design tool. The design methodology allows for the analysis of an arbitrarily shaped active integrated travelling wave antenna. An electromagnetic based circuit simulator is used in conjunction with a post-processor. The circuit simulator is the analysis tool to determine the current distribution, while the post-processor is used to calculate the radiation characteristics. In addition, a noise model has been developed. The model is used to calculate the output temperature of active integrated travelling wave antennas. These tools have been verified experimentally, with good agreement between the calculated and measured results.

An active integrated antenna has been designed, modelled, fabricated, and verified experimentally. The structure is a series distribution of microstrip transmission line and amplifiers. This antenna has been shown to possess numerous characteristics unachievable by traditional passive elements. However, some undesirable traits such as poor noise temperature performance have also been identified.

The actual implementation of this type of active antenna will depend upon the application, of course. Some applications have been investigated and are presented. The information presented within this thesis may also be used in the analysis of EHF circuit designs and study of concepts for designing circuitry which will radiate effectively. This has been recommended as a potential application of the developed technology.

Acknowledgements

I would like to express my sincere thanks and appreciation to Dr. L. Shafai and Dr. A. Ittipiboon for their constant guidance and support throughout my graduate studies at the University of Manitoba. The different opportunities presented to me by Dr. Shafai are gratefully acknowledged.

I would like to thank Dr. M. Palfreyman, Director-General, Components and Devices, Mr. R. Douville, Director, Components and Subsystems, for the opportunity provided to carry out the research for this thesis in a cooperative environment between the Department of Components and Subsytems, Communications Research Centre, and the University of Manitoba. I would also like thank Michel Cuhaci, MHMIC project leader, for his support and advice during this project.

Many thanks are addressed to all those at CRC and at the University of Manitoba who assisted with the fabrication and measurements of the developed antennas, especially Brian Clarke and Brad Tabachnik.

Special thanks to my colleagues at the University of Manitoba and those from other universities who were located at CRC. In particular, I would like to acknowledge Neil Simons and Langis Roy who were always available for many fruitful discussions.

I would like to thank my family for their encouragement and support throughout the years. I am indebted to my wife, Diane, for her support and understanding. I would also like to thank Colin M^{c}Arthur and Chris Allen for their support.

Financial support provided by Dr. Shafai and the University of Manitoba Fellowship is gratefully acknowledged.

TABLE OF CONTENTS

List of Figures

List of Tables

CHAPTER 1 : INTRODUCTION

1.1 Purpose and Application

An active antenna is defined in this thesis as a radiating element on which the current distribution along the structure may be altered in a controlled manner. The ability to control the current distribution along its structure is the unique feature of this class of antenna and gives it its primary advantages. With this ability, radiation characteristics such as pattern shape, axial ratio, and gain may all be controlled. This type of control mechanism for antenna performance is not present with passive radiators. The current distribution cannot be varied, hence radiated pattern characteristics cannot be altered.

This feature and the control over performance leads to novel applications of active antennas in communication systems, as individual radiators or as a plurality of elements forming a phased array. Provided device and fabrication technology is available, active antennas can be implemented at all frequencies. At EHF, a single layer monolithic microwave integrated circuit (MMIC) active antenna or phased array could be fabricated in a single batch process. (A monolithic microwave integrated circuit is a circuit which has all passive and active elements and interconnections implanted into the body, or onto the surface of a semi-insulating substrate). This type of structure integrates circuitry with radiators to produce a functional circuit with desired radiation characteristics.

Active antennas are advantageous for systems which incur large feed losses. With amplifiers integrated with the antenna, the losses due to the feed network become secondary. In addition, matching networks may be eliminated by integrating the devices with the antenna taking into account the input impedance of the devices, i.e. matching to 50 ohms is not a necessity.

The purpose of this thesis is to undertake the development of active integrated antennas and the concomitant design methodology . The integrated antennas are intended to be compatible with monolithic microwave integrated circuits. Applications in the 1 - 4 GHz range will be demonstrated with MHMIC technology, while higher frequency (EHF) applications are anticipated. (A miniature hybrid microwave integrated circuit (MHMIC) is a circuit which has only its passive elements implanted onto the surface of a substrate, with the active devices connected to the circuit separately by wire bonds). This work has focused on travelling wave antenna structures. Issues such as gain control, pattern shaping, noise figure, and fabrication are addressed. A design methodology dealing with these, along with a noise model, have been developed.

It should be made clear that there can be two levels of active antennas. One is at a radiating element level where active devices are incorporated. The other is at an array level where active devices are incorporated outside a radiating element in a feed network. Active devices at the array level results in what is referred to as an "active phased array antenna". All the radiating elements can be either passive or active. The literature thus far treats only active phased arrays using passive radiating elements. This thesis deals mainly with an active antenna at the element level. Its possible application in an active phased array has also been addressed.

1.2 Scope

Background information pertaining to active antennas is presented in Chapter 2. Also included in this chapter are the basic theory and problems associated with phased arrays.

Chapter 3 presents a technique developed to design, simulate, and analyse an active integrated antenna. A design methodology is presented first, followed by the derivation of a noise model.

The verification and the design of an active antenna is presented in Chapter 4, followed by both computer simulation results and experimental measurements. The chapter concludes with experimental results on noise figure which are used to validate the developed noise model.

Chapter 5 presents some applications in which active integrated antennas may be used.

The final chapter of this thesis presents some conclusions concerning active integrated antennas and recommendations for future work.

CHAPTER 2 : BACKGROUND INFORMATION

2.1 Active Antennas

Active antennas have been reviewed in the literature [1]-[38]. All papers and antennas presented in this chapter have been classified in the literature as active antennas. It should be noted that these structures do not all fall into the definition presented in Chapter 1. The definition previously introduced is repeated here, as a radiating element on which the current distribution along the structure may be altered in a controlled manner.. This definition is that which is most appropriate for the research carried out and it should not be confused with the definitions presented by other authors.

Perhaps the first active antenna work was performed in the early to mid 1960's by Copeland et al. and Fujimoto [1]-[4]. This work consisted of integrating a transistor amplifier with a dipole antenna as shown in Figure 2.1 [2]. The resultant structure was referred to as an "antennafier". This resultant structure offered advantages including amplitude distribution control, low noise, high gain and size.

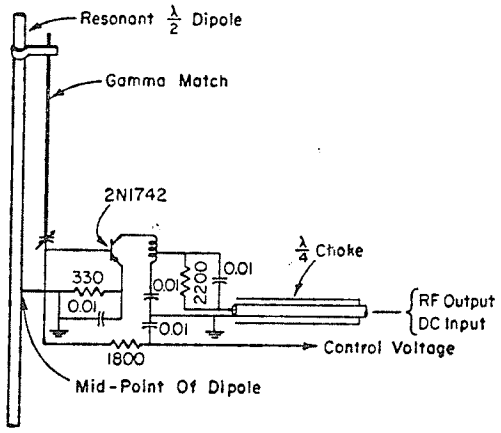

Figure 2.1 : The transistorized dipole antennafier with controllable gain [2].

The literature revealed little publication in the active antenna field during the 1970's. However, renewed interest in the field was evident after the paper published by Thomas et al. [5] where a GUNN diode was integrated with a microstrip patch (Figure 2.2a), [5]). This renewed interest [5] - [38] may be attributed to developments in device and microstrip antenna technologies. The microstrip antenna medium is ideal for integrating active devices to produce a planar structure. The active patch in Fig. 2.2 is a transmitting configuration where the source has been integrated directly with the patch. The standard 50 ohm matching network is eliminated by connecting the diode to the patch where the patch input impedance matches that of the diode (~10 ohm). Similar active antenna structures using circular and rectangular microstrip patch antennas with GUNN or GaAs IMPATT diodes have been reported in [6] - [9]. To summarize their operation, when a d.c. bias is applied the diode converts the d.c. power to R.F. power and the patch then radiates the power into free space. These devices are best suited for higher power applications; however, heat sinks are required because of the low d.c. to R.F. conversion efficiency. As indicated in Figure 2.2 b) [8], d.c. bias can be applied to the centre of a non-radiating side of the patch at an R.F. null.

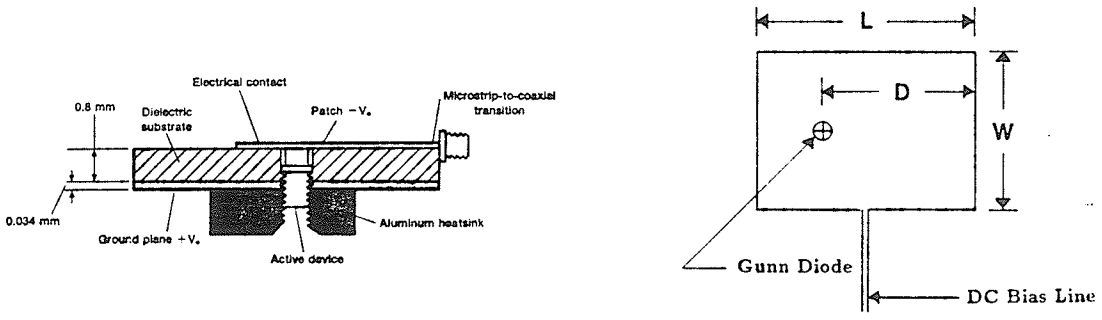

a) b)

Figure 2.2 : Active patch with integrated diodes [5].

Field-effect-transistors (FETs) have also been integrated with microstrip patch antennas [10], [11]. FETs are higher efficiency devices than diodes and have lower noise figures. They are used for applications requiring lower power. In [10], Chang et al. use a microstrip patch antenna in the feedback loop of an oscillator circuit (Figure 2.3 [10]). In effect, the patch is the resonator which dictates the frequency of oscillation. The input and output of the FET are matched to a 50 ohm system and the FET is connected to the patch where the antenna input impedance is 50 ohms.

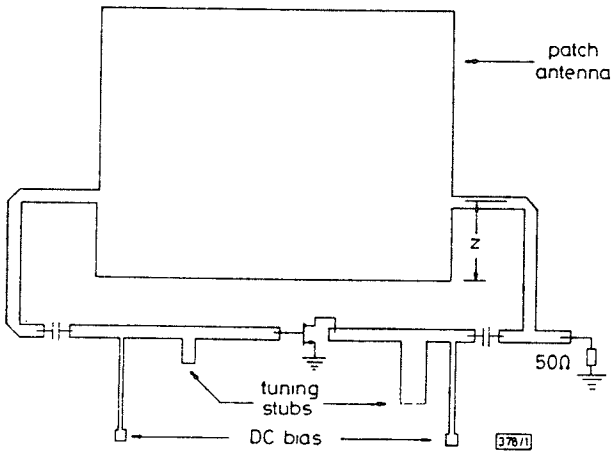

Figure 2.3 : FET-active patch antenna [10].

A FET also has been integrated with a microstrip patch in a different manner as reported in [11] (Figure 2.4 [11]). In this configuration , the FET is located on top of a split microstrip patch antenna. Again, this unit operates as an oscillator. The patch is divided into two parts to provide d.c. isolation between the drain and gate. Capacitance feedback is provided by the slot and d.c. bias is supplied through quarter-wave transmission lines. It should be noted that the low frequency oscillator used high frequency FETs operating in their instability region to ensure oscillation.

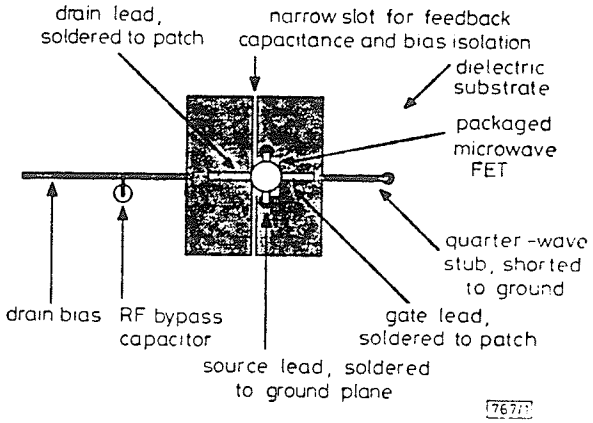

Figure 2.4 : Alternate configuration of FET-active patch antenna [11].

A variation of the FET-active split patch microstrip antenna is a dual FET configuration reported in [12] (Figure 2.5, [12]). Again, the gap between the gate and drain provides d.c. isolation and a feedback loop. The two devices operate in a push-pull manner producing twice the output power of a single FET patch antenna. A lower cross-polarization level was also reported.

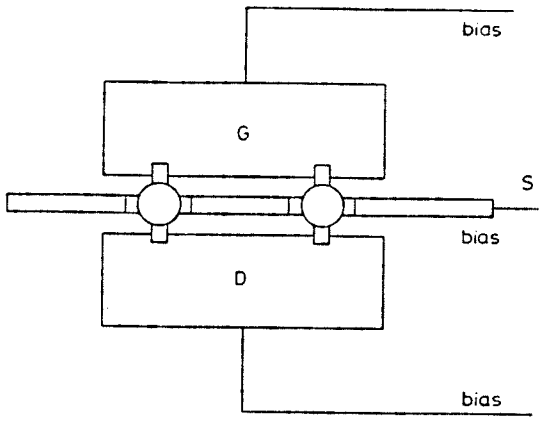

Figure 2.5 : Dual FET active patch antenna [12].

More recent planar compact active antennas are reported in [13]-[15]. The active antenna reported in [13] and [14] is of interest as a notch antenna is used instead of a patch (Figure 2.6, [13]). The FET is operated in oscillation and as with the split patch

structure, a narrow slot is used to provide d.c. isolation between the gate and drain and to provide a feedback loop.

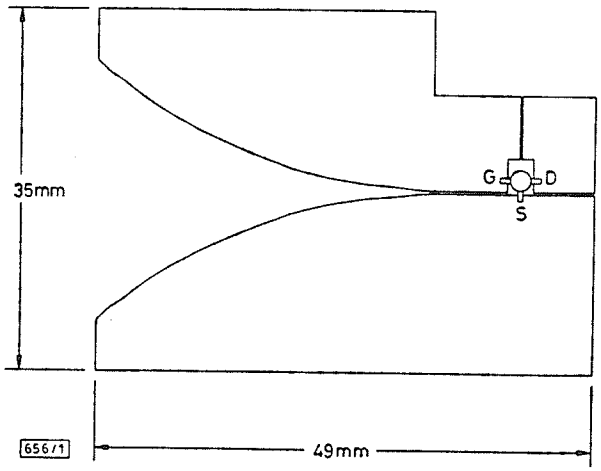

Figure 2.6 : FET active notch antenna [13].

The type of microstrip antenna used in active antennas is not restricted to single resonant patches as has been predominantly reported. Leaky-wave antennas have been used in FET-oscillators as reported in [16] (Figure 2.7, [16]).

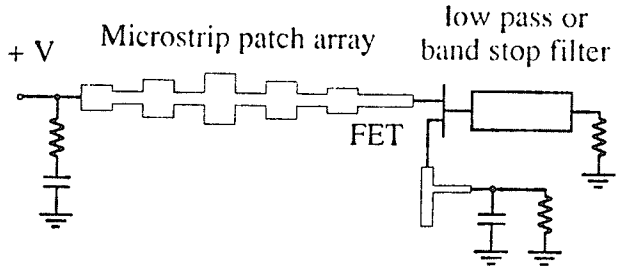

Figure 2.7 : FET-oscillator circuit incorporating a microstrip patch array [16].

Leaky-wave and slot antennas have also been used in quasi-optical devices [17] - [20]. Quasi-optical devices are referred to as components formed by combining circuit elements with antennas where the interconnections are made by waves propagating in free space. An example is the transceiver module shown in Figure 2.8 [18].

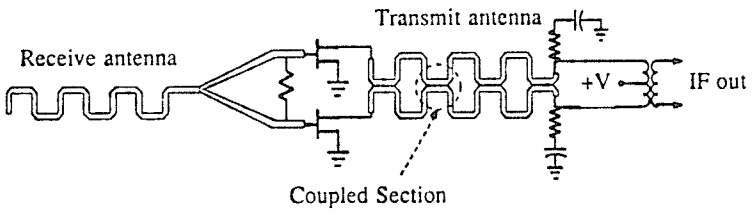

Figure 2.8 : Transceiver circuit [18].

Figure 2.8 shows two rampart line arrays being used in the transceiver, one as the receive antenna and the other as the transmit antenna. In the transmit mode, the dual rampart lines act as resonant structures to produce the oscillator circuit. The generated oscillator frequency is then radiated by the travelling wave antenna. In the receive mode, the FETs function as self-oscillating mixers for down conversion to I.F., i.e. the receive signal is mixed with L.O., I.F. is transmitted through the transmit antenna and extracted by the transformer for I.F. out. These units have been demonstrated for Doppler motion detection [18].

Recent publications [21] - [23] include active multilayer patch antennas (Figure 2.9). This type of structure is well suited for multilayer phased array antenna architectures. This configuration uses a ground plane separating two dielectric layers. The microstrip antenna is located on the top layer of low relative permittivity dielectric and the active circuitry is on the bottom layer of high relative permittivity dielectric.

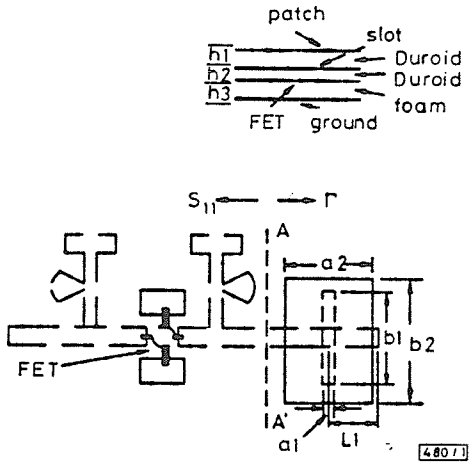

Figure 2.9 : Active multilayer patch antenna [21].

An alternative to the previously reported oscillator structures has been reported in [23]. This structure differs in that a multilayer architecture is used (Figure 2.10, [23]). As depicted in figure 2.10, ports 1 and 2 represent the amplifier load and source respectively. The amplifier circuit located on the bottom layer of the structure is combined with a microstrip patch antenna located on an upper substrate. Slot coupling between the circuit and patch is used. The resulting structure is a radiating feedback loop oscillator. This structure was demonstrated at an operating frequency of 2.4 GHz, with expected application at X-band.

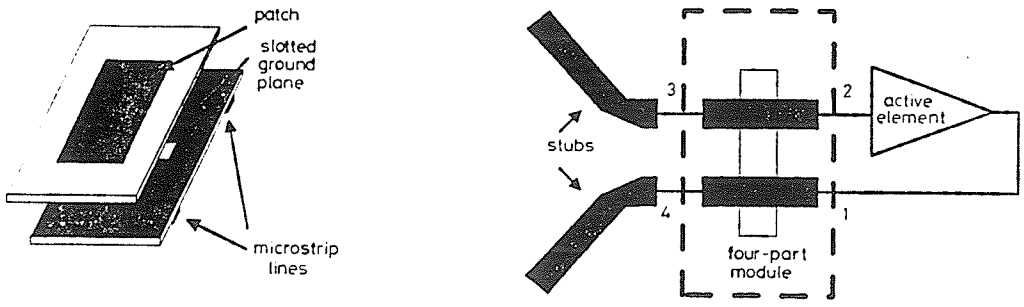

Figure 2.10 : Two-port active coupled microstrip antenna [23].

In terms of EHF applications, perhaps the first integrated active antenna fabricated as a monolithic microwave integrated circuit was developed by Roy et al. [24]. This configuration uses a FET and slot antenna where the output of the amplifier is directly matched to the input impedance of the slot radiator (Figure 2.11). This active antenna was fabricated on a GaAs wafer and demonstrated operation at its design frequency of 30 GHz.

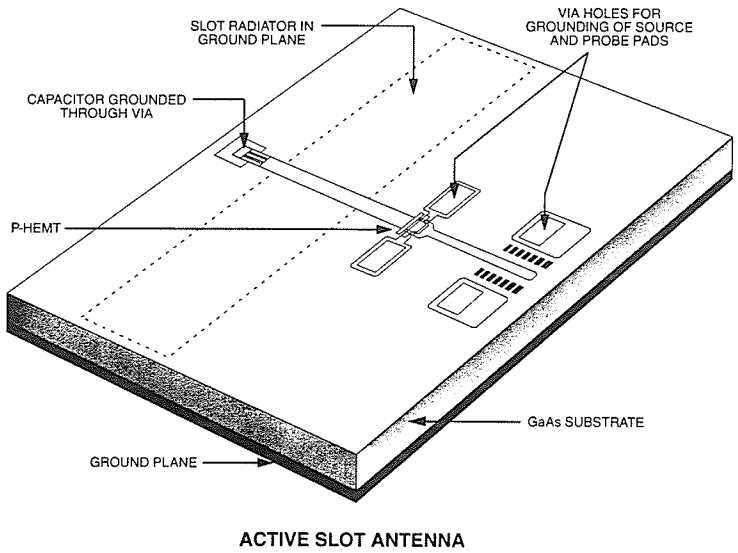

Fig 2.11 : MMIC active slot antenna [24].

Other active antenna configurations utilizing a slot radiator are presented in [25] and [26]. The structure reported in [25] differs from the previous slot configuration in that MESFETs are used to tune the slot length, not to amplify the signal. The MESFETs are located on the layer below the slot and are used to reactively load the ends of the slot (Figure 2.12, [25]). This configuration allows the slot length to be varied electromagnetically. The structure presented in [25] yielded a 10% tuning range.

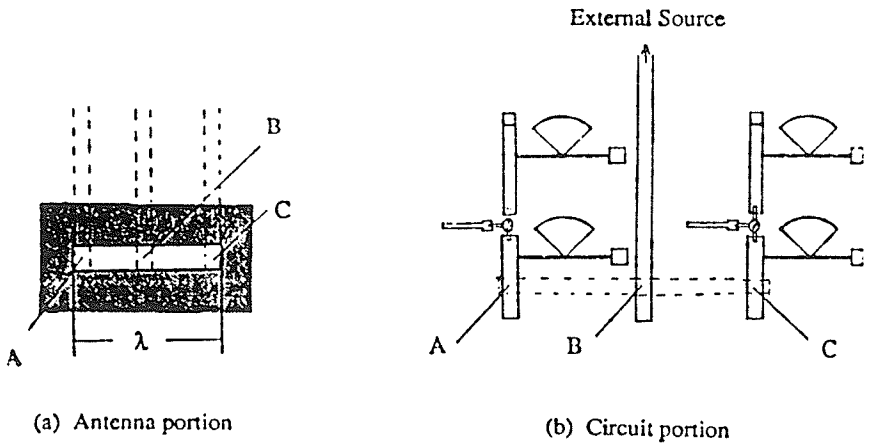

Figure 2.12 : Reactively tuned active slot antenna [25].

An oscillator circuit utilizing a slot radiator is reported in [26] (Figure 2.13, [26]). Two MESFETs, operating in oscillation, are connected in parallel to a slot radiator. This structure was designed for X-band and can be compared to a similar structure where only one oscillator is connected to the slot. An increase of radiated power from the slot was reported to be 1.5 dB when comparing the two configurations. In addition, the double-oscillator configuration had a larger tuning range, with a maximum of 48 MHz.

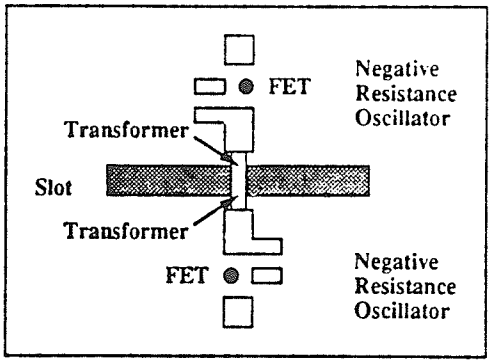

Figure 2.13 : Dual oscillator FET active antenna.

Spatial power combining structures using a FET-oscillator and an array of patches with GUNN diodes have been reported in [27] and [28] respectively. More recent publications on array architectures utilizing active elements are reported in [29]-[32]. An active patch configuration using a FET and varactor diode is presented in Figure 2.14, [29]. This element was used in an array configuration . The FET within the patch is used to produce a radiating patch oscillator. The integrated varactor diodes are used to provide variable radiated phase. The variation in phase is achieved with d.c. bias control. Beam scanning in excess of 40^{o}, along with cross-polarization levels of less than -25 dB were reported.

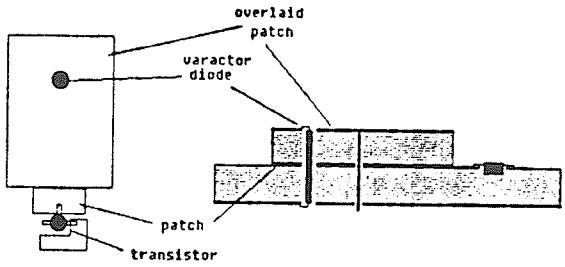

Figure 2.14 : Varactor / FET active antenna used in an array [29].

Limited beam steering with an active element array was reported in [31]. The element and array configuration is presented in Figure 2.15, [31]. A GUNN diode is integrated with a circular patch antenna and placed in an array.

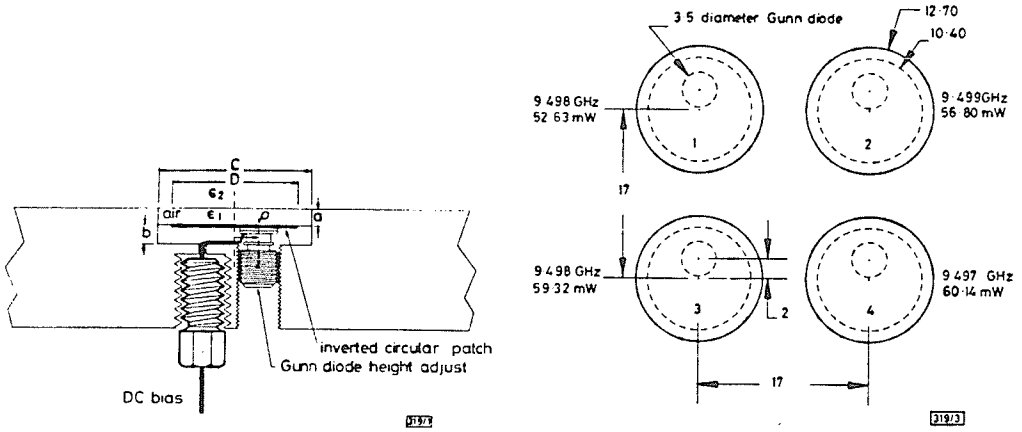

Figure 2.15 : GUNN diode active antenna and array configuration [31].

Again, each element is a radiating patch oscillator. Beam steering is achieved by setting up an injection-locking phase shift between each active element. This approach to beam steering is unique in that other active element array structures have all oscillating patches injection-locked to a common signal. A limited beam steer of 15^{o} is reported.

A travelling wave array having diodes integrated along the feed structure is presented in [32] (Figure 2.16, [32]). The concept of operation of this structure is similar to the active antennas developed in this thesis. As depicted in figure 2.16, varactor diodes are integrated with the travelling wave feed line. The diodes act as phase shifters in this configuration. Beam scanning of 20^{o} as well as noise figure degradation are reported.

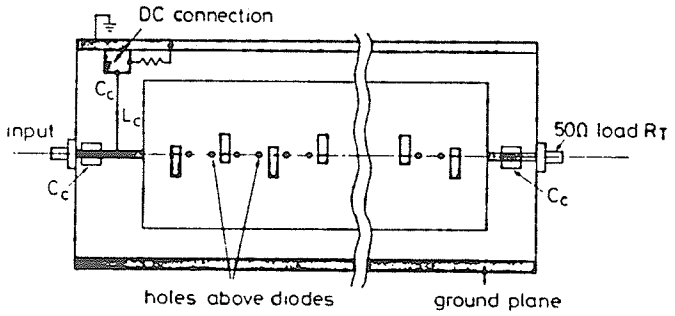

Figure 2.16 : Travelling wave configuration with integrated varactor diodes [32].

2.1.1 Analysis of Active Antennas

With respect to the analysis and design of active integrated antennas, there is not a definitive design methodology or analysis technique. This is due to the complexity of the structures. For the most part, the structures presented were designed empirically. Fusco, [39], [40], has applied numerical optimization to optimize the terminal voltages of a MESFET in a FET oscillator (Figure 2.3). The purpose was to maximize power and the microstrip patch antenna was matched to the FET based on this optimization. Itoh, et al. [17], [18], use a microwave circuit simulator, Touch Stone [52] (an EEsof product) to analyse circuit characteristics of their developed transceivers (Figure 2.8). However, experimental results were required to verify the radiation characteristics. This is necessary as Touch Stone does not model radiative losses accurately. Shen et al., [21], also use Touch Stone to verify the circuit response of an active multilayer patch antenna (Fig. 2.9). A finite difference time domain method was applied separately to the slot coupled antenna to determine the input impedance.

Perhaps the most rigourous analysis of an active multilayer antenna was performed by Gillard et al. [41]. Their technique is based on the integral equation and solution by moment method. The active device is replaced by an equivalent model and then the entire structure is analysed. The reported theoretical and experimental results were in good agreement. This technique can be applied to other active antenna structures and shows promise as a design tool.

Hall [42] uses a magnetic current source model to represent a FET oscillator (Figure 2.3). In this approach the transistor itself is also replaced by a current source. The measured and calculated results reported are in good agreement. Most recently, Hall has incorporated the use of a circuit simulator to model active antennas more accurately [43]. The microwave design software package Touch Stone is used to model the circuit

performance. The calculated voltages are extracted and used as a source distribution in the previously developed magnetic current model. This analysis approach is similar in concept to the approach developed in this thesis. However, it should be noted that work in [43] was published after the method developed within this thesis was completed. One major difference between [43] and the design methodology developed in this thesis is that a full wave electromagnetic circuit simulator is used in the latter [44]. Thus more accurate results are anticipated. This is discussed in detail in Chapter 3.

2.2 Phased Array Antennas

An antenna containing more than one radiating element may be classified as an array. The performance of the array depends on the element configuration and excitation amplitude and phase. An antenna whose main beam of radiated power is steered by element excitation phase changes is called a phased array antenna. With an electronically steered main beam, the antenna can be secured in a fixed position and can scan at rates unattainable by mechanically scanned antennas. One of the growing interests with active integrated antennas are their application to phased array antennas. Due to the nature of these elements, a planar architecture would most likely be utilized in an array containing hundreds or thousands of elements. A literature review of phased array antennas yields numerous publications on this topic and a brief review is presented here based upon [45]-[47].

The main beam of an array may be characterized by the product of the element factor and the array factor. A linear phased array antenna will typically be constructed of N identical radiating elements having certain characteristics. The element excitation and orientation dictate the type of radiation pattern obtained. This is known as the element factor and represented by $F_n(\theta,\phi)$. In an array, each element is fed by currents having

amplitude and phase. The sum of contributions from all these element currents is known as the array factor and is a function of element location and their complex excitation. A planar array with arbitrary element locations is given in Figure 2.17.

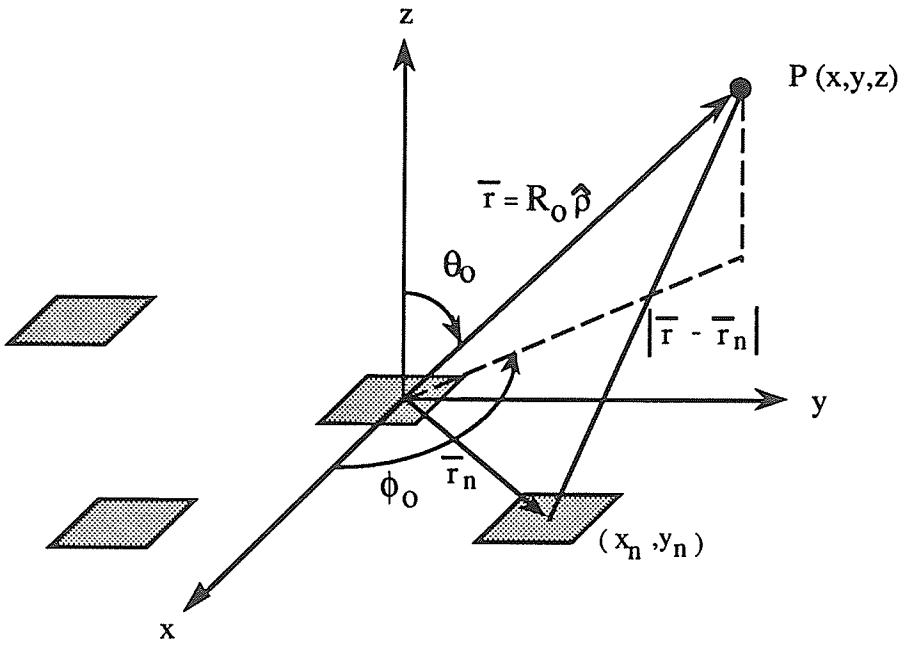

Figure 2.17 : Planar Array

If mutual coupling between radiating elements is neglected, the total radiated field may be given as

$$\bar{E}(\theta,\phi) = A\sum_n \bar{F}_n(\theta,\phi)\, I_n \frac{e^{-jk|\bar{r}-\bar{r}_n|}}{|\bar{r}-\bar{r}_n|} \qquad (2.1)$$

where $\bar{F}_n(\theta,\phi)$ is the element pattern
I_n is the complex excitation
A is a constant
k is the wave number, $k = 2\pi/\lambda$
where the wave length, $\lambda = c/f$
c is the velocity of light in free space
f is frequency
$|\bar{r} - \bar{r}_n| = [\,(x-x_n)^2 + (y-y_n)^2 + z^2\,]^{1/2}$

Let the distance from the origin of the array to the observation point be represented by R_o and under the far field condition, $|\bar{r} - \bar{r}_n|$ can be approximated with

$$|\bar{r} - \bar{r}_n| \cong R_o - \bar{r}_n \cdot \hat{\rho}$$

where $\hat{\rho} = u\hat{x} + v\hat{y} + \cos\theta\,\hat{z}$

and u and v are the directional cosines; $u = \sin\theta\cos\phi$

$v = \sin\theta\sin\phi$

Thus, equation (2.1) may be written as

$$\bar{E}(\theta,\phi) = A\sum_n \bar{F}_n(\theta,\phi)\, I_n \frac{e^{-jk(R_o - \bar{r}_n \cdot \hat{\rho})}}{(R_o - \bar{r}_n \cdot \hat{\rho})}$$

$$\bar{E}(\theta,\phi) = A\frac{e^{-jkR_o}}{R_o}\sum_n \bar{F}_n(\theta,\phi)\, I_n\, e^{jk\bar{r}_n \cdot \hat{\rho}} \qquad (2.2)$$

where $\bar{r}_n \cdot \hat{\rho}$ may be neglected in the denominator since its magnitude is $<< R_o$

A main beam can be formed and steered to any location in space specified by the angle (θ_o,ϕ_o). This may be accomplished by selecting appropriate excitation currents. Two methods of steering may be used, time delay steering or phase steering. However, time delay devices are costly and hence phase steering becomes a desirable method. Phase steering is accomplished by utilizing phase shifters at each element designed to operate at a specific frequency, f_o. Thus the excitation current becomes

$$I_n = |I_n|\, e^{-jk_o \bar{r}_n \cdot \hat{\rho}_o}$$

where $k_o = 2\pi/\lambda_o$, $\lambda_o = c/f_o$

Substituting into equation (2.2) yields

$$\bar{E}(\theta,\phi) = A\frac{e^{-jkR_o}}{R_o}\sum_n \bar{F}_n(\theta,\phi)\,|I_n|\, e^{-jk_o\bar{r}_n \cdot \hat{\rho}_o}\, e^{jk\bar{r}_n \cdot \hat{\rho}}$$

$$\bar{E}(\theta,\phi) = A\frac{e^{-jkR_o}}{R_o}\sum_n \bar{F}_n(\theta,\phi)\,|I_n|\, e^{j\bar{r}_n \cdot (k\hat{\rho} - k_o\hat{\rho}_o)} \qquad (2.5)$$

Equation (2.5) shows that at a specified point (θ_o,ϕ_o), there is a frequency dependence. The operational bandwidth of a phase steered array is limited by the

bandwidth of the phase shifters. Other problems associated with phased arrays are grating lobes, scan blindness, and feed losses in some architectures.

Grating lobes are radiation patterns equivalent to the main beam but at other angular positions. This is generally undesirable and may be avoided by keeping the element spacing fairly small. Mailloux [45] has examined this problem thoroughly and has shown that element spacing less than one-half wavelength will generally suppress grating lobes. In addition, an element type which has a null in its radiation pattern corresponding to a grating lobe location could be selected.

Scan blindness is a condition when the antenna array does not radiate any power at a certain scan angle. This phenomenon is related to the impedance of each element of the array as the beam is scanned. The impedance of each element is a function of its self impedance and the mutual impedances of all other elements. When looking at the total impedance of an element, the impedance contribution from other elements in the array is a function of the scan angle. It has been determined that at certain scan angles the total impedances become quite large. This increase in total impedance creates a large reflection coefficient at that element, thus preventing energy from radiating. In addition, Pozar [47], determined that scan blindness is also related to the resonance of a trapped surface wave mode. He also studied the effects of substrate thickness, relative permittivity and element spacing with respect to the scan blindness angle. The normal operating condition is to contain the beam in the broadside direction. Pozar found that the scan blindness angle approaches broadside as substrate thickness, relative permittivity and element spacing decrease. These parameters should be taken into consideration when applying MMIC technology to phased array antennas.

The losses associated with a feed network are an important aspect of an array when considering receive applications. Although low loss feed networks such as wave guide can be used, it is preferable to use a microstrip medium, from a manufacturing and design point of view. A microstrip feed network would produce a structure which is compact and low cost in comparison to wave guide. Disadvantages of this type of feed network are the losses associated with it (dielectric, copper, and radiative losses). It has been shown in [48] that these losses limit the achievable gain in large arrays (containing hundreds or thousands of elements). This relationship is presented in Figure 2.18. As can be seen, the gain that one would expect from the associated aperture size is not obtainable because of the feed losses. This graph shows that a limit is reached where increasing aperture size to increase gain becomes futile.

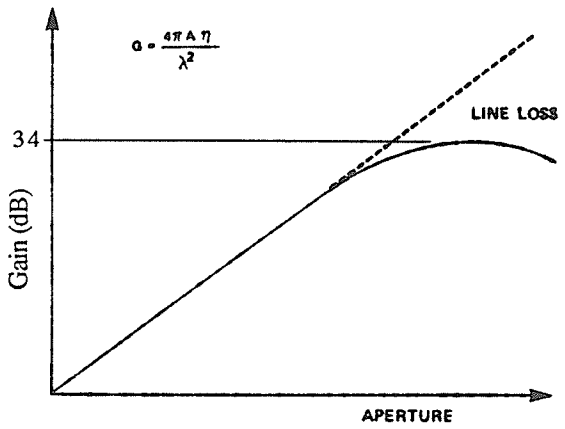

Figure 2.18 : Aperture gain and achievable gain versus array size.

One approach to minimize these feed network losses is to place low noise amplifiers (LNAs) right at the radiating elements. This configuration is classified as an active phased array antenna.

2.2.1 Active Phased Arrays

An active phased array antenna is defined here as an array where both the supplied current amplitude and phase of each element can be varied. This type of array has several advantages over other array architectures. One advantage is that the losses in the feed network become second order. In the receive case, all losses ahead of the LNA add directly to the noise figure of the antenna. Thus if the path loss between the radiating element and LNA can be minimized, then the overall G/T of the antenna will improve [49]. G/T is the gain to temperature ratio which is used as a figure of merit in assessing the performance of antennas. This issue of noise figure and G/T is discussed in detail in Chapter 5.

Another advantage of active phased arrays is that a tailored aperture distribution can be readily generated when amplitude control is available at each element. A tailored aperture distribution allows one to minimize sidelobe levels [50].

Over all, an active phased array antenna has improved performance which results in the reduction of the number of elements required within an array. For the transmitting case, the amplifiers at each element are sufficient to replace a high power source with one of lower power. This would reduce both cost and size and at the same time increase reliability. The primary disadvantages of active phased array antennas are the complexities in fabrication, and heat dissipation of the circuitry.

Two general array architectures which have been reported are the brick and tile configurations. The brick configuration contains modules perpendicular to the aperture plane while the tile configuration has the circuitry and radiating elements parallel to the aperture plane. This thesis addresses conformal structures, hence the brick architecture is not considered further.

Three basic planar array architectures are shown in Figure 2.19 which illustrate single layer and double layer structures, each characterized by different feeding schemes [47].

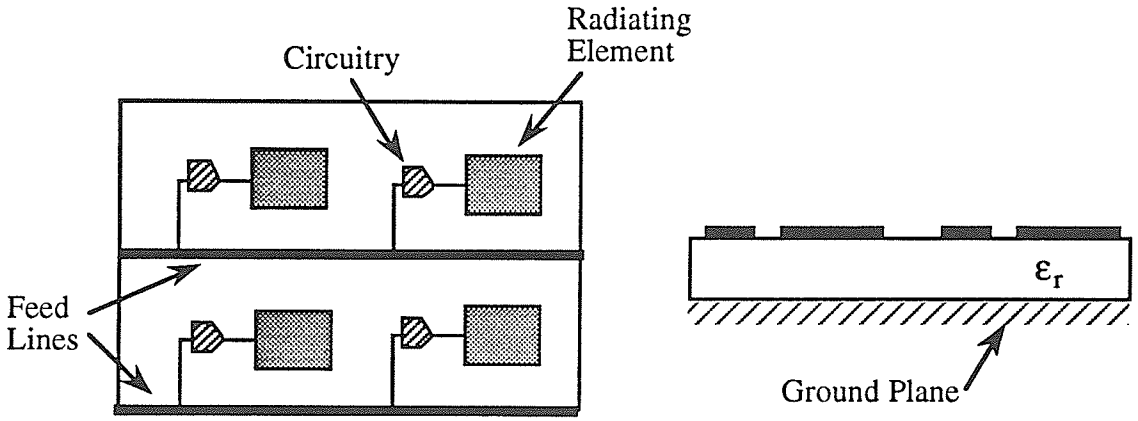

Top View Side View

(a) Single Layer: Direct Feed

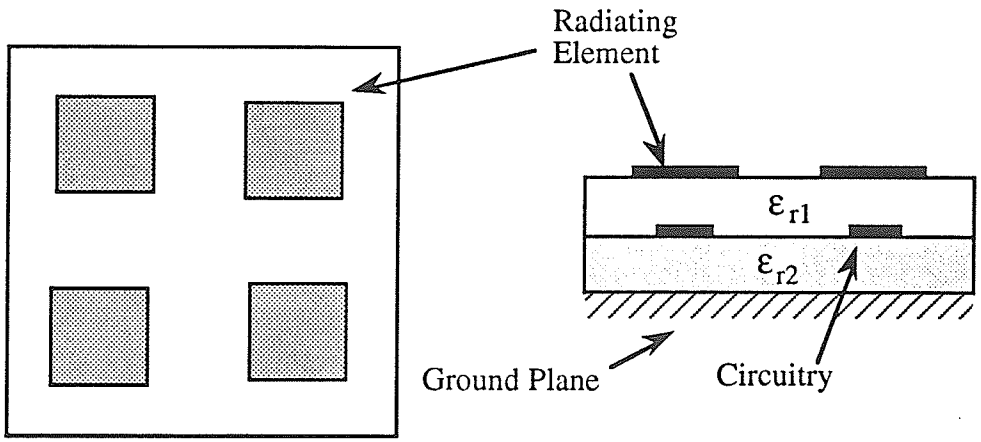

Top View Side View

(b) Double layer:Proximity Coupling

Figure 2.19 : Tile architectures

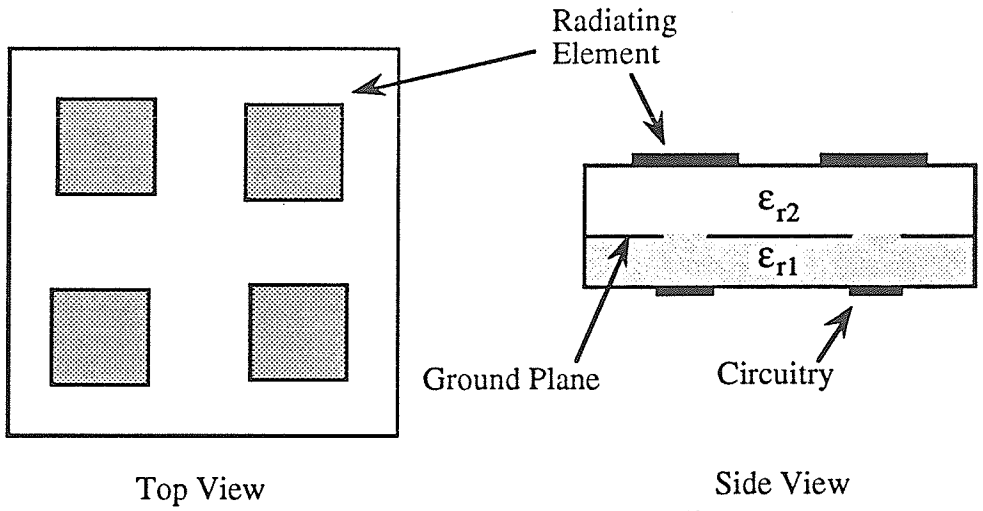

(c) Double layer : Aperture coupling

Figure 2.19 (cont.)

The single layer structure shown in Figure 2.19 (a) would be ideal for MMIC technology since it is the only truly monolithic structure. That is, all the circuitry, feed lines and radiating elements could be fabricated in a one batch process. With hundreds to thousands of identical units required, this becomes very desirable and feasible. However, there are many problems associated with a single layer structure because all components of the array are placed on a GaAs substrate. One problem is that spurious radiation from the feed network will degrade the sidelobe and cross polarization levels as well as the main beam. Another problem is that a GaAs substrate is used for the circuitry and this is not very suitable for radiating elements. The GaAs substrate is very thin, varying from h = .254 mm to h = 1.27 mm, and has a relative permittivity (ε_r) close to thirteen. These properties are not desirable for radiating elements. In general, radiating elements demonstrate improved performance on thicker dielectric substrates having low relative permittivities. This is the rationale behind the multi-layered structures shown in figure 2.19. The structure in figure 2.19 (b) has a high relative permittivity substrate layer, ε_{r1}, for the circuitry and a low relative permittivity dielectric layer, ε_{r2}, for the radiating elements. Excitation of the radiating elements is accomplished with proximity coupling. However, this structure is susceptible to undesirable circuit element coupling to the

radiating elements. The structure in Figure 2.19 (c) eliminates this problem by feeding with aperture coupling . The multiple dielectric layers are for circuitry and antenna as before. However, a ground plane is situated in between the two layers, hence eliminating unwanted coupling, i.e. spurious radiation. In the multilayer configuration, the antenna could be built in a subarray module approach to further reduce the cost and complexity. This involves dividing the array into smaller subarrays which could then be constructed as plug-in units to form the total array. Each element could be passive with each subarray module excited with amplitude and phase control. This concept of plug-in units has advantages in trouble shooting and repairing an array. Each module could be tested for proper operation and a malfunctioning module could be replaced with an operating module. This is advantageous because MMICs cannot be altered or repaired after they are fabricated.

Active integrated antennas are ideal for active phased array applications because the active elements are compact and incorporate the required active circuitry.

CHAPTER 3 : MODELLING ACTIVE ANTENNAS

3.1 Introduction

A notable characteristic of the previously presented active antennas is that the active device and radiating element remain separate entities. That is, typically a resonant antenna has been incorporated into a circuit, or a device has been imbedded in, or close to, the antenna element. The results are active antennas, but they do not fall into the definition outlined in Chapter 1. Although active devices have been used in these antennas in various forms, the current distribution along the radiating structure cannot be altered, i.e., the pattern emanating from the antenna cannot be freely altered. It is the purpose of this thesis to develop active integrated antennas where the current distribution along the radiating structure can be controlled. Focus of the work has been on travelling wave structures. This type of structure allows intuitive understanding of the energy propagation along the structure and how active devices may be used to alter this distribution. A design methodology is developed to assist in the analysis and design of travelling wave active integrated antennas of arbitrary geometry having arbitrarily located active devices.

To facilitate the design of these active integrated antennas it is imperative that design tools are available. A structure where devices are integrated within the antenna requires a computer aided design (CAD) tool where both circuit parameters and electromagnetic properties are accounted for in its analysis.

A survey of commercially available software, [51]-[56], indicates that there is an absence of software suitable for the analysis of active integrated microstrip antennas. On the antenna side, the available software either lacks the ability to model the substrate, such as Numerical Electromagnetic Code (NEC) [51] or lacks the ability to incorporate active devices. From the point of view of microwave circuit analysis, radiative losses are typically

not handled in a rigorous manner. The circuit components and microstrip discontinuities are represented by characterized design curves or RLC circuits. This is the case for packages such as Touch Stone and Libra [52] (where Touch Stone is the linear modelling package of Libra, EEsof Inc.) and Super Compact and Harmonica [53] (where Super Compact is the linear modelling package of Harmonica, Compact Software Inc.). Some commercially available microwave circuit analysis packages which are based upon electromagnetic field theory are EMsim^{TM} [54], Sonnet's package [55], and High Frequency Structure Simulator (HFS) [56]. Because of the rigorous analysis approach taken, parameters such as coupling and radiation due to the geometry of the layout are accounted for in the analysis.

It is proposed here that the circuit simulator EMsim^{TM} be used to analyse active integrated antennas. However, applying this package to the analysis of printed antennas requires additional post processing to calculate radiation characteristics such as the patterns and gain.

3.2 General Theory of the Circuit Simulator

The circuit simulator selected for this work is EMsim^{TM}, distributed by EEsof Inc. EMsim^{TM} is a microwave circuit analysis package based on electromagnetic field theory. The work horse of this package is WATMIC, a computer code developed by Chow et al. at the University of Waterloo. EEsof has provided the user interface to facilitate the input of circuit geometry and associated parameters.

In the initial version of WATMIC (ver 3.0) arbitrarily shaped microstrip line structures are analysed with an approximate dynamic image model of charges and currents [57],[58]. The problem being studied is one which contains a finite microstrip line structure situated above an infinite dielectric substrate and ground plane. The underlying theory has been presented in [58] and is summarized here. Consider one current element, Idl, situated on a dielectric substrate with ground plane. Image theory dictates that this system may be

equivalently represented by a system of current and charges, and their images. There are two field regions corresponding to this problem; the field within the dielectric (Region II) and the field above the dielectric (Region I) (Fig. 3.1). In the quasi-dynamic approximation, two field components are assumed to appear, the induction and static fields referred to as Faraday and Coulomb fields respectively. It should be noted that the electric field of a current element contains an additional field; the radiated field. This field has been neglected because circuits are typically close to the ground plane ($h<\lambda/20$) and electrically small. Under these conditions, the electric field is dominated by the other field components. Thus the calculated current becomes inaccurate for thick substrates and electrically large structures where the reaction between two segments is electrically far apart.

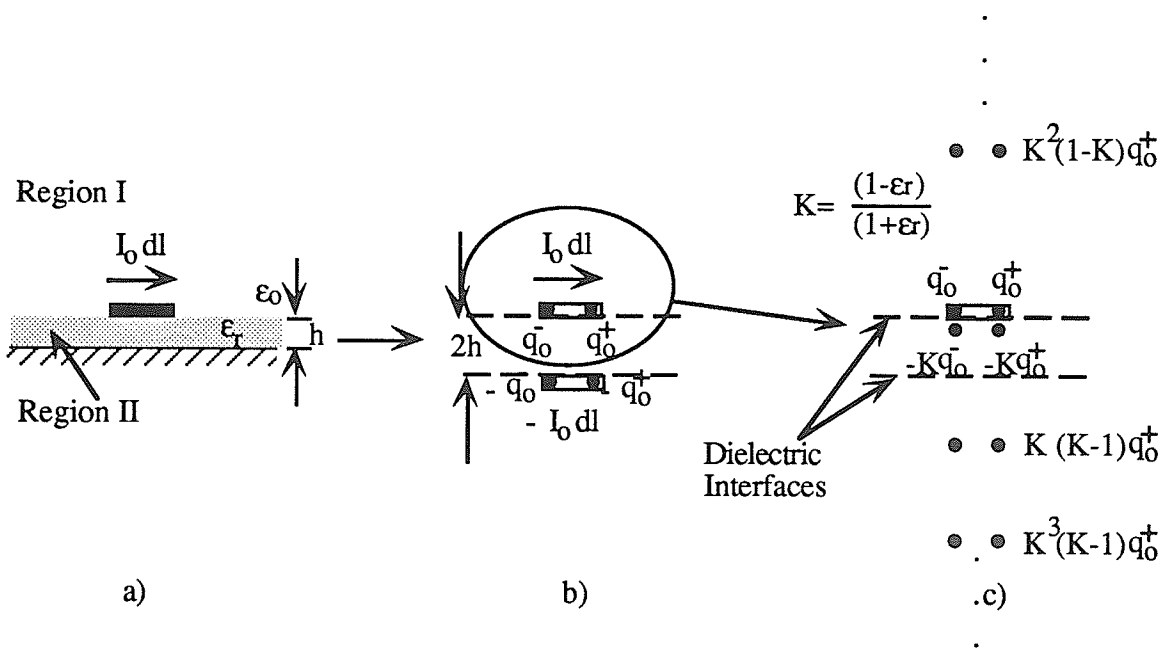

Figure 3.1 : Equivalent system representation.

The Faraday field of the electric field is due to the changing magnetic field. The dielectric interfaces do not affect this field because the quasi-static magnetic field is not

affected by non-magnetic materials. The presence of the current element indicates the existence of a positive and negative charge through the continuity equation [58]

$$j\omega q_o^{\pm} = I_o = -j\omega q_o^{-}$$

The dielectric interface will affect the fields produced by these charges. It has been determined in [59] that the "dielectric interface" effect may be represented by a series of image charges. These charges are imaged about the dielectric interfaces to generate the total field which is the sum of the fields produced by the charges and their images. Each charge is related to the true charge by a ratio, K, developed in [59] (Fig. 3.1c)). The microstrip line is on the dielectric interface hence the charges may be imaged in a free-space medium or dielectric medium, depending on the region of interest. The region of interest in this application is that of the substrate because feeds and loads are located within the substrate. Thus the charges are imaged in a dielectric medium to generate the field within the substrate. This is the only region for which the field is valid (Region II). It should be noted that the charge imaging depicted in Fig. 3.1 c) is incomplete. The image current and associated image charges have not been shown. The total field is a combination of the contributions of the complete system representation. The net electric field due to a current element has been determined to be [58]

$$\overline{E} = -j\omega\overline{A_o^{\pm}} - \nabla\left[\sum_{i=0}^{\infty}\left(\phi_{i+} + \phi_{i-}\right)\right]^{\pm} \qquad (3.1)$$

where A_o is the vector potential

$$\overline{A_o}(r) = \frac{e^{-jkr}}{4\pi r} I_o \, dl$$

k is the propagation constant in the dielectric substrate

$\phi_{i\pm}$ is the scalar potential

$$\phi_{i\pm}(r) = \frac{e^{-jkr}}{4\pi r \varepsilon_o \varepsilon_r} q_{i\pm} \quad , \; i=0,1,2,...$$

The first component in equation (3.1) is the Faraday component while the second is the Coulomb component. The superscript, ±, indicates the contribution of the image source. The total field due to many current elements will be the summation of each generated field.

In the new version of WATMIC (ver 3.5) complex image theory and surface waves are incorporated to the analysis. This results in a rapid convergence to the solution where the accuracy of the solution has been extended to the intermediate field. Thus higher frequency and thicker substrates may be modelled. The improved approximation to the Green's function is reported in [60]-[62] and summarized here. The improved Green's function has contributions from three parts; 1. a few quasi-dynamic images (near field) 2. surface waves and 3. complex images which are related to leaky waves. The incorporation of surface waves and the use of complex images are the improvements to this version. The application of complex image theory is reported in [63]-[66] and summarized here. As a general statement, complex image theory is based upon generating an approximation to the Fresnel reflection coefficient which appears in the Sommerfeld integral [63]. The purpose of generating this approximation is to avoid the numerical integration of the Sommerfeld integral. Thus, using an approximation along with the Sommerfeld identity [60], a closed form solution can be determined. The approximation is in the form of an exponential function. For example, $R(u_o)$ is defined as the plane wave reflection coefficient for TE waves as [63]

$$R(u_o) = \frac{u_1 - u_o}{u_1 + u_o} \tag{3.2}$$

where $u_o = (\lambda^2 + \gamma_o^2)^{\frac{1}{2}}$

$u_1 = (\lambda^2 + \gamma_1^2)^{\frac{1}{2}}$

where $\gamma_o^2 = -\omega^2\mu_o\varepsilon_o$

$\gamma_1^2 = j\omega^2\mu_o(\sigma_1 + j\omega\varepsilon_1)$

λ is the variable of integration of the Sommerfeld integral

Equation (3.2) can be expanded into a series representation. Initially, the series expansion was approximated with [63]

$$R(u) = - e^{-2u} \tag{3.3}$$

where $u = \dfrac{u_o}{(\gamma^2 - \gamma_o^2)^{\frac{1}{2}}}$

When expanded, the approximation used in equation (3.3) coincides with the series expansion of equation (3.2) up to the u^2 term. This representation can be classified as a single image located at a complex depth. Various improvements to the approximation given in equation (3.3) has been reported in [64] - [66]. Multiple images have been utilized and the result is a more accurate representation of equation (3.2). That is, the approximation for equation (3.2) given in [65] is

$$R(u_o) = -\frac{1}{n} \sum_{j=1}^{n} e^{-u_o d_{n,j}} \tag{3.4}$$

Equation (3.4) represents several complex images with complex locations $d_{n,j}$.

With EMsim^{TM}, Chow et al. utilize multiple complex images combined with Prony's method and nonlinear optimisation to yield a rapidly convergent solution [60], [61]. The complex images are represented by the form

$$\sum_{i=1}^{N} a_i e^{- b_i u_o} \tag{3.5}$$

The system is replaced by the real source and a few complex images (Fig. 3.2).

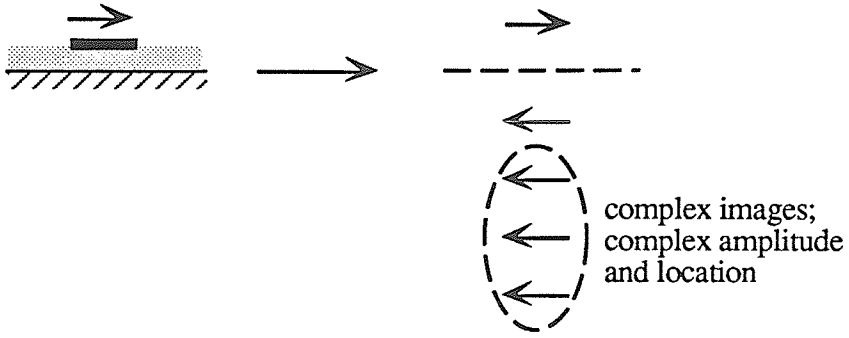

Figure 3.2 : Complex imaging for an electric segment.

The unknown coefficients in (3.5) are related to the path of integration. In the complex plane, the path is a straight line. This path corresponds to the deformed path of integration on the complex λ plane where λ is the variable of integration with respect to the Sommerfeld integral. This is where Prony's method is used. For a given complex function, f(x), Prony's method [67] gives an approximation of [61]

$$f(x) = \sum_{i=1}^{N} A_i \, e^{S_i x} \quad , x \in [X_1, X_2] \tag{3.6}$$

where A_i, S_i are complex coefficients

The interval where the function is defined (X_1 ,X_2) corresponds to the straight path of integration in the complex plane. As shown in [61], as the interval increases, the path of integration becomes more accurately defined. In addition to Prony's method, Chow uses nonlinear optimisation [61] to minimize errors in a_i and b_i of equation (3.5). It has been reported in [60],[61],[68],[69] that only three to four complex images are required to generate results within 1% accuracy. This accuracy is achieved within a range of one wavelength. Thus for electrically large structures, $>\lambda$ in this case, one would expect less accurate results. This is anticipated, as the coupling from one segment of the structures to another which is located more than a wavelength away will not be calculated accurately.

As previously mentioned, surface waves have also been incorporated into this version of EMsim^{TM}. The poles of the expressions accounting for the effects of the microstrip substrate have been extracted and evaluated separately. These poles represent the surface waves. The method of residues is used to generate a Green's function representing the surface wave contribution. This technique is reported in [60] and [70].

Thus the combination of a few quasi-dynamic images, a few complex images, and the inclusion of surface waves, yield a solution which closely follows the exact solution. The final closed form spatial Green's function used has been reproduced in Appendix I [60]. In both versions of the code, the derived closed form approximation to the microstrip Green's function is used with the moment method outlined by Harrington [71] to solve the mixed potential integral equation.

A brief summary of the user interface is now presented. EESof Inc. has provided the user interface to the WATMIC program. With this interface, drawing files which represent the circuit to be analysed are created. These drawings should be identical to the physical circuit. All associated circuit parameters are specified when the circuit drawing is generated. The structure is then segmented to accommodate the analysis technique of method of moments. Numerous measurement ports can be specified, along with the location of active devices. The active devices are represented by scattering parameter files. These files are typically generated from the characterisation of the devices. The impedance matrices of the devices are determined, which are eventually combined with the overall impedance matrix of the system. The interface itself was found to be somewhat limited and awkward. The limitations were primarily with the generation of the circuit drawing, eg. curved lines could not be generated. The interface was awkward in that once the circuit drawing was complete, the drawing has to be re-traced to specify the circuit area requiring segmentation.

However the electromagnetic field based circuit simulator EMsim^{TM} can be used successfully to calculate accurately the current distribution along the structure. With the current distribution known, the radiation characteristics of the structure can be determined as outlined in the following section.

3.3 General Theory of Far-Field Calculation

For this particular situation, the current distribution on an arbitrarily shaped microstrip line is a known quantity. The radiation pattern, in terms of co- and cross-polarization components, thus can be calculated. Initially, a free-space Green's function was used; however, it was found necessary to obtain a more accurate calculation of the far-field pattern. Thus a microstrip Green's function was used.

3.3.1 Free Space Green's Function

In general, the field due to an electric source distribution may be determined from [72],

$$\bar{E}^e = -j\omega\mu A + \frac{1}{j\omega\varepsilon}\nabla\left(\nabla\cdot\bar{A}\right) \tag{3.7}$$

where A is the vector potential

$$\bar{A}(r) = \frac{1}{4\pi}\int_v \bar{J}(\bar{r}')\, G(\bar{r},\bar{r}')\, dr'$$

As a first approximation to calculating the far field pattern, the sources considered are the true current source and its image source located a distance z below the ground plane. Thus the free space Green's function may be used and (3.7) is reduced to (3.8), as the first term is dominant in the far field.

$$\bar{E}^e = -j\omega\mu\bar{A} \tag{3.8}$$

where $\bar{A}(\bar{r}) = \frac{1}{4\pi}\int_v \bar{J}(\bar{r}')\frac{e^{-jkR}}{R}\, dr'$

The two field components, E_θ and E_ϕ, may be determined from the vector potential by :

$$E_\theta = -jk_o\zeta_o A_\theta \tag{3.9}$$

$$E_\phi = -jk_o\zeta_o A_\phi$$

where $A_\theta = A_x \cos\theta\cos\phi + A_y \cos\theta \sin\phi$

$A_\phi = -A_x \sin\phi + A_y \cos\phi$

where $A_x(\theta,\phi) = \sum_{i=1}^{n} I_i \sin\phi_i [-2 \sin A \sin B + j\, 2 \cos A \sin B]$

$A_y(\theta,\phi) = \sum_{i=1}^{n} I_i \cos\phi_i [-2 \sin A \sin B + j\, 2 \cos A \sin B]$

where $A = k_o(x_i \cos\phi + y_i \sin\phi)\sin\theta$

$B = k_o z_i \cos\theta$

ϕ_i describes the direction of the current

k_o is the free space wave number

ζ_o is the free space impedance

Thus equation (3.9) may be used to calculate the far field of an arbitrarily shaped microstrip antenna knowing the current distribution.

The procedure for analysing travelling wave antennas by using EMSim and calculating the resultant far field radiation patterns, based upon the free space Green's function, has been applied to several travelling wave antennas. The calculated radiation properties agreed with those expected, provided the relative permittivity of the antenna substrate was low. As the relative permittivity of the substrate increased (eg. Alumina,

ε_r=9.8), the accuracy of the calculated far fields degraded. Thus a Green's function accounting for the dielectric substrate in the far field calculation was deemed necessary.

3.3.2 Microstrip Green's Function

The utilization of a microstrip Green's function in the calculation of far fields has been presented in [73] and [74] by Ragheb and Shafai. A summary of the field calculation is presented here. The expressions for the electric field components have been determined in [73] and is repeated in Appendix II. As can be seen in equations (aII-4) - (aII-6) of Appendix II, the Sommerfeld integrals contain Bessel functions. However, in the far field (kr >> 1), the Bessel functions may be replaced by Hankel functions of the second kind to represent outward travelling waves. Again, for kr >> 1, the Hankel function can be represented by an asymptotic expansion. An asymptotic expansion is used as the argument of the function to be expanded approaches infinity. As an approximation to this series, the first term of this expansion is used [75]. Thus the Hankel function is represented by $H_n^{(2)}(\eta\rho) \cong j^n \sqrt{\frac{2j}{\pi\eta\rho}}\, e^{-j\eta\rho}$. The Sommerfeld integrals are now in a suitable form to evaluate. The integral can be divided into two parts, where one part represents the spatial waves and the other part represents the surface waves. In this calculation of the radiated fields the surface waves have been neglected. Thus the remaining integral may be evaluated using the method of steepest descent where the major contribution to the integration comes from the neighbourhood of the saddle point of the integrand. This facilitates the evaluation of the integral. The above is an effective technique in evaluating Sommerfeld integrals for the far field [75]. Applying this technique yields expressions for the far field [73] which are presented in Appendix II. Again, it is assumed that the current distribution is known. This quantity is determined by the circuit simulator.

The power gain can be calculated from the relationship [76]

$$G(\theta,\phi) = \frac{\left[|E_\theta|^2 + |E_\phi|^2\right]}{30|I_{in}|^2\, \mathrm{Re}\{R_{in}\}} \tag{3.10}$$

where I_{in} and R_{in} are the input current and impedance

The field components and input parameters can be determined from the far field expressions and circuit simulator respectively.

The expressions for the far field, eq's (aII-7) and (aII-8), along with the expression for gain, eq'n (3.10), were coded to provide a post-processor to EMsim. This code is provided in Appendix III. This post processor calculates the radiation characteristics of the circuit/antenna being analysed by the circuit simulator. As a microstrip Green's function was used for the field calculation, more accurate results are expected for the cases where substrates with high permittivities are used, i.e. more accurate compared to the initial far field expressions where a free-space Green's function was used.

3.4 Verification of Design Methodology

The design methodology proposed is to use the circuit simulator EMsim followed by a post processor to calculate the radiation characteristics of active antenna structures. Qualitative results are given in this section with respect to passive travelling wave antennas while quantitative results are presented in section 4.5. There the calculated characteristics of an active antenna are compared to measured results.

Initially, EMsim was verified as an antenna design tool. This was done by studying the current distribution calculated by EMsim. The current distributions generated by EMsim for several travelling wave structures were compared to the current distributions generated by Numerical Electromagnetic Code (NEC), [51], which is a wire model program. The antenna structure is approximated as a wire structure and the moment method technique is used to solve the electric field integral equation as applied to the antenna geometry. Since NEC is limited to a free space environment above a perfect conducting ground plane, the relative permittivity of a substrate was set equal to one. The geometry of the travelling wave antenna is given in Figure 3.3. Both magnitude and phase of the current distribution generated by EMsim and NEC are presented in Figures 3.4 a) and b) respectively. As can be seen, both analysis packages generate the expected current distribution. That is, a continuous phase progression and a decrease in current magnitude along the antenna. The ripples observed in the magnitude plot are due to the reflections at the corners of the antenna.

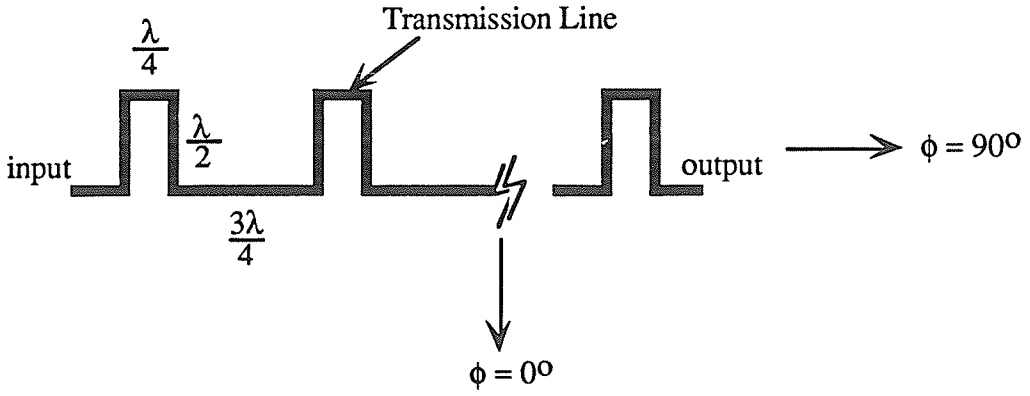

Figure 3.3 : Passive circularly polarized rampart line travelling wave antenna.

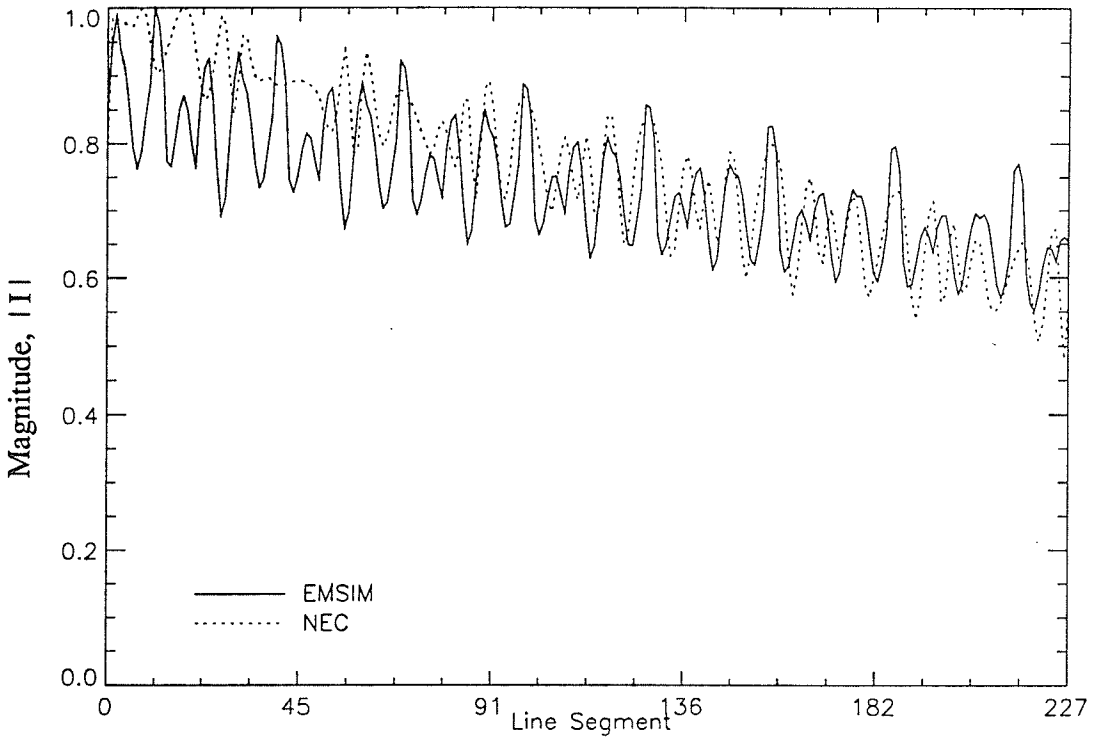

a) Current magnitude along antenna, EMsim and NEC

Figure 3.4 : Calculated current distribution of rampart line antenna.

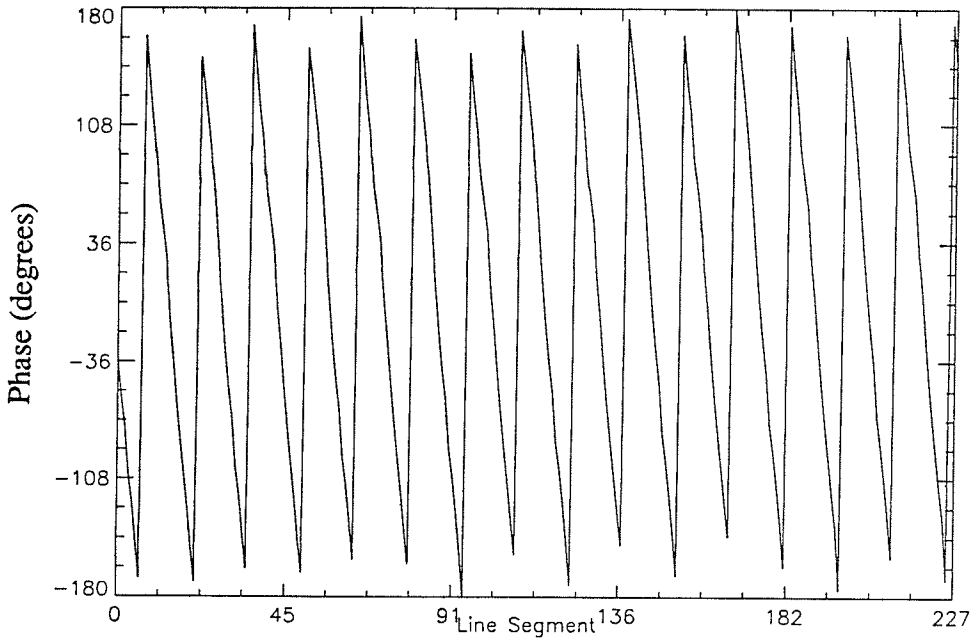

b) Current phase along antenna, EMsim

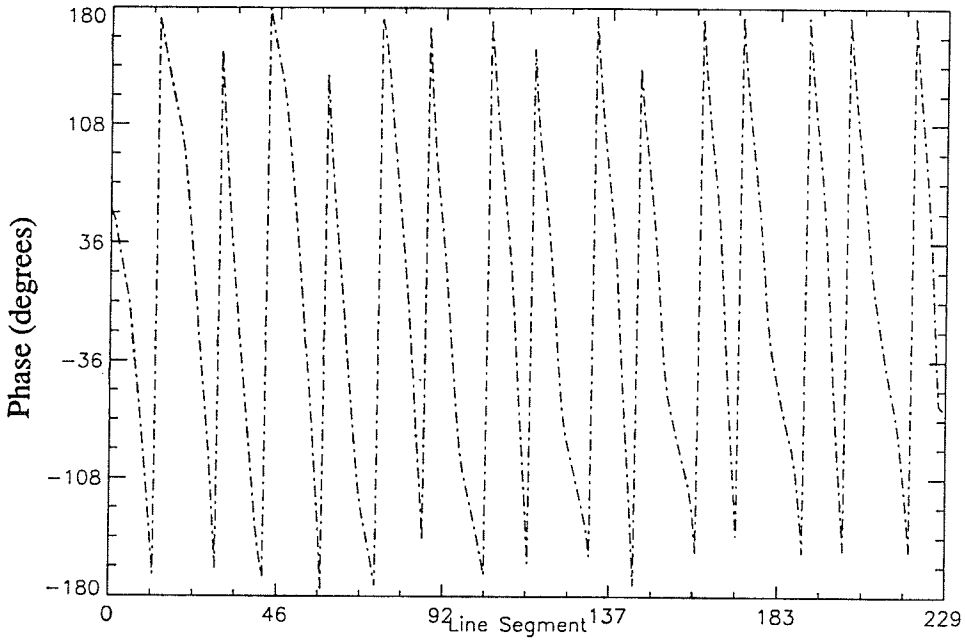

c) Current phase along antenna, NEC

Figure 3.4 : (Cont.)

Next the combination of EMsim with the developed post processor was studied. Two passive travelling wave antenna were modelled; the rampart antenna of Figure 3.3 and the 4-arm travelling wave antenna [77] given in Figure 3.5. Both antennas generate a circularly polarized field. The rampart antenna was modelled having a substrate permittivity of one, while the 4-arm antenna was modelled having substrate permittivities of 1.0, 2.55, and 9.8.

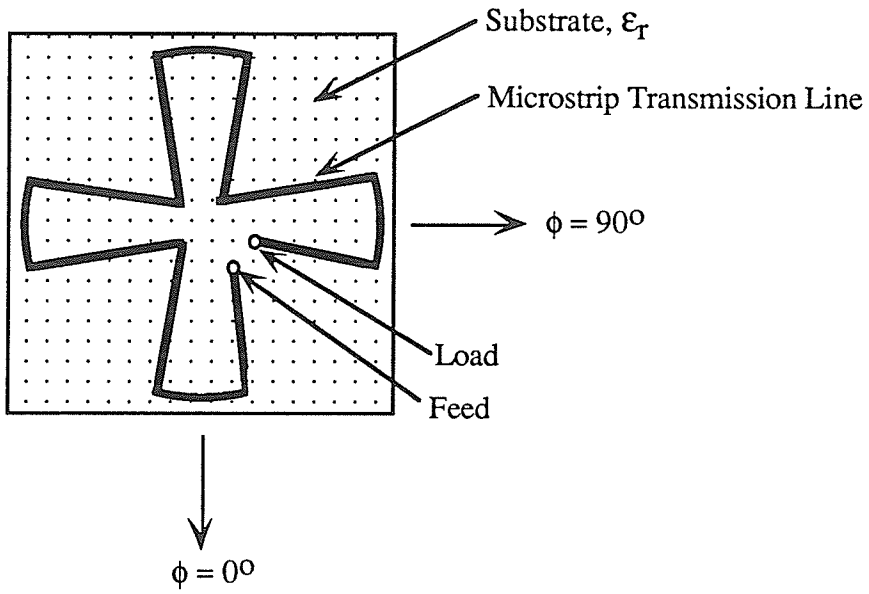

Figure 3.5 : Passive circularly polarized 4-arm travelling wave antenna

The calculated patterns of the rampart antenna (ε_r = 1.0, h=λ/20, f=3 GHz) are given in Fig. 3.6. As expected, based upon the aperture size, the pattern in the ϕ=0^o plane is broad while the pattern in the ϕ=90^o plane is narrow. These radiation characteristics have been confirmed with experimental results given in [78]. The rampart antenna was also modelled with NEC and similar radiation characteristics were generated (Figure 3.7).

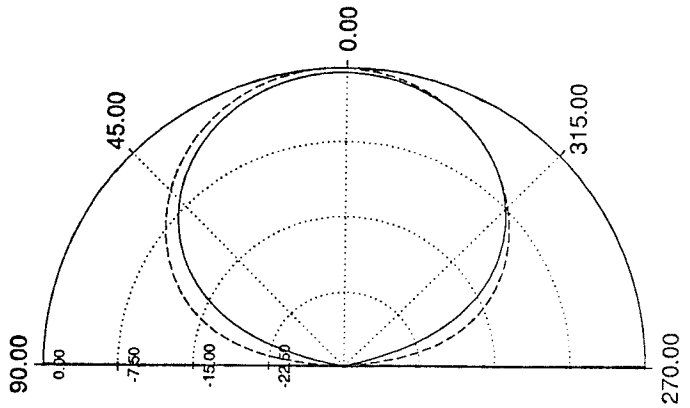

a) $\phi=0^o$

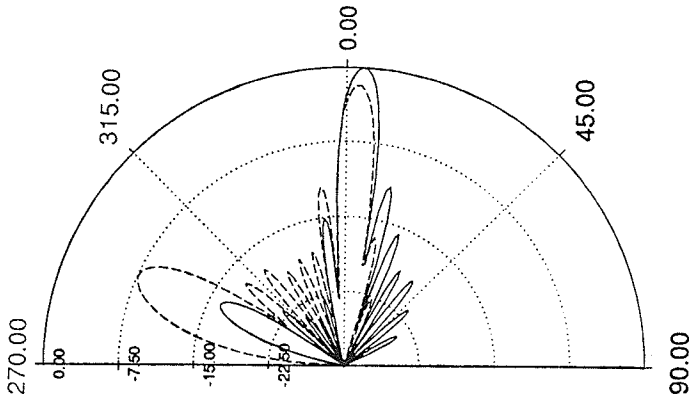

b) $\phi=90^o$

Figure 3.6 : Calculated radiation patterns of modelled circularly polarized rampart antenna, —— E_θ - - - E_ϕ

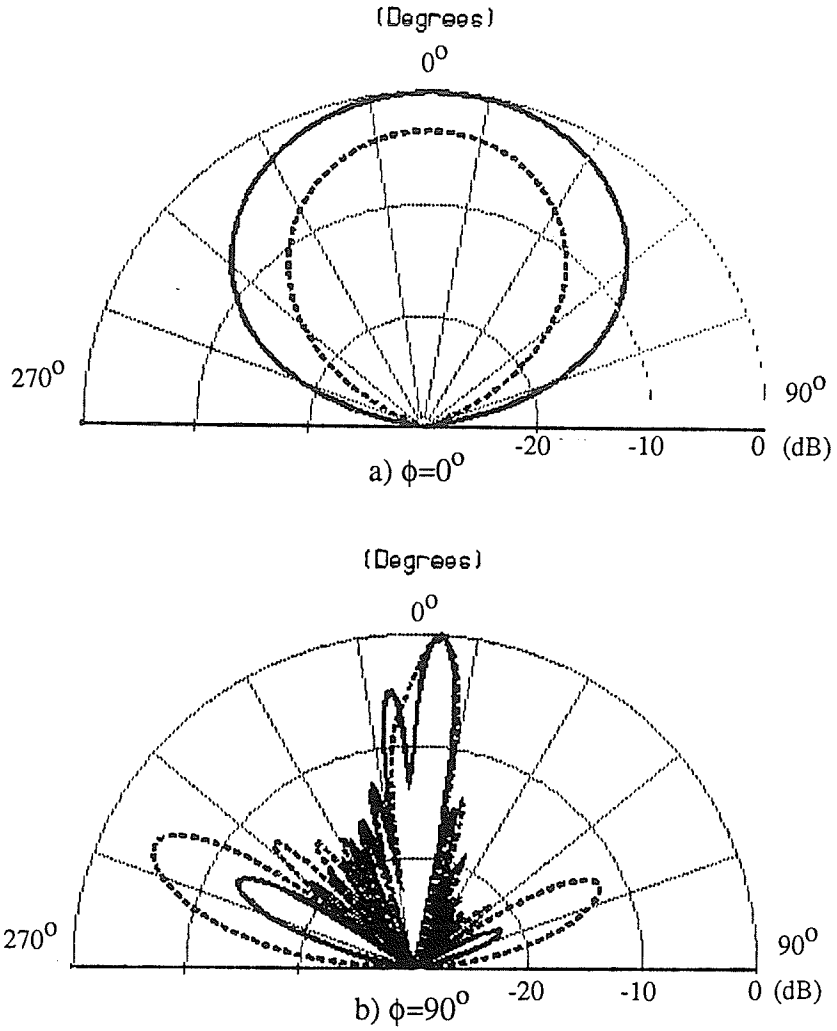

Figure 3.7 : Calculated radiation patterns from NEC of modelled circularly polarized rampart antenna, —— E_θ, - - - E_ϕ.

The passive 4-arm antenna of Figure 3.5 was also modelled having similar parameters ($\varepsilon_r = 1.0$, $h=\lambda/20$, f=3.0 GHz). The calculated pattern at the centre frequency is given in Figure 3.8 a). This can be compared to the same structure modelled with NEC [77] (Figure 3.8 b)). In accordance to [77] both modelling packages predict a circularly polarized broadside pattern. Both NEC and the proposed modelling technique predict a half power beam width of approximately 40^o.

The 4-arm travelling wave antenna was also modelled where it was situated on an Alumina substrate (ε_r = 9.8, h=λ/20, f=3.0 GHz). The more rigourous post processor, based upon a microstrip Green's function was developed for cases such as this. Elevation patterns in two planes of the antenna are given in Figure 3.9. Both magnitude and phase are calculated and presented. As can be seen, the two field components are approximately equal in magnitude and in phase quadrature in both planes at the broadside direction. These are the expected results for this antenna [77]. A broader half power beamwidth can be noted when comparing these patterns to Figure 3.8. The broader beamwidth is an expected characteristic as the high relative permittivity of the substrate yields a reduced aperture size. The radiation characteristics over a range of frequencies were also calculated (Figure 3.10). Inherent with travelling wave antennas is the squinting of the main beam as frequency deviates from the centre frequency, f_c. The squinting is caused by the shift in electrical length of the antenna. As frequency deviates from the centre frequency, the beam squints off broadside. Eventually a centre null is formed. These characteristics are predicted with the modelling procedure (Figure 3.10) and have also been verified experimentally in Figure 3.11. The results presented are for frequencies which exceed the centre frequency. Similar results were obtained for frequencies below the centre frequency, with the beam squinting in an opposing direction.

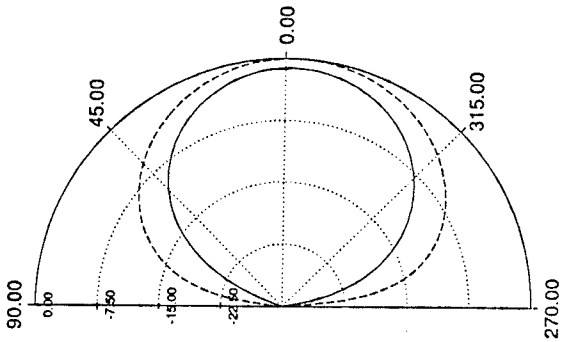

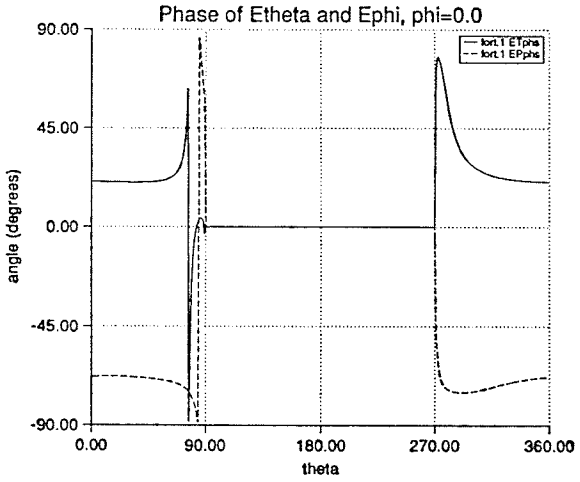

i) Magnitude ii) Phase

a) $\phi=0^o$

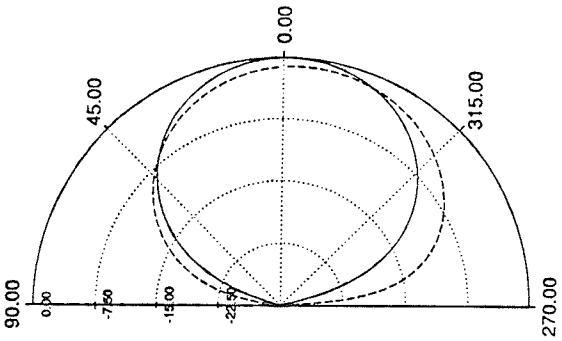

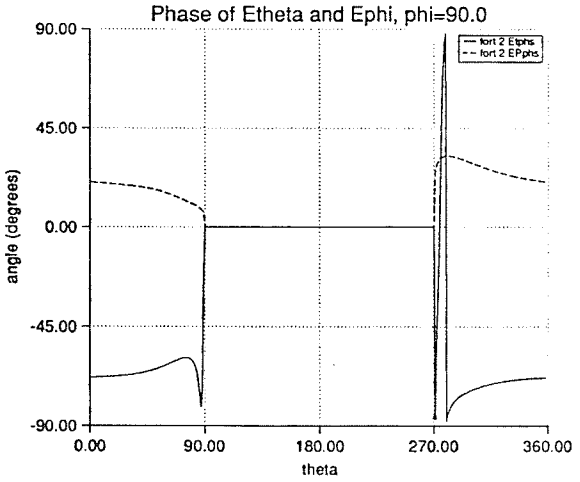

i) Magnitude ii) Phase

b) $\phi=90^o$

Figure 3.9 : Magnitude and phase of field components of passive 4-arm antenna, $\varepsilon_r = 9.8$, —— E_θ, - - - E_ϕ.

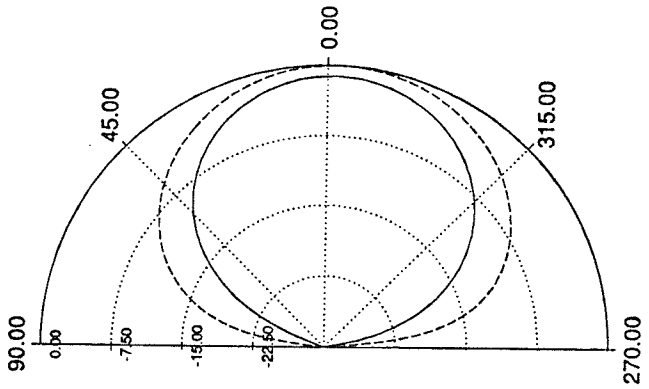

a) Calculated, f=3.1 GHz

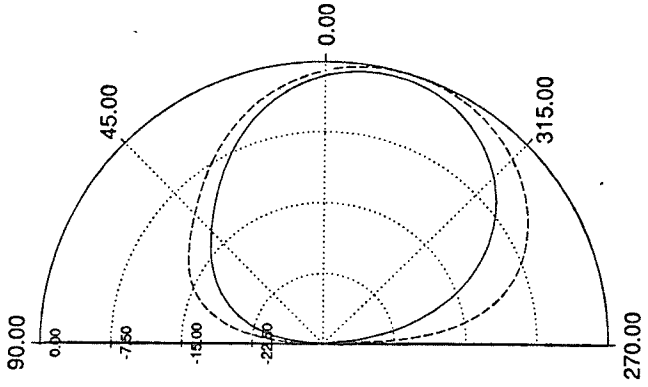

b) Calculated, f=3.3 GHz

Figure 3.10 : Calculated radiation patterns of passive 4-arm antenna ,ε_r=9.8, —— E_θ,- - -E_ϕ, $\phi=0^o$

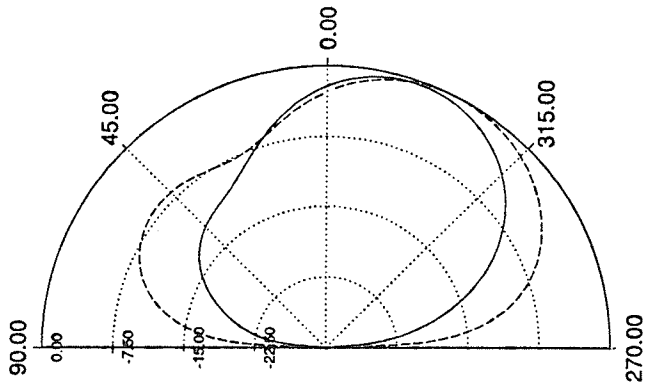

c) Calculated, f=3.4 GHz

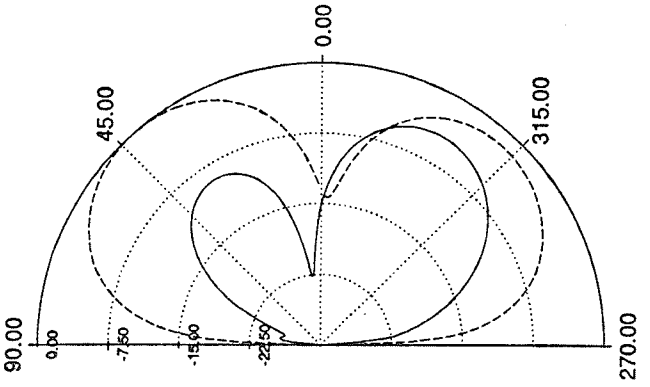

d) Calculated, f=3.6 GHz

Figure 3.10 : (cont.)

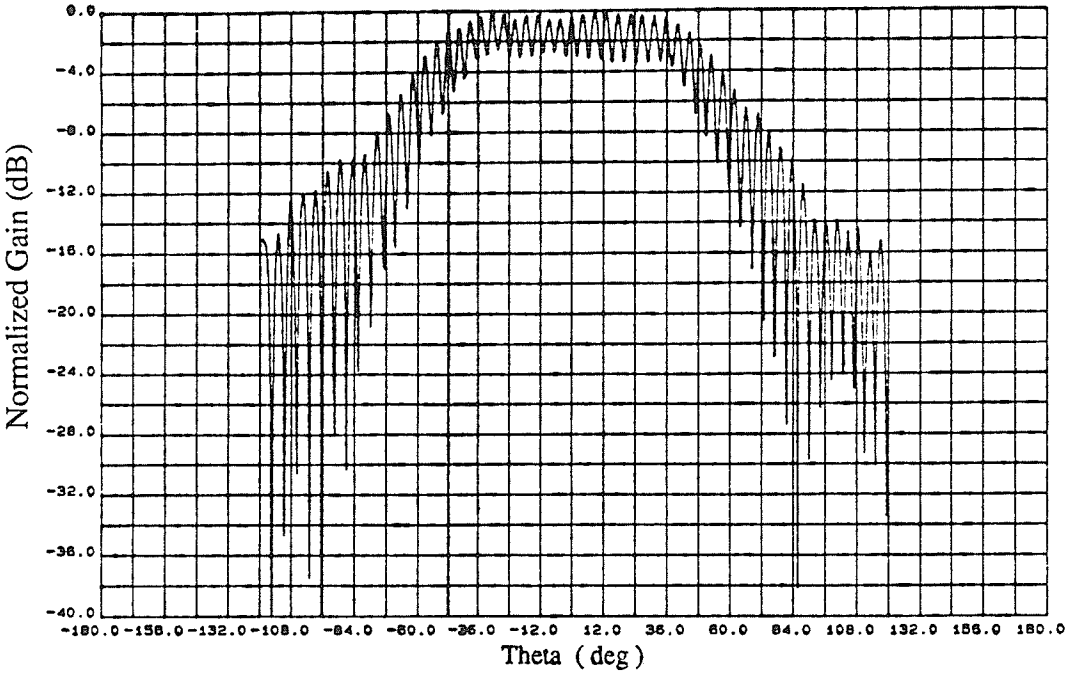

a) Measured, f=3.1 GHz

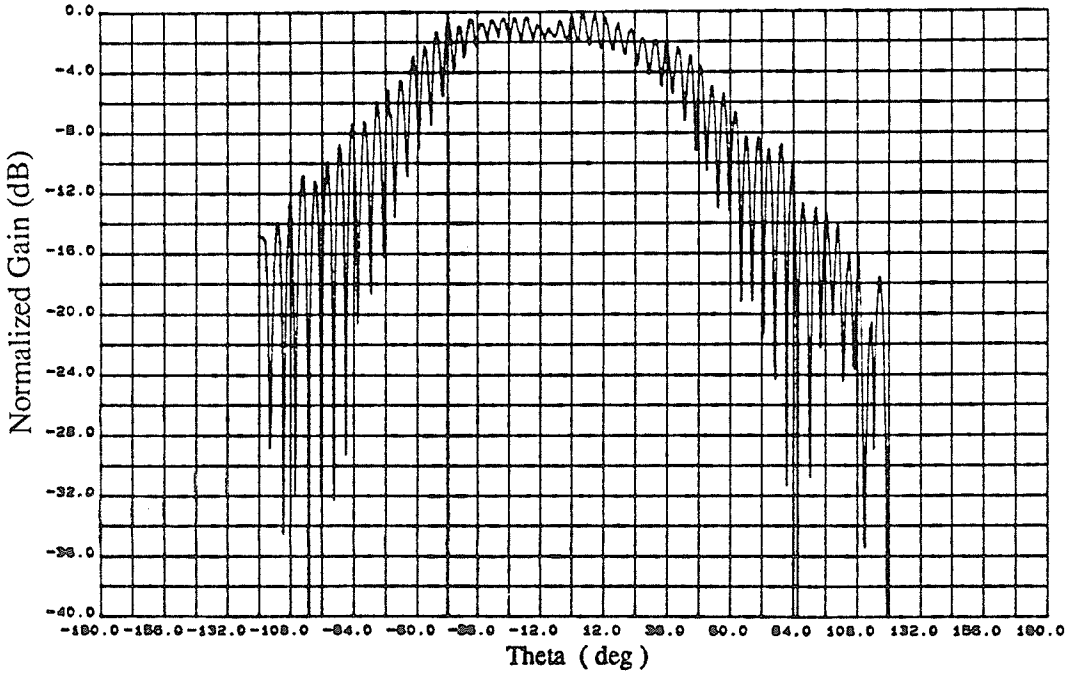

b) Measured, f=3.2 GHz

Figure 3.11 : Measured radiation patterns of passive 4-arm antenna ,ε_r=9.8, ϕ=0°

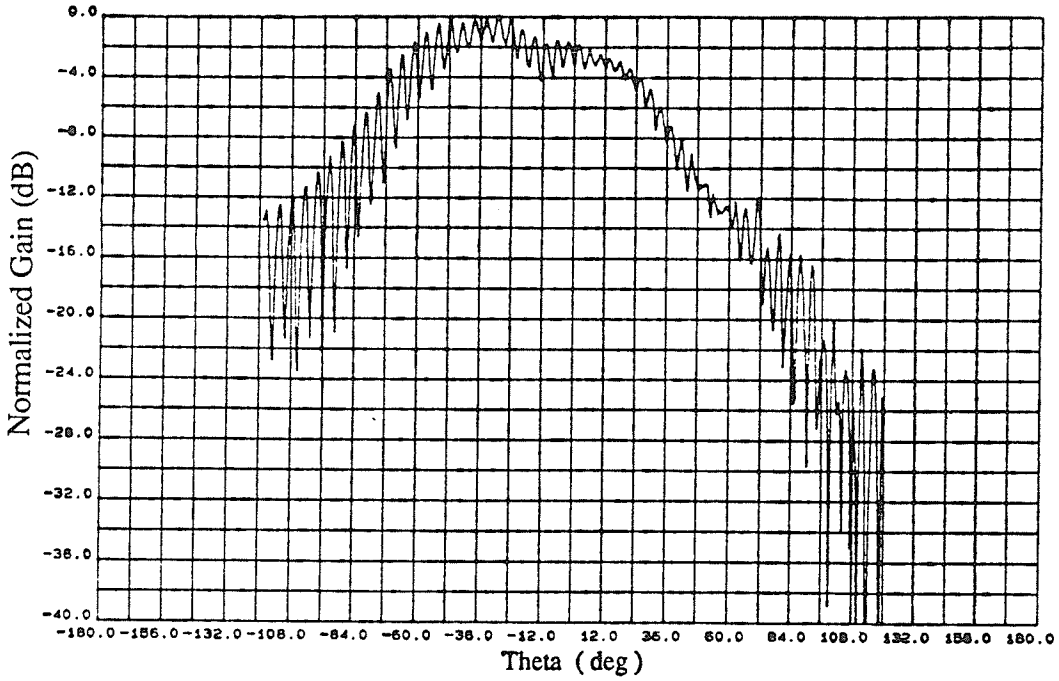

c) Measured, f=3.4 GHz

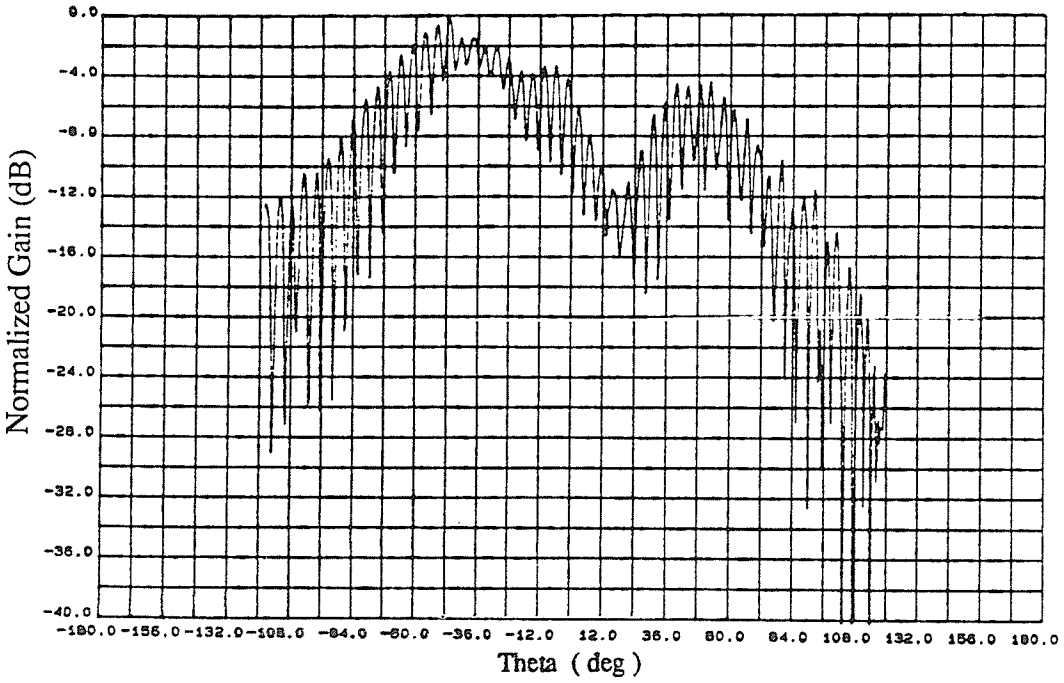

d) Measured, f=3.5 GHz

Figure. 3.11 : (cont.)

3.5 Noise Analysis of Active Antennas

The active antennas considered in this study are travelling wave in nature with active devices integrated along the structure. Thus in general, the resultant structure is a distribution of microstrip transmission lines and active devices. A block diagram is depicted in Figure 3.12. If this type of antenna were to be used in a receive application then the noise temperature of the antenna must be determined. This section presents a theoretical analysis of the noise temperature of the proposed active antenna. The noise model is validated with experimental results given in Chapter 4.6.

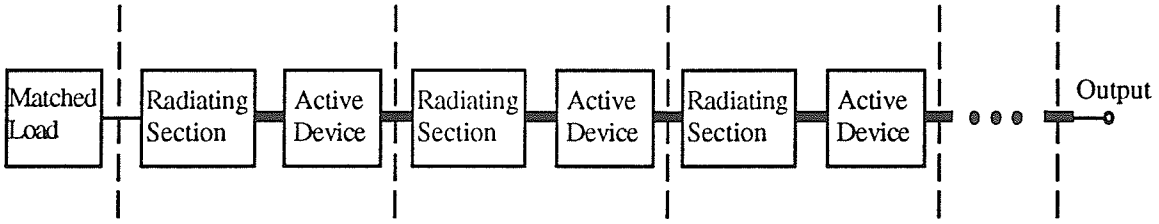

Figure 3.12 : Block diagram of a receive active antenna.

Within a typical communication system, the amplification stage and other active devices follow the passive radiator. The noise contributions from each stage can be clearly segregated and the noise calculation of the system can be determined based upon a cascade network of noise sources [49]. The developed active antennas introduce an interesting problem when calculating the system temperature. For this particular situation, the active devices cannot be separated from the receive antenna because they are an integral part of the antenna. Each section of the antenna contributes to the overall system noise temperature. These contributions are weighted by factors such as radiation efficiency and the gain/loss of each device. The noise variables involved with this type of antenna may be identified to be 1. device noise, 2. sky noise, and 3. ohmic losses. These noise sources combine in some manner to produce an output noise temperature. This is graphically depicted in Figure 3.13.

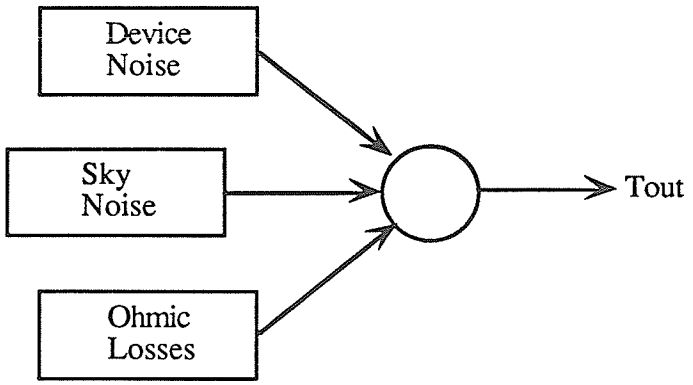

Figure 3.13: Sources of noise for an active antenna.

An equivalent noise model of the general structure, Figure 3.12, is presented in Fig. 3.14. The noise model is a circuit representation of the antenna where the antenna is replaced with a combination of resistors, attenuators, and active devices. The matched termination inherent with travelling wave antennas is represented by the resistor R_o while the radiation resistance is represented by R_N. Each resistor is referenced to its environment temperature, thus R_N is referenced to the sky temperature. The ohmic attenuation due to the microstrip transmission line is represented by L_N, referenced to its environment temperature, T_{L_N}. The gain/loss of each active device is represented by G_N where the noise figure of each active device is expressed in terms of temperature by T_{A_N}.

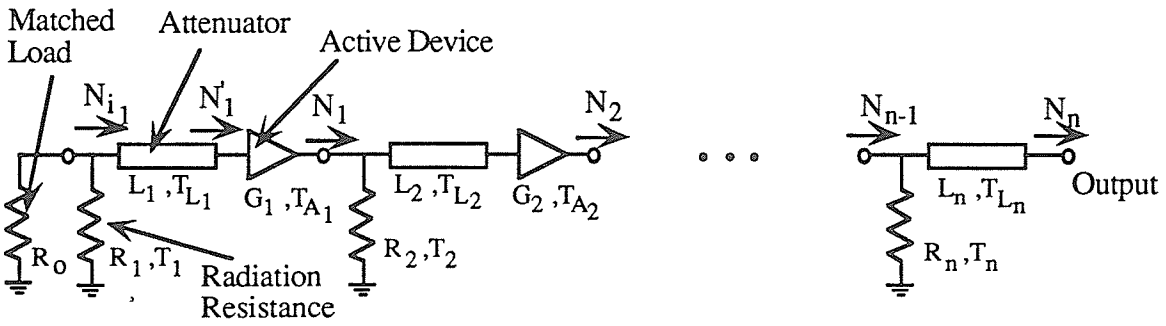

Figure 3.14 : Noise model for general configuration of travelling wave active antenna

The output temperature of the antenna is determined by calculating noise in a sequential manner, commencing at the section furthest from the output port. The two parallel resistors can be considered as parallel noise sources. Superposition is applied to determine the total noise power available to the attenuator, N_{i_1}, as outlined below.

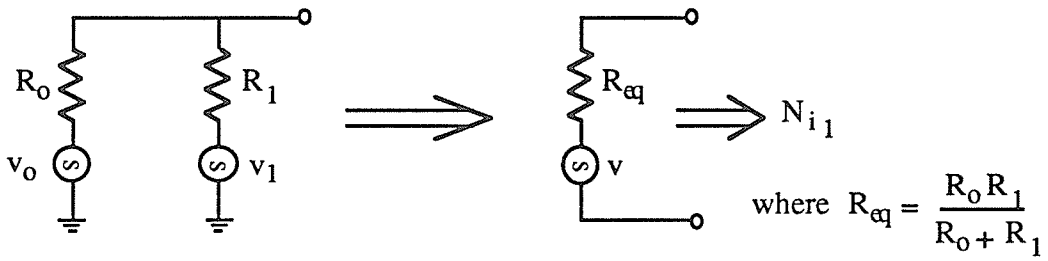

I/ Determine noise power due to v_o :

$$v = \frac{v_o R_1}{R_o + R_1}$$

$$N_i^{v_o} = \frac{\overline{v}^2}{4 R_{eq}}$$

$$= \frac{\overline{v_o}^2 R_1}{4 R_o (R_o + R_1)}$$

but $\overline{v_o}^2 = 4 k T_o R_o B$

$$\therefore N_i^{v_o} = \frac{k B T_o R_1}{(R_o + R_1)}$$

In terms of conductance, $G = \frac{1}{R}$

$$\therefore N_i^{v_o} = \frac{k B T_o G_{R_o}}{(G_{R_1} + G_{R_o})} \qquad (3.11)$$

II/ Determine noise power due to v_1 :

$$\text{Similarly,}\quad N_i^{v_1} = \frac{k\,B\,T_1\,G_{R_1}}{(G_{R_1} + G_{R_o})} \tag{3.12}$$

$$N_{i_1} = N_i^{v_o} + N_i^{v_1}$$

$$\therefore\ N_{i_1} = k\,B\left(\frac{T_o\,G_{R_o} + T_1\,G_{R_1}}{G_{R_1} + G_{R_o}}\right) \tag{3.13}$$

The noise power at the output of the first active device, including the effect of the attenuator L_1, can be determined to be

$$N_1 = k\,B\,T_{N_1} \tag{3.14}$$

where $T_{N_1} = \frac{G_1}{L_1}[T_{i_1} + (L_1 - 1)\,T_{L_1}] + G_1\,T_{A_1}$

where $T_{i_1} = \frac{T_o}{1 + g_{r_1}} + \frac{T_1 g_{r_1}}{1 + g_{r_1}}$

where g_r is the normalized radiation conductance

Assuming maximum power transfer, i.e. a matched system, the first section may be replaced by a matched resistor with temperature T_{N1} [76]. This resistor in parallel with R_2 is the input to the next stage.

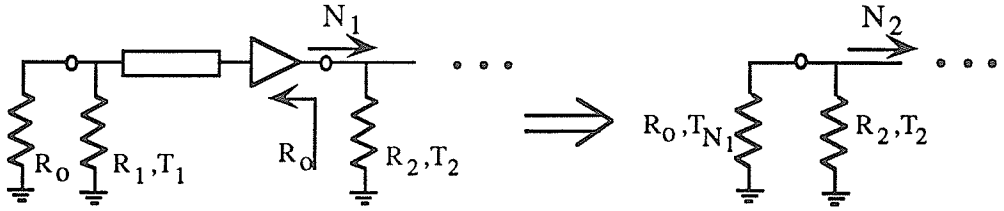

This procedure is repeated until the output temperature of the system is obtained. It is found to be

$$T_{out} = \frac{T_{i_n}}{L_n} + \frac{(L_n - 1)\,T_{L_n}}{L_n} \tag{3.15}$$

where T_{i_n} can be calculated from T_{N_1} of equation (3.14) using the following recursive relationships

$$T_{i_n} = \frac{T_{N_{n-1}}}{1 + g_{r_n}} + \frac{T_n g_{r_n}}{1 + g_{r_n}}$$

and

$$T_{N_n} = \frac{G_n}{L_n}[T_{i_n} + (L_n - 1)\, T_{L_n}] + G_n\, T_{A_n}$$

where n is the number of radiating sections.

The radiation conductance can be determined from a travelling wave array of slot radiators as given in [80]. There the radiation conductance is related to the amount of power radiated by each slot. This relationship is used here where slot radiation is replaced by the radiation efficiency of each arm, i.e. $\eta_{arm} = \frac{g_r}{1 + g_r}$. There is however a limit to the radiation efficiency of each section such that the matched condition remains valid. As an example, demanding 90% radiation efficiency from each section will produce mismatches as the characteristic impedance changes. Therefore the developed noise model will not be accurate. An acceptable limitation on the radiation efficiency that one can demand from each arm is determined below. It is assumed that the matched condition remains valid for S_{11}< -10 dB, i.e. reflection coefficient maximum is 0.1. It is desired that $z_L = 1.0$ and z_o is dependent upon the parallel combination as

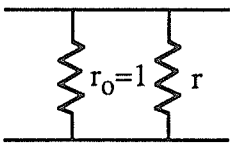

$$z_o = \frac{r}{r+1}$$

$$|\Gamma| = \frac{Z_L - Z_o}{Z_L + Z_o}$$

$$\therefore |\Gamma| = \frac{1 - \frac{r}{1+r}}{1 + \frac{r}{1+r}}$$

for $|\Gamma| = 0.1$, r=4.5

but g=1/r, $\therefore$ $g_r = 0.222$

This is the upper limit for the validity of the noise model, i.e. g_r=0.222. This translates to a radiating section efficiency of 18.18%.

Based upon eq'n (3.15), the output temperature of an active antenna can be calculated. This expression has been used to calculate the output temperature of the active antennas presented in Chapter 4. The limitation within this model is that a matched system is assumed. Once this condition is violated the model is not valid.

3.6 Discussion

The type of active integrated antennas studied may be generalized as a travelling wave antenna with active devices integrated along the radiating structure. As no software is commercially available to analyse such a structure, a design methodology was developed. An electromagnetic based circuit simulator is being used in conjunction with a post processor. The circuit simulator is the analysis tool to determine the current distribution and the post processor is being used to calculate the far field radiation patterns. The procedure has been verified with the analysis of passive travelling wave antennas. In addition to the radiation characteristics, a noise model has also been developed. The verification of this model is given in Chapter 4.

A technique and model has been presented where an arbitrarily shaped active integrated travelling wave antenna may be analysed. Radiation characteristics such as pattern and gain may be calculated as well as a noise analysis of the entire structure. The noise analysis incorporates the effects of the environment, microstrip, and the integrated active devices.

CHAPTER 4 : THE DESIGN AND VERIFICATION OF AN ACTIVE ANTENNA

4.1 The Design of an Active Integrated Antenna

The work within this thesis has been focused on travelling wave structures. This type of structure allows intuitive understanding of the energy propagation along the structure and how active devices may be used to alter this distribution. Previous work [77] produced a circularly polarized passive microstrip travelling wave antenna. The radiation characteristics of this antenna were based upon a circular loop. A circular loop was studied in [81] using a continuous radiating current of the form

$$I_n = \left[a_n \cos(n\phi') + b_n \sin(n\phi')\right]\hat{\phi}\,,\ n>0 \tag{4.1}$$

which produce the following far field patterns;

$$E_\theta = f_n(\theta)\,[a_n \sin(n\phi) - b_n \cos(n\phi)] \tag{4.2a)}$$

where $$f_n(\theta) = \frac{-\omega\mu a}{4}\frac{e^{-jkr}}{r} j^n \cos\theta\,[J_{n+1}(k a\sin\theta) + J_{n-1}(k a\sin\theta)] \tag{4.2b)}$$

and $$E_\phi = g_n(\theta)\,[a_n \cos(n\phi) + b_n \sin(n\phi)] \tag{4.3a)}$$

where $$g_n(\theta) = \frac{-\omega\mu a}{4}\frac{e^{-jkr}}{r} j^n\,[J_{n+1}(k a\sin\theta) - J_{n-1}(k a\sin\theta)] \tag{4.3b)}$$

The derivation for these equations can be found in [77].

It was found that by selecting $a_n=1$ and $b_n=j$, equation (4.1) produced conditions suitable for obtaining circular polarization. Substituting these values into equations (4.1), (4.2a)) and (4.3a)) reduces the current to

$$I_n = e^{jn\phi'} \tag{4.4}$$

and the far fields to

$$E_\theta = f_n(\theta)\, e^{j(n\phi - \frac{\pi}{2})} \tag{4.5}$$

$$E_\phi = g_n(\theta)\, e^{j(n\phi)} \tag{4.6}$$

Equations (4.5) and (4.6) show that the two field components are 90° out of phase, but with unequal magnitudes. This condition would result in elliptically polarized waves; however, circular polarization can be obtained if the magnitudes are equal. This can be achieved with the proper selection of loop radius. Examining equations (4.2b)) and (4.3b)) shows that the radiation characteristics are dependent upon the Bessel functions. Each order of Bessel function is referred to here as a mode. For n=1, mode 1, a zero order Bessel function is present and this will generate a broadside pattern since

$$J_m(0) = 1 \qquad \text{for } m=0$$

$$J_m(0) = 0 \qquad \text{for } m\geq 1$$

All other values of n produce higher order Bessel functions (modes) resulting in $f_n(0^o) = g_n(0^o) = 0$. This will generate a conical shaped pattern with a centre null on the loop axis. As the mode of operation increases (increasing n), the resultant radiated pattern approaches the plane of the loop. Thus by selecting various orders of the Bessel function one can change the radiation characteristics of the loop.

To obtain circular polarization, a radiating current in the form of equation (4.4) is required. Breaking up the radiating current into discrete elements is one variation [81]. This can be carried out as follows.

$$I_n = I\Delta l \sum_{m=1}^{M} e^{j\delta_m} \tag{4.7}$$

with $\sum_{m=1}^{M} \delta_m = n2\pi$

where $I\Delta l$ is the discrete current element
M is the total number of elements
δ_m is the phase of each element

The condition of $\sum_{m=1}^{M} \delta_m = n2\pi$ was stipulated in order to satisfy the conditions of a loop where phase progresses as $n2\pi$.

The radiation properties of the developed active antenna are based upon the above theory. It was anticipated that an antenna with discrete radiating current elements could be realized with a travelling wave microstrip antenna where the current elements are interconnected with active devices (Fig 4.1). The active devices within the antenna would allow the alteration of the current magnitude and/or phase along the outer circumference of the antenna.

This would yield an antenna with variable gain, size and radiated pattern. In addition to the enhanced gain which the amplifiers would contribute if used, the active devices could be used to "fine tune" a radiated pattern or reconfigure the pattern. The pattern may be reconfigured to different modes of operation by varying the current distribution to satisfy the necessary conditions outlined previously. For example, the active devices could be biased in one state for a 2π phase progression ($n2\pi$, where n=1 (mode 1)) along the outer circumference of the antenna producing a circularly polarized broadside pattern. The devices could then be biased to a second state such that a 4π phase progression ($n2\pi$, where n=2 (mode 2)) along the outer circumference of the antenna is generated. This would satisfy the conditions necessary to produce a conical shaped

pattern. The modal operation of this antenna has been investigated and is reported on in Chapter 5.

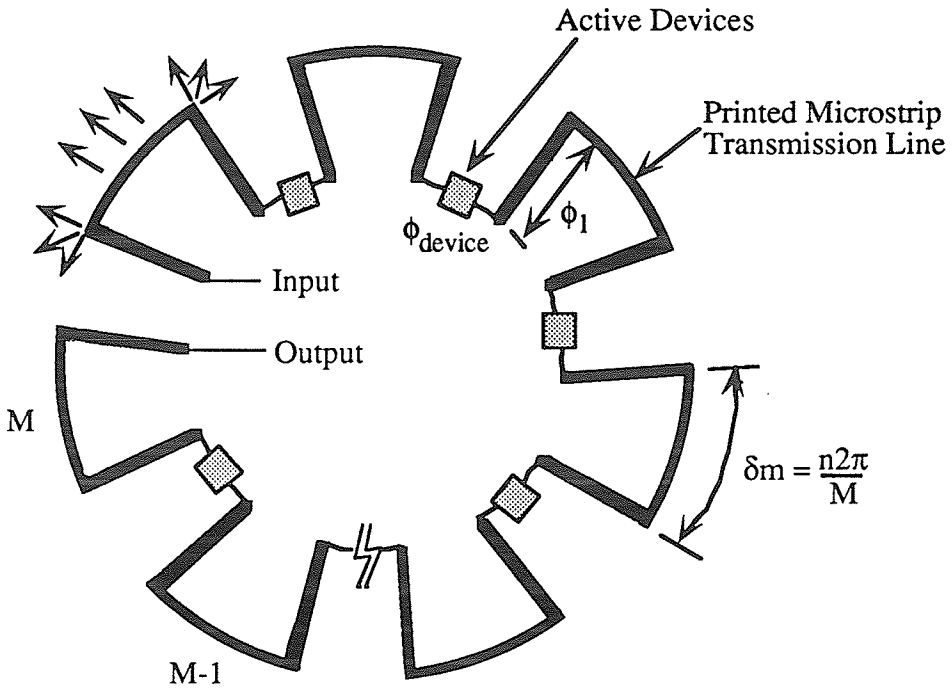

Figure 4.1: Generalized structure of proposed active integrated antenna.

4.2 Modelling of the Active Integrated Antenna

An active integrated antenna, based upon the generalized structure of Figure 4.1, was numerically modelled using the design methodology presented in Chapter 3. The simulated antenna consisted of four radiating "arms" interconnected by amplifiers (ε_r=2.94, h=0.06", f_c=3.0 GHz (Figure 4.2). A broadside pattern, mode 1 operation, i.e. n=1, was selected as the design criterion. This requires a 2π phase progression along the outer circumference of the loop. A structure with four radiating segments requires each segment to be $\lambda/4$ in length to satisfy this phase progression. Thus the phase progression from the end of one segment to the beginning of the next is required to be transparent. This may be realized with the proper combination of transmission line and active devices. For this particular antenna, the active devices are amplifiers which function as both amplifiers and phase shifters. Each amplifier has an associated phase shift, ϕ_{amp}, at the operating frequency of the antenna, thus the phase delay between radiating segments may be achieved provided the total phase shift between each segment is maintained at 360^o ($\phi_{amp} + 2\phi_l = 360^o$) (Figure 4.2). With the amplifiers operating at 0 dB gain, the active devices are simply phase shifters and the antenna should yield results similar to a circularly polarized loop. As the amplifiers increase in gain there should be a notable increase in antenna peak gain.

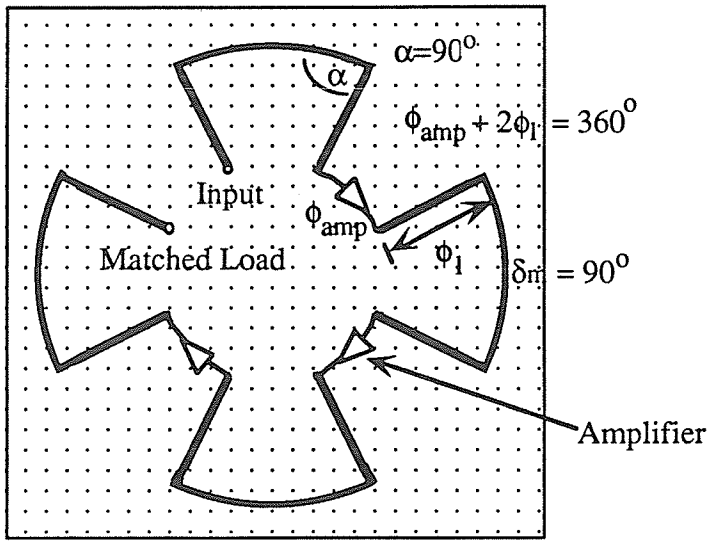

Figure 4.2 : Four arm active antenna for broadside operation.

The active antenna presented in Figure 4.2 was simulated using EMsim^{TM} and the developed post-processor. The amplifiers were incorporated by using scattering matrices. These matrices correspond with the scattering parameters of the devices used in the fabricated structure. The device characteristics are given in Appendix IV. The layout of the antenna as presented by the user interface is given in Figure 4.3.

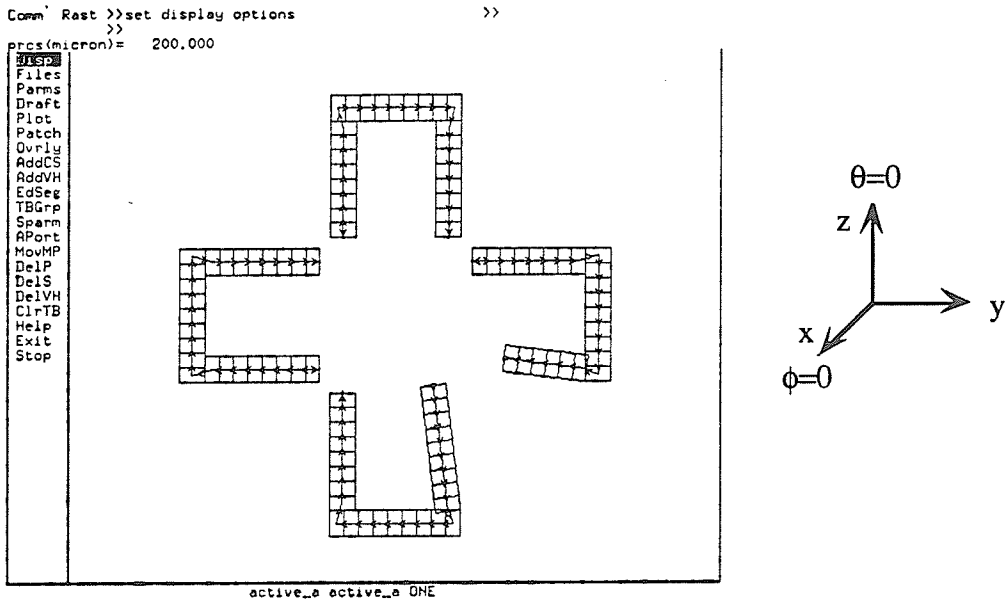

Figure 4.3 : Layout of active integrated antenna.

Initially, the case where the amplifiers are biased for 0 dB gain was studied. The resultant radiation characteristics should be similar to those of the passive 4-arm travelling wave antenna (Figure 3.5). A frequency sweep, from 2.5 GHz to 3.5 GHz, of the active antenna was simulated. The calculated radiation patterns are presented in Figure 4.4. As can be seen, the squinting behaviour of the travelling wave structure is predicted. The presence of a centre null as frequency deviates from the centre frequency is also predicted. According to the calculated results, the centre frequency is 3.1 GHz. The patterns of the centre frequency in two orthogonal planes are presented in Figure 4.5. The phase of the two field components are also presented. As can be seen, the field components are broadside, circular symmetric, equal in magnitude, and in phase quadrature.

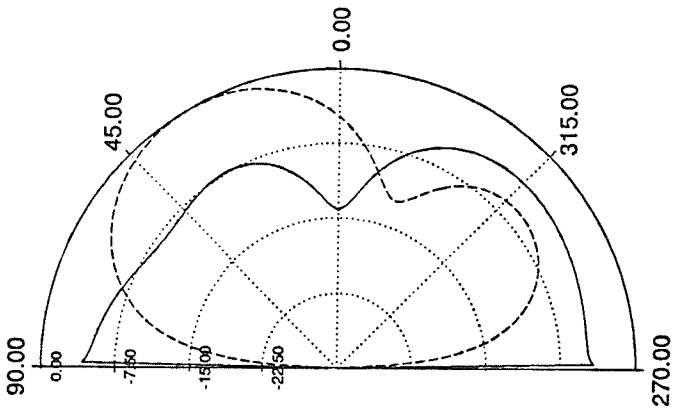

a) f=2.5 GHz

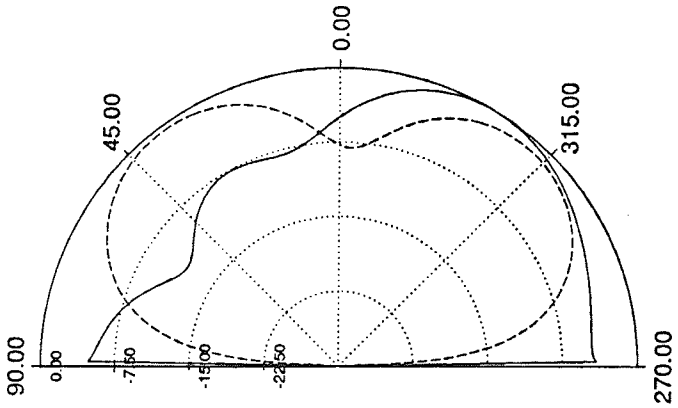

b) f=2.6 GHz

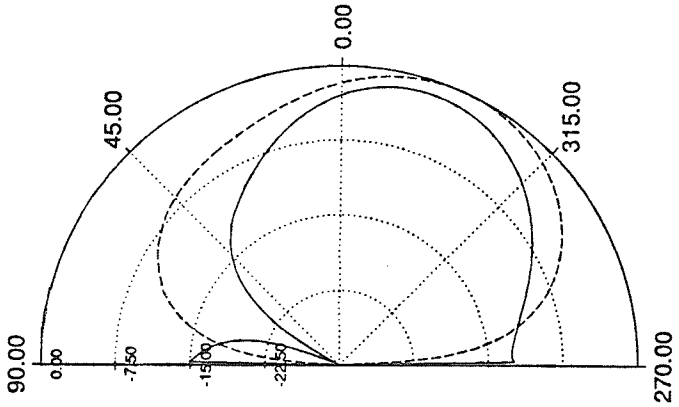

c) f=2.7 GHz

Figure 4.4 : Calculated patterns of active antenna, amps@0dB, $\phi=0^{o}$,—— E_{θ},- - -E_{ϕ}.

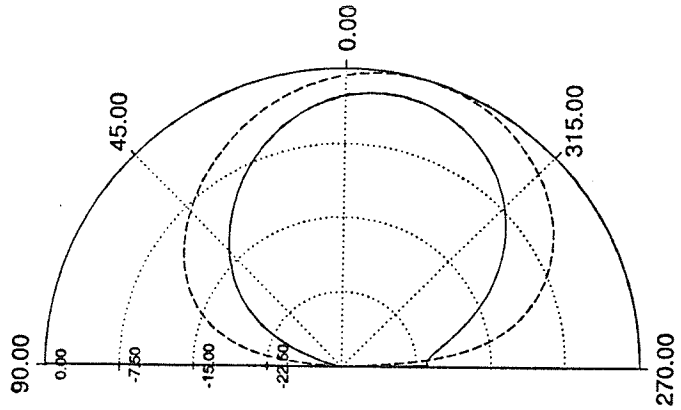

d) f=2.8 GHz

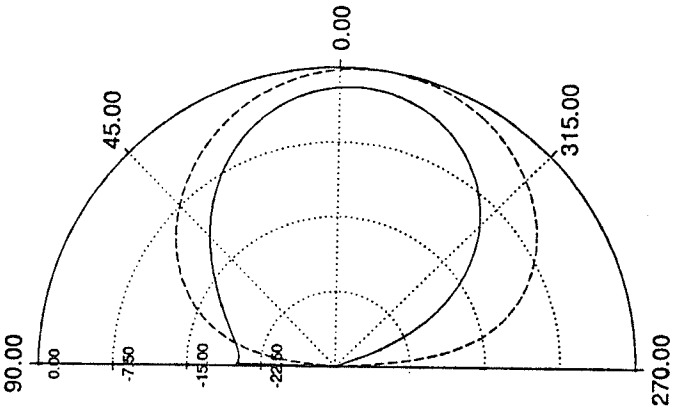

e) f=2.9 GHz

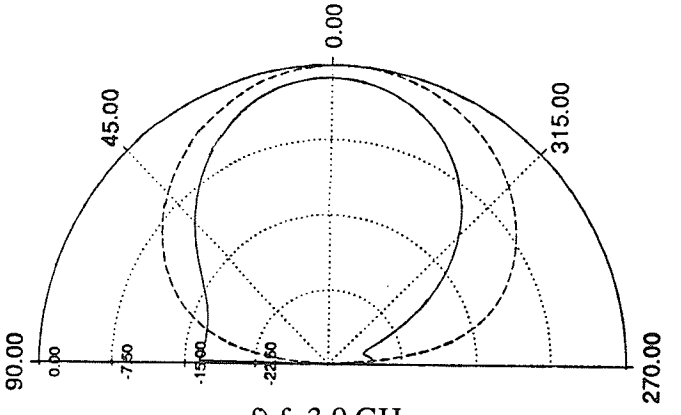

f) f=3.0 GHz

Figure 4.4 : (Cont.)

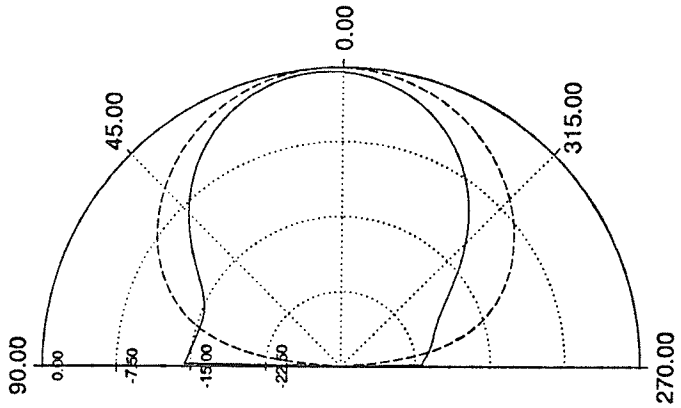

g) f=3.1 GHz

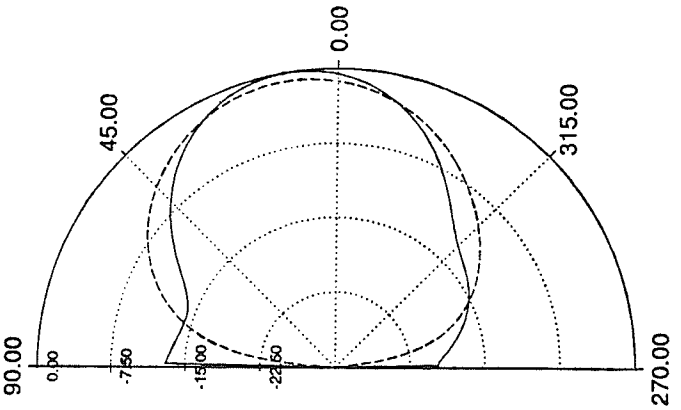

h) f=3.2 GHz

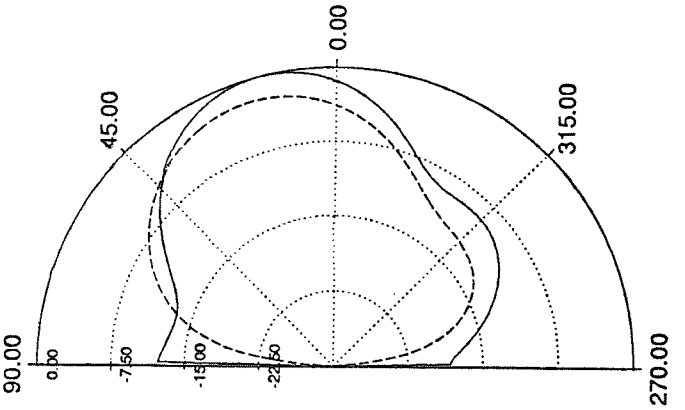

i) f=3.3 GHz

Figure 4.4 : Calculated patterns of active antenna, amps@0dB, $\phi=0^{o}$

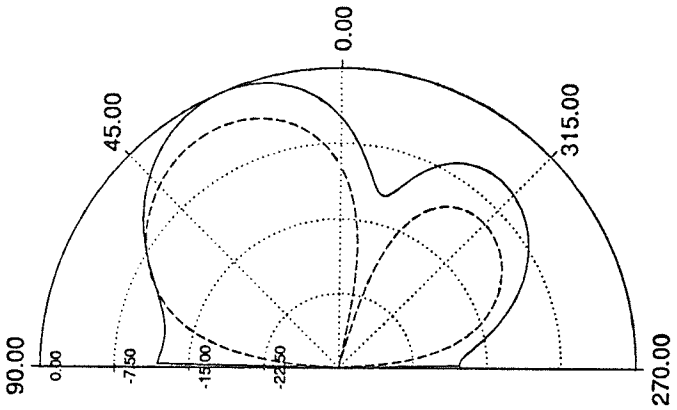

j) f=3.4 GHz

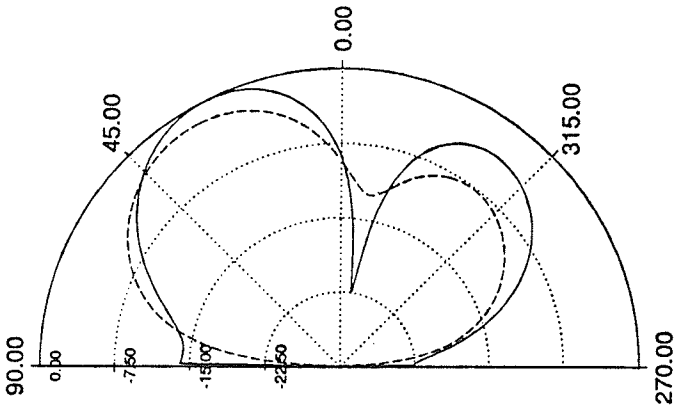

k) f=3.5 GHz

Figure 4.4 : (Cont.)

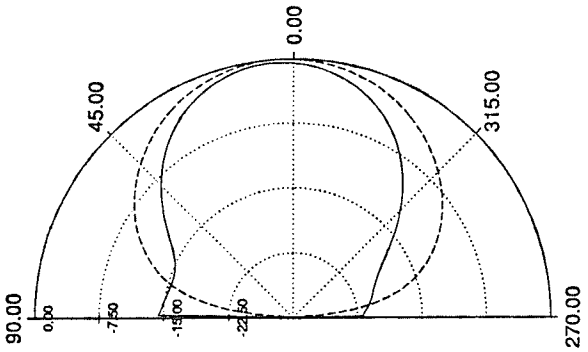

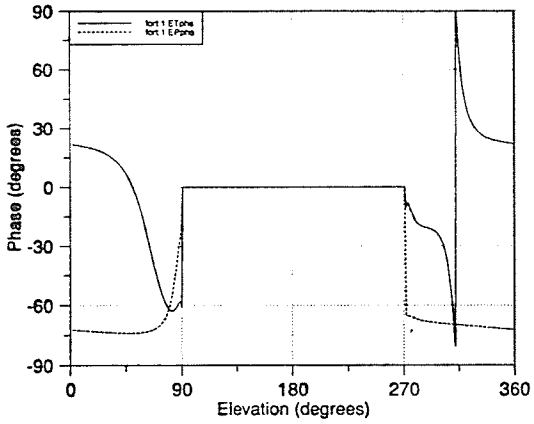

i) Magnitude ii) Phase

a) $\phi=0^o$

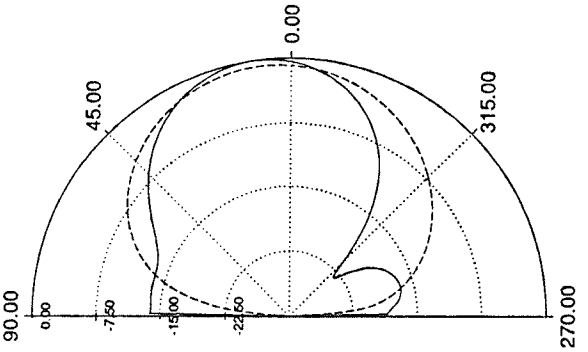

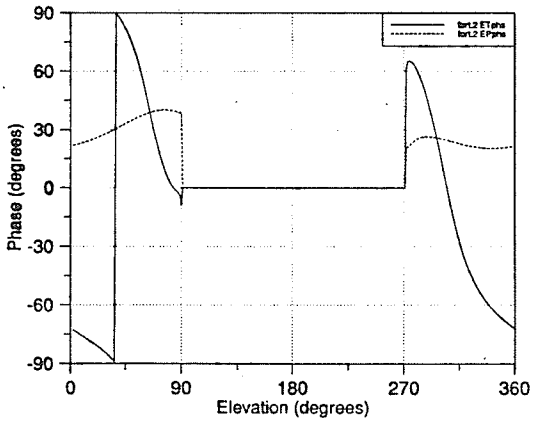

i) Magnitude ii) Phase

b) $\phi=90^o$

Figure 4.5 : Calculated centre frequency of active antenna , f=3.1 GHz,—— E_θ,- - -E_ϕ.

It was thought that the beam squint could be compensated for if the phase along the structure could be controlled. With the modelling software, the phase may be varied readily , so beam squint correction was investigated. For every 100 MHz deviation from the centre frequency, a corresponding phase shift of approximately 12^{o} is generated. Thus the phase shift may be compensated for by including it in the scattering parameters of the devices during the simulation. The results are given in Figure 4.6. As can be seen, when phase correction is applied, the pattern remains broadside with virtually no squint. Most notable improvements are at frequencies farthest from the centre frequency.

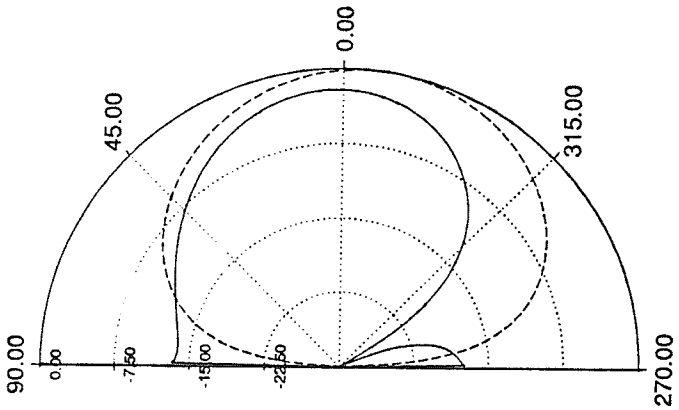

a) f=2.6 GHz, $\Delta\phi$=+60°

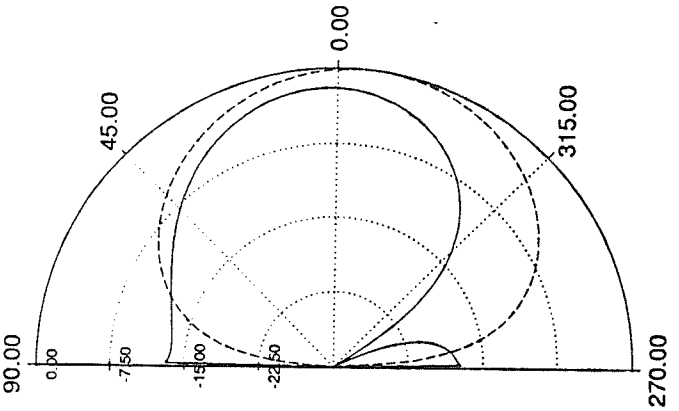

b) f=2.7 GHz, $\Delta\phi$=+48°

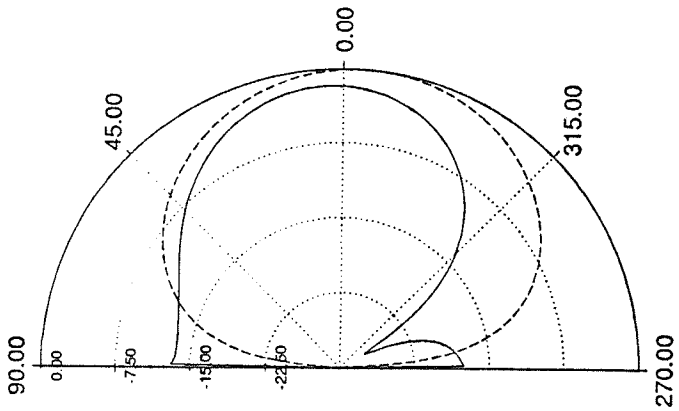

c) f=2.8 GHz, $\Delta\phi$=+36°

Figure 4.6 : Calculated radiation patterns of active antenna with phase correction, amps@0dB, ϕ=0°, —— E_θ, - - - E_ϕ.

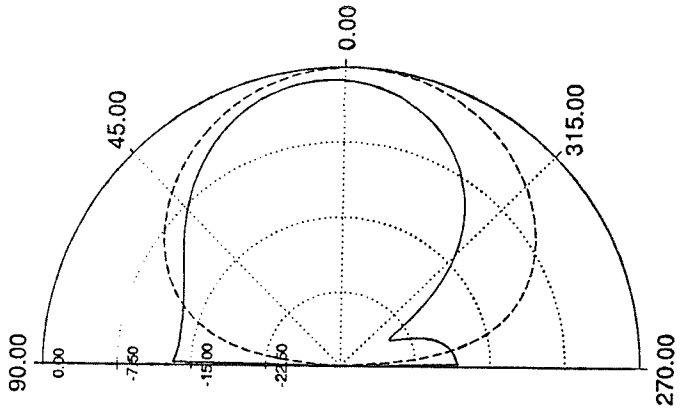

d) f=2.9 GHz , $\Delta\phi$=+24°

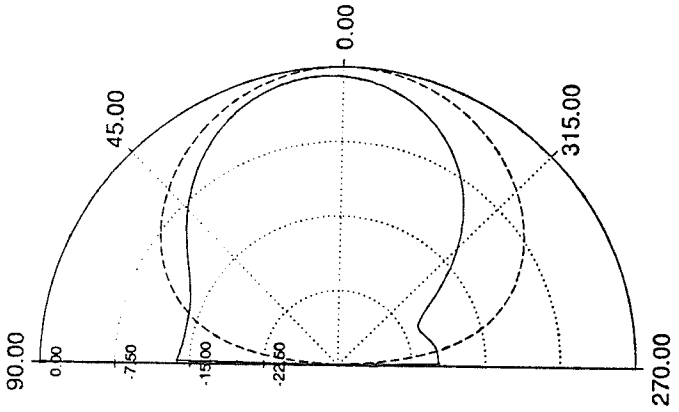

e) f=3.0 GHz , $\Delta\phi$=+12°

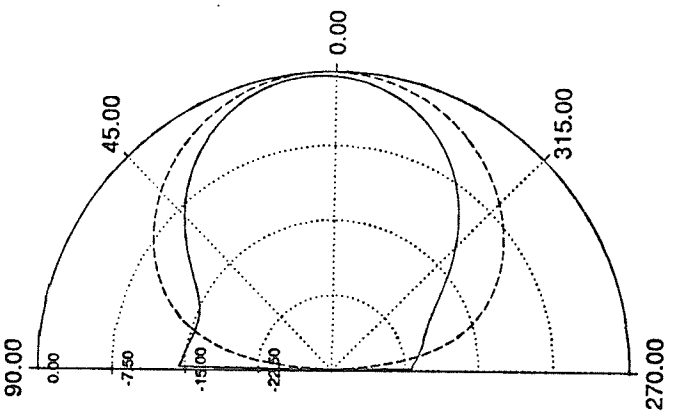

f) f=3.1 GHz , $\Delta\phi$= 0°

Figure 4.6 : (Cont.)

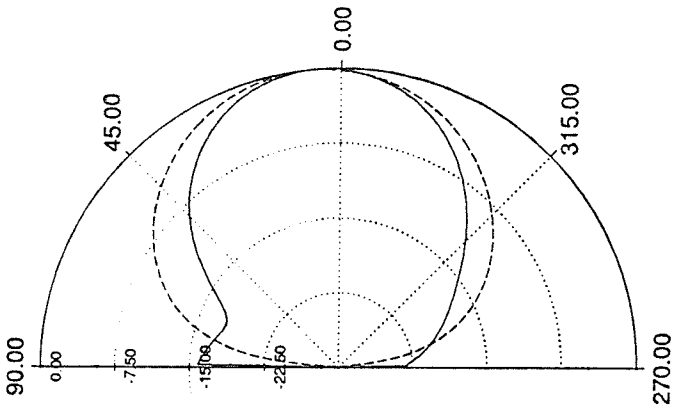

g) f=3.2 GHz , $\Delta\phi$= -12°

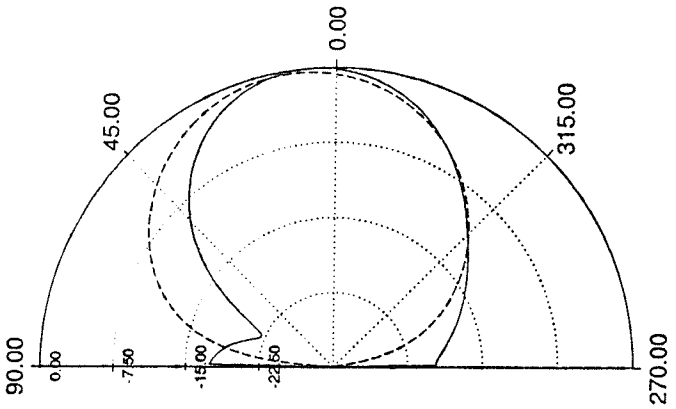

h) f=3.3 GHz , $\Delta\phi$= -24°

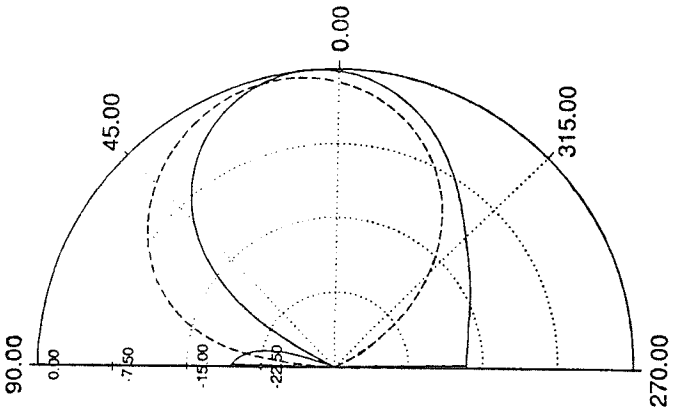

i) f=3.4 GHz , $\Delta\phi$= -36°

Figure 4.6 : (Cont.)

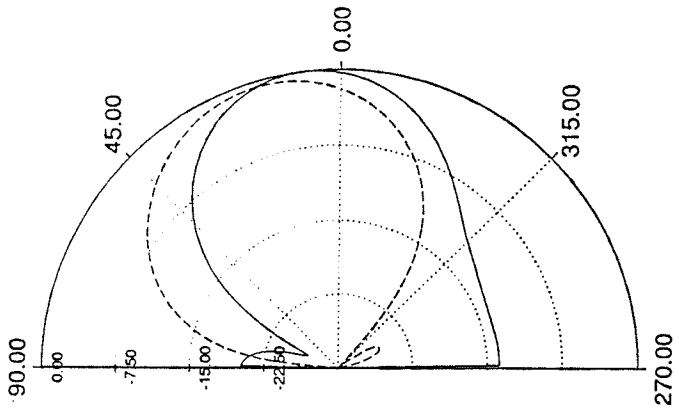

j) f=3.5 GHz, $\Delta\phi$= -48°

Figure 4.6 : (Cont.)

The active antenna was modelled further using this methodology. The scattering parameters of the amplifiers within the EMsim^{TM} simulation were altered to reflect various bias conditions which in turn vary amplifier gain. Gain of the amplifiers was varied from 0dB to 7dB. The calculated patterns are presented in Figure 4.7. As can be seen, the calculated results show an increase in peak gain as amplifier gain increases, while still maintaining a circularly polarized broadside pattern (axial ratio < 3 dB).

The modelling technique was also used to investigate severe amplitude variations along the antenna structure. In the four arm active antenna, as one arm becomes dominant the beamwidth broadens and the quality of the pattern degrades. Circular polarization is maintained because each arm inherently generates a circularly polarized field. The amplitude variations would have a greater affect on the radiated pattern of a structure which does not have four arms. Under these conditions each arm inherently generates an elliptically polarized field.

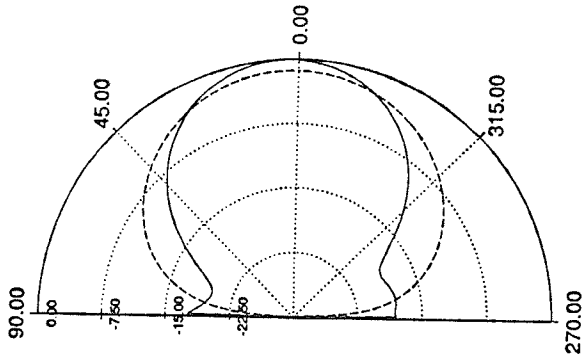

i) $\phi=0^o$

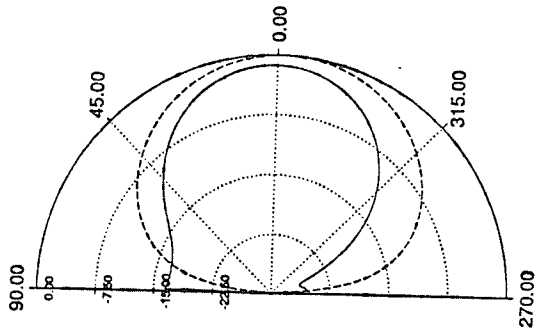

ii) $\phi=90^o$

a) amps @ 0 dB, G_p=-3.63 dB

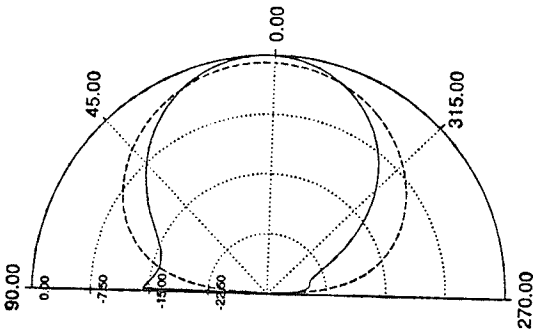

i) $\phi=0^o$

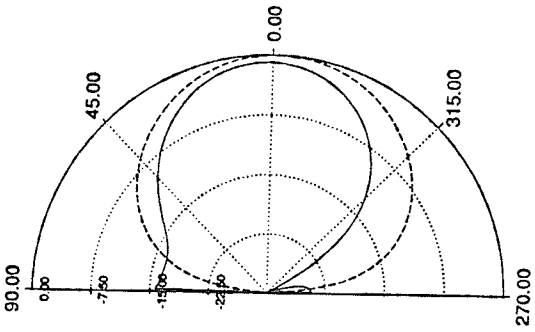

ii) $\phi=90^o$

b) amps @ 2 dB, G_p=-0.89 dB

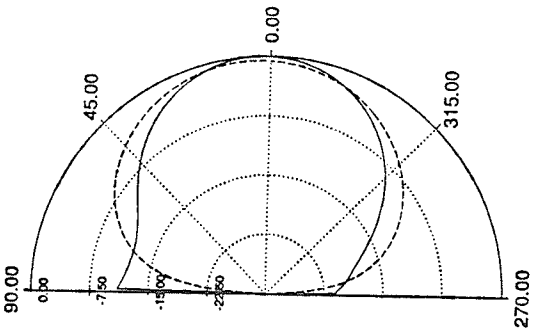

i) $\phi=0^o$

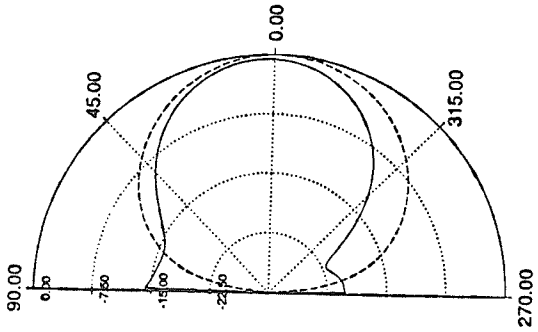

ii) $\phi=90^o$

c) amps @ 4dB, G_p= 2.44 dB

Figure 4.7 : Calculated radiation patterns as amplifier gain varies,—— E_θ,- - -E_ϕ.

4.3 Fabrication of the Active Integrated Antenna

The active integrated antenna modelled in section 4.2 was fabricated. The fabricated antenna has four arms, three MMIC amplifiers and a matched load (ε_r=2.94, h=0.06", f_c=3.0 GHz) (Fig. 4.9). The microstrip lines used for the antenna have a characteristic impedance of 50 ohms. A hybrid approach was taken where the antenna and amplifiers were fabricated separately and then integrated in the final assembly stage. Three GaAs MMIC amplifiers were used as the active devices (Appendix IV). Each amplifier has an operating range of 2 to 6 GHz with a maximum gain of 10 dB. The amplifiers were packaged in order to provide protection during testing. Each amplifier was epoxied to the package along with the appropriate capacitors to provide d.c. bias blockage. All connections were made with wire bonds (Appendix IV). A network analyser was used to measure the scattering parameters of each amplifier at the operating frequency of the antenna. Each amplifier was found to have a 145^o phase shift at f_c = 3.0 GHz when biased for 0 dB gain (Figure 4.8). Thus each phase delay section required line lengths, ϕ_l, of 107.5^o ($\phi_l = (360^o - \phi_{AMP})/2$). Characteristics of each amplifier were recorded under various bias conditions which produced gains of up to 7 dB.

The packaged amplifiers were then integrated with the antenna as shown in Figure 4.9. The bias voltages for the amplifiers were supplied by lines through the ground plane. The antenna configuration in Figure 4.9 was designed to meet the characteristics of the amplifiers and the geometry of the packages available in the lab and it is not necessarily the optimal design.

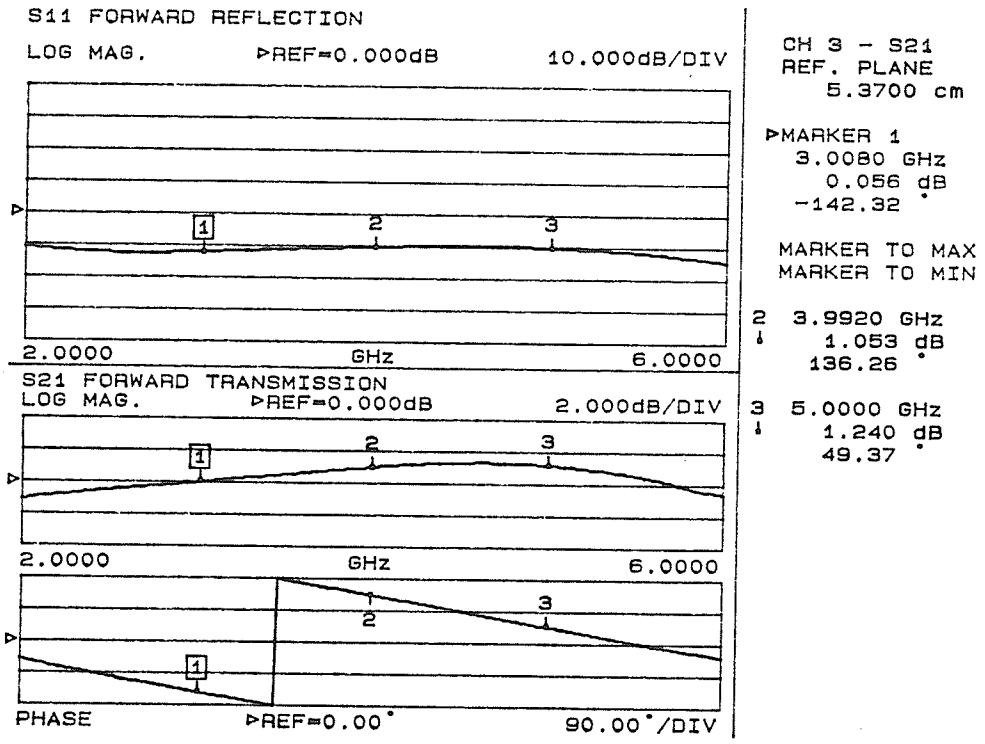

Figure 4.8 : Measured scattering parameters of MMIC amplifier.

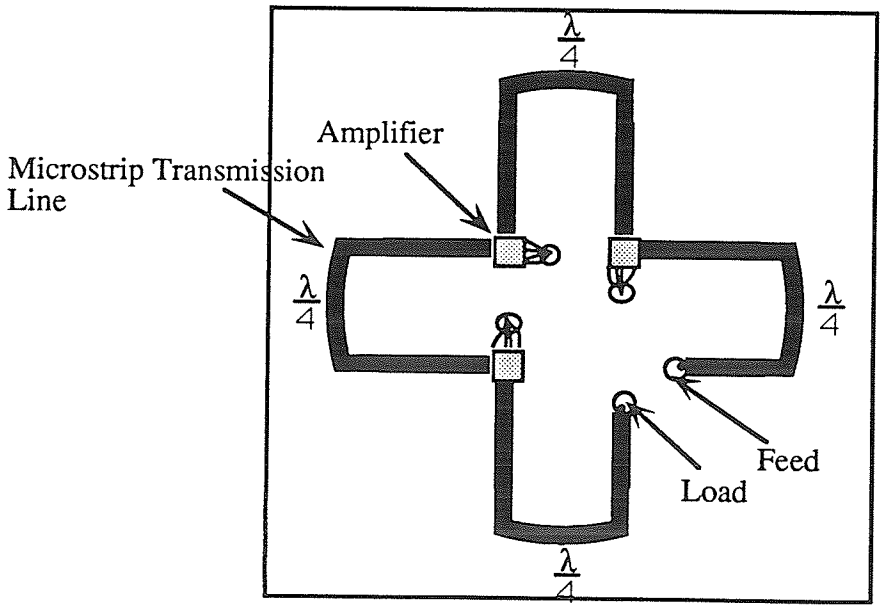

Figure 4.9 : Fabricated active integrated antenna.

4.4 Experimental Results

A network analyser was used to determine the return loss of the integrated antenna under various bias conditions (Figure 4.10). The input impedance bandwidth based on a VSWR of 2:1 was found to be very broad, approximately 60 %. This is to be expected, as the input impedance is primarily dependent upon the characteristic impedance of the microstrip line and the input match of the amplifier. The amplifiers used in this antenna are limited to a match of -13 dB. The input impedance bandwidth of the antenna remained relatively constant as the amplifiers were biased to operate at various gain conditions.

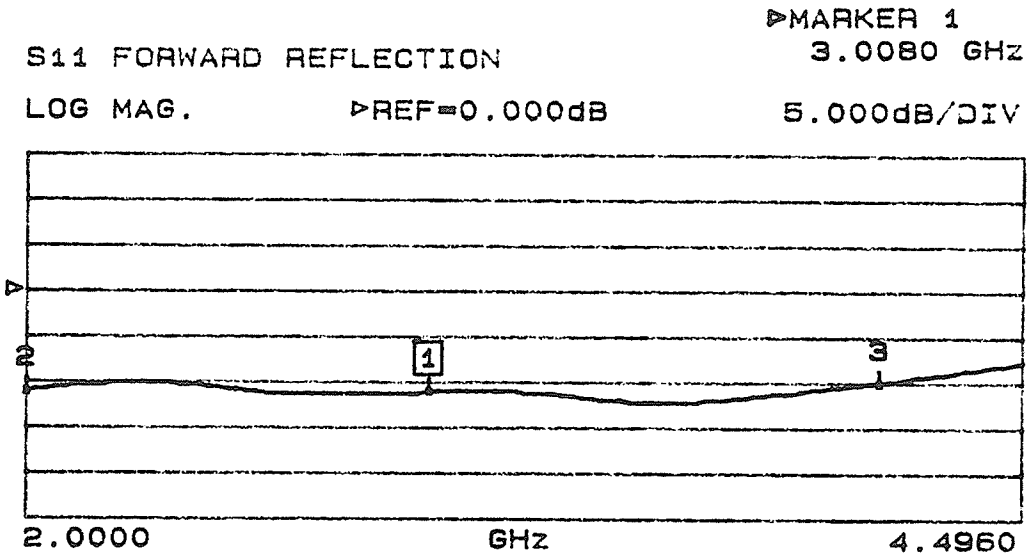

Figure 4.10 : Return loss measurement of active antenna, amps @ 0dB.

Pattern measurements over this frequency range show that a pattern bandwidth of approximately 10 % is obtained. Within this bandwidth, the patterns are broadside and circularly polarized with an axial ratio less than 3 dB within the 3 dB beamwidth. As anticipated from the numerical results of the passive antenna [77], the measured patterns of the active antenna show the main beam to squint as the frequency deviates from the centre frequency. The measured radiation patterns are shown in Figure 4.11 where the

centre frequency, f_c=3.05 GHz, is shown in Figure 4.11d). Elevation patterns were measured through various planes of the antenna dictated by ϕ. The E-plane corresponds to $\phi=0^o$. Patterns at $\phi=0^o$ and 90^o were observed to be similar. To ascertain that acceptable circular polarization is present, measurements were taken at $\phi=45^o$ (Figure 4.11e)). As can be seen, this antenna may be considered to be circularly polarized. It was experimentally determined that the packages had an adverse effect on the radiation patterns. By placing small amounts of ECCOSORB MF-117 (6mm x 4mm x 1mm) on top of the packages, the effects of the packages were reduced which results in the improvement of the pattern characteristics, particularly the axial ratio (Figure 4.12a), compare with Figure 4.11 d)). Under these conditions the centre frequency was measured to be 3.1 GHz (Figure 4.12 b)).

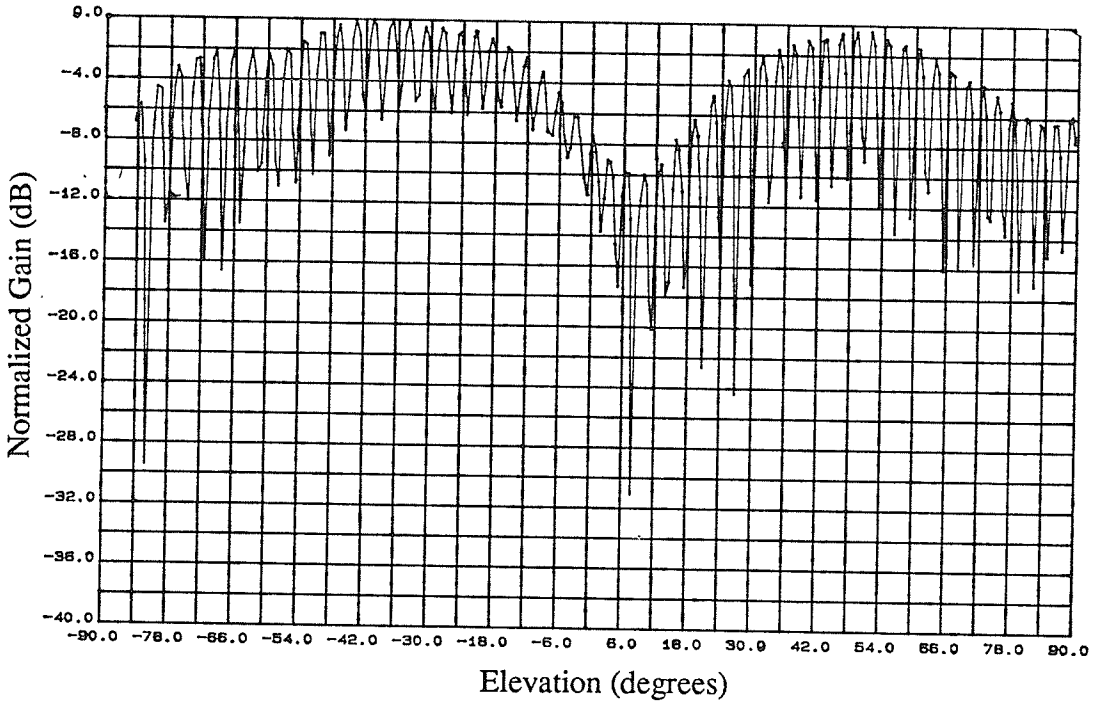

a) f = 2.6 GHz, $\phi=0^o$

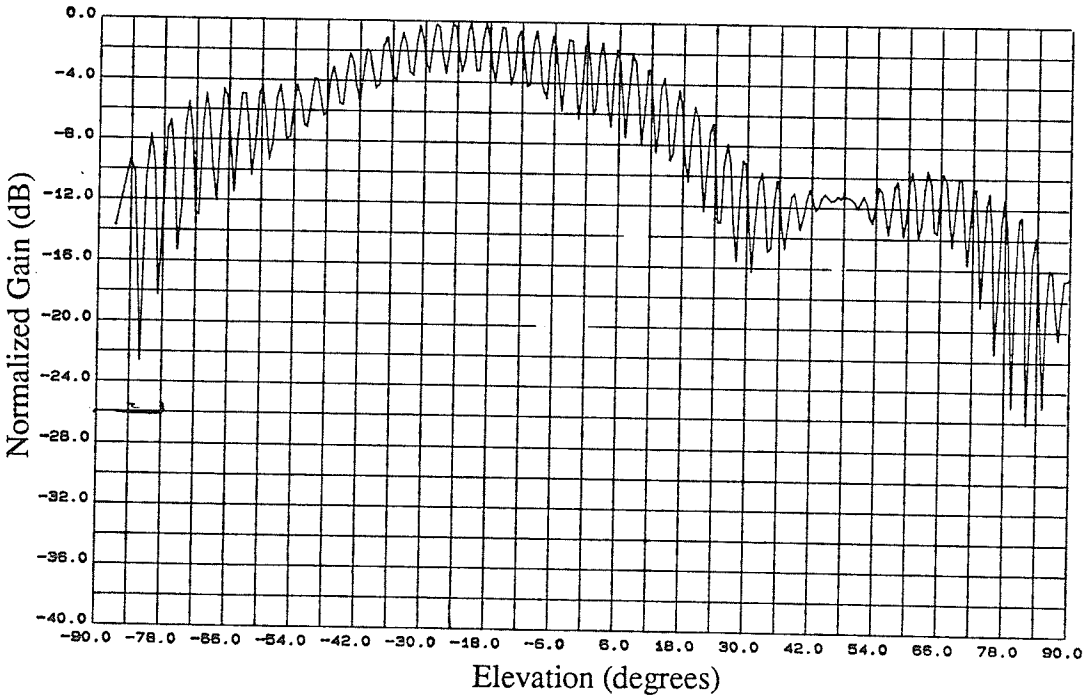

b) f = 2.85 GHz, Gp = -7.1 dB, $\phi=0^o$

Figure 4.11 : Measured patterns of four arm active antenna, amps@0 dB,

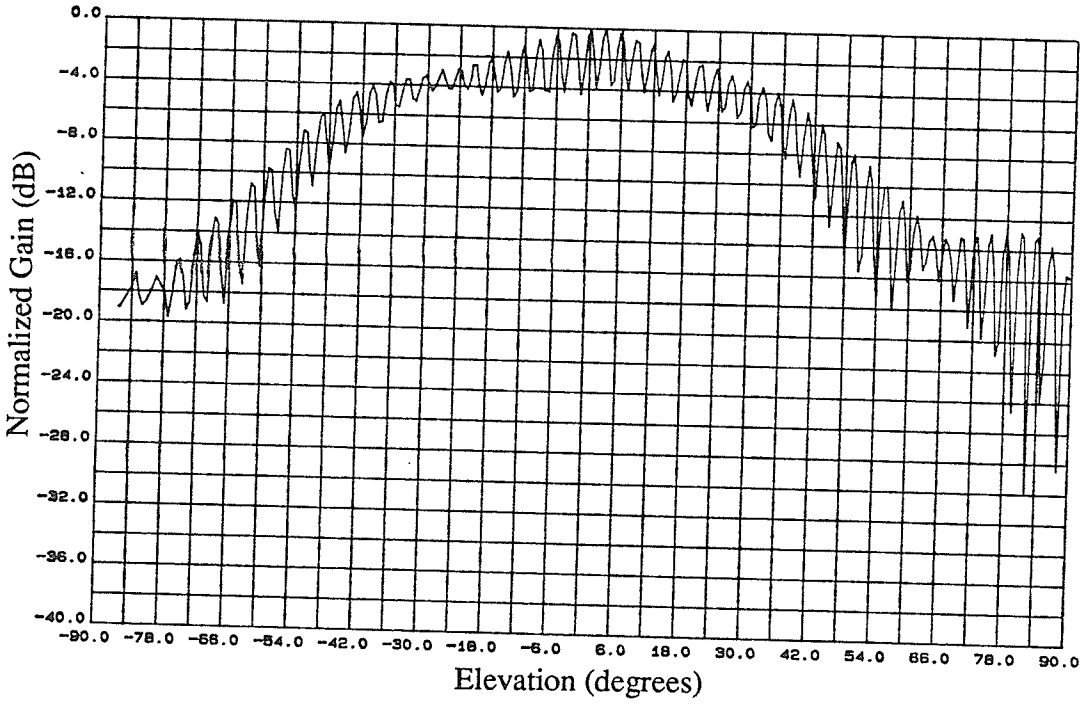

c) f = 3.0 GHz, Gp = -5.1 dB, ϕ=0^o

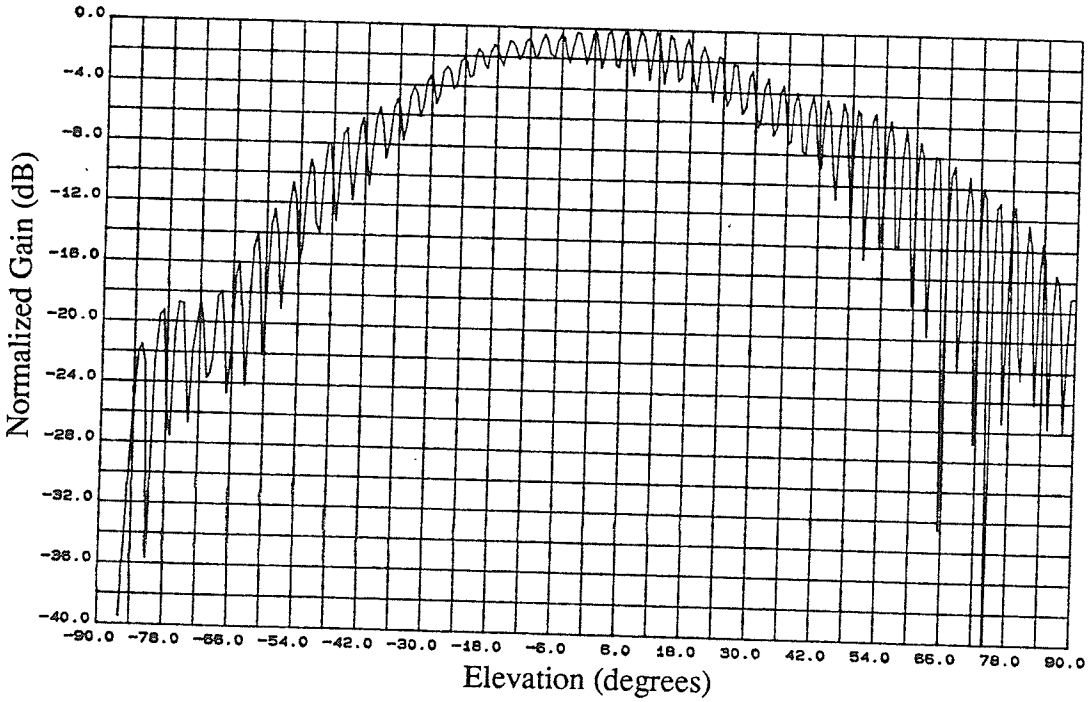

d) f = 3.05 GHz, Gp = -4.4 dB, ϕ=0^o

Figure 4.11 : (cont.)

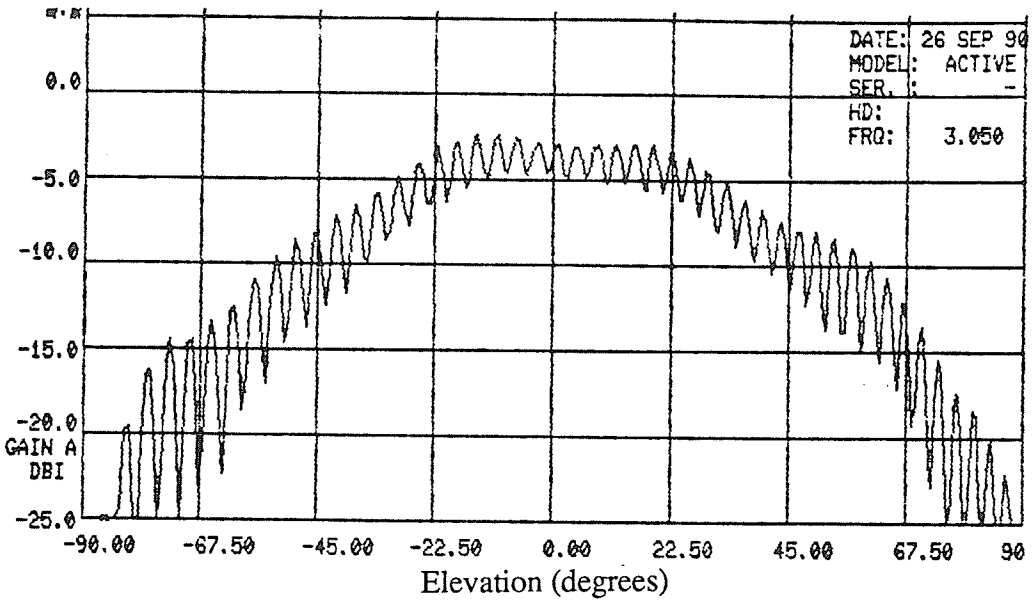

e) f = 3.05 GHz, Gp = -4.4 dB, ϕ=45^o

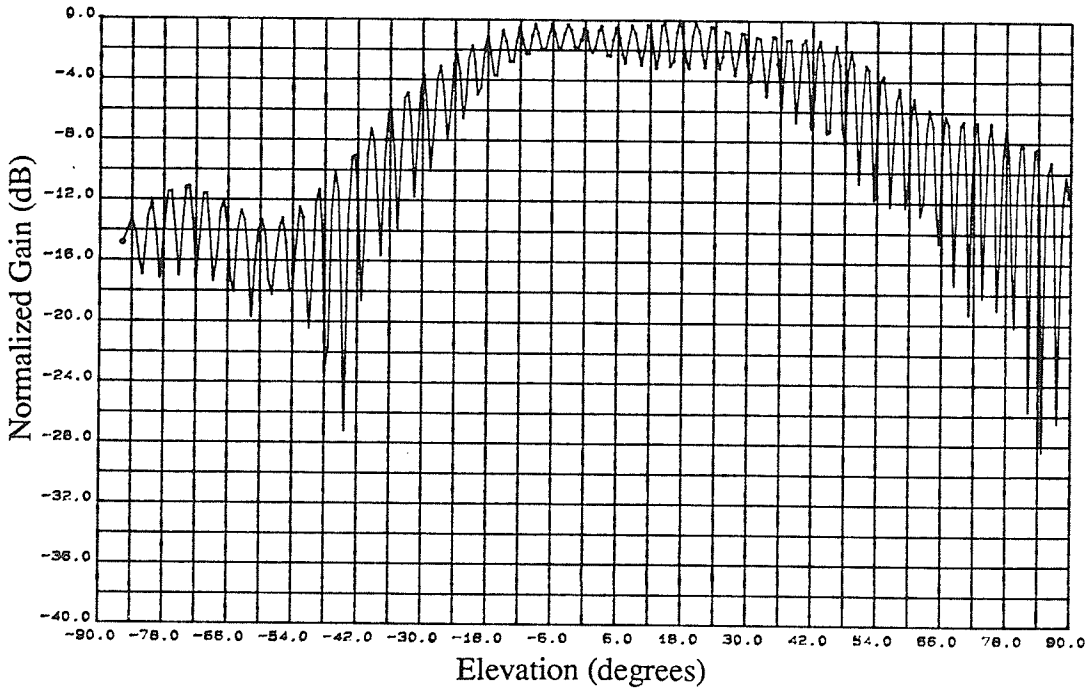

f) f = 3.15 GHz, Gp = -3.2 dB, ϕ=0^o

Figure 4.11 : (cont.)

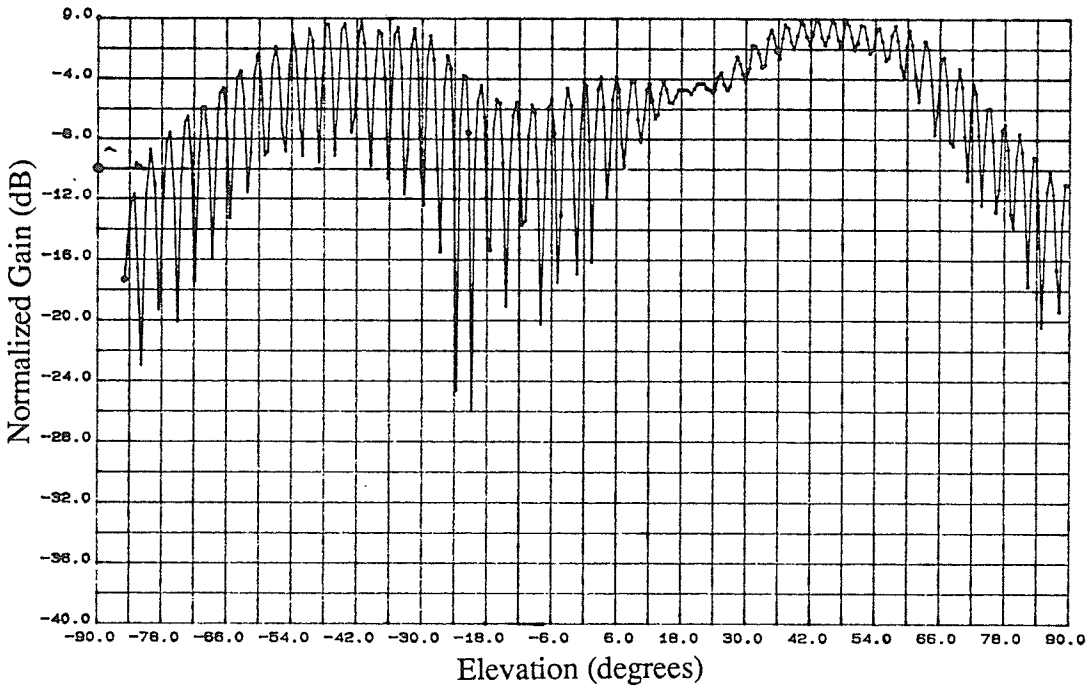

g) f = 3.5 GHz, $\phi=0^{o}$

Figure 4.11 : (cont.)

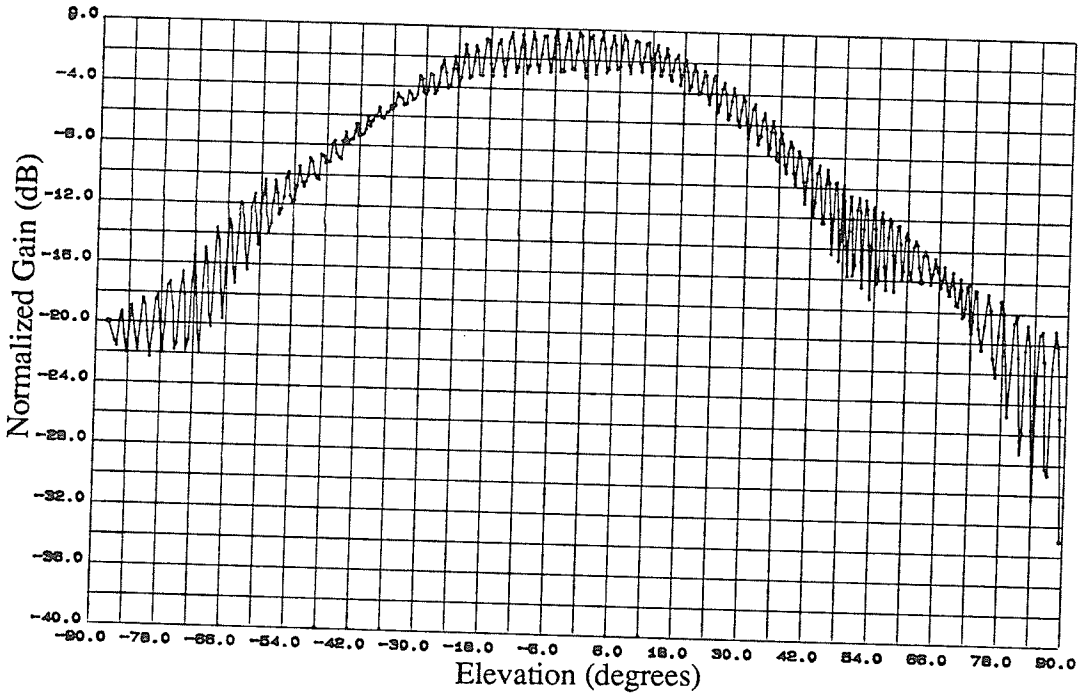

a) f=3.05 GHz

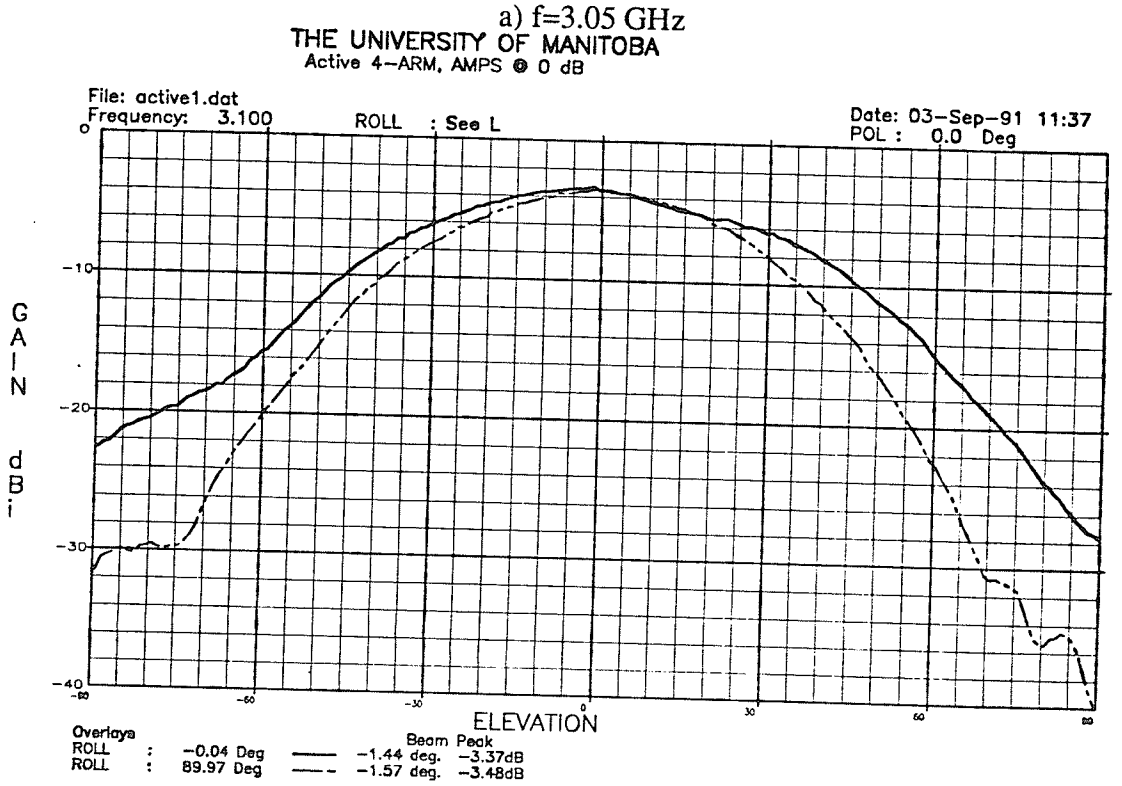

b) f=3.1 GHz

Figure 4.12 : Measured radiation pattern with package absorber, amps@0 dB, $\phi=0^{o}$, —— E_{θ}, - - - E_{ϕ}.

Several bias voltages were applied to the amplifiers to produce individual gains ranging from 0 to 7 dB. Pattern measurements were recorded with the amplifiers biased to produce equivalent gain levels. Figure 4.13a) and b) show plots of the axial ratio and peak gain of the main beam over the pattern bandwidth. As can be seen, the gain of the antenna increases as amplifier gain increases while still maintaining an axial ratio less than 3 dB.These results were predicted by the modelling procedure. The measured patterns of the antenna under the various bias conditions can be found in Figure 4.14. The radiation characteristics of the antenna were similar for various bias conditions and correspond with the modelled results, i.e. beam squint off centre frequency and eventual formation of centre null. This can be seen in the frequency sweep with the amplifiers biased for 7dB (Figure 4.14 c)-i) as compared with Figure 4.11).

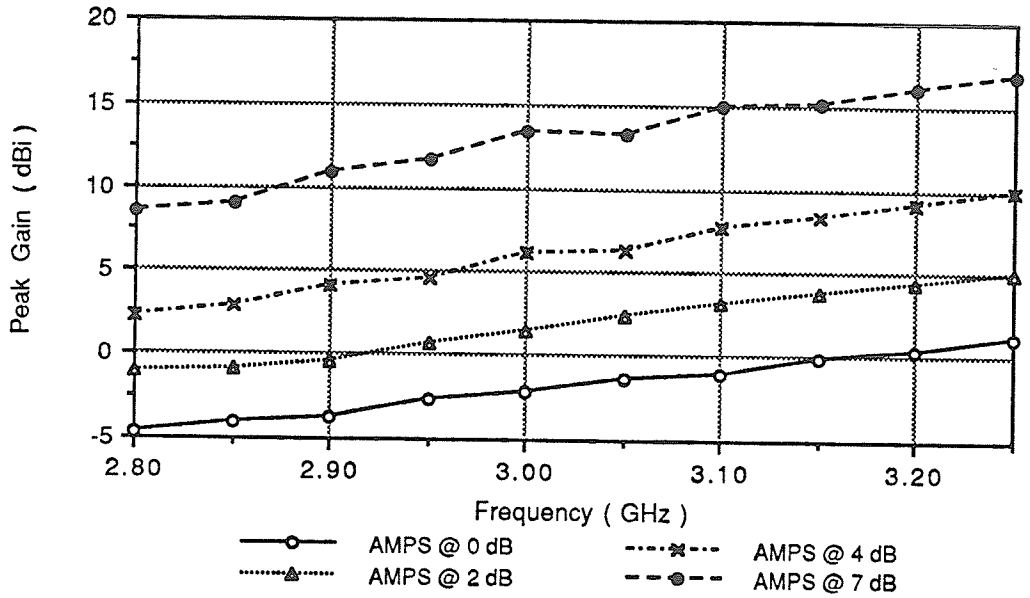

a) Peak gain

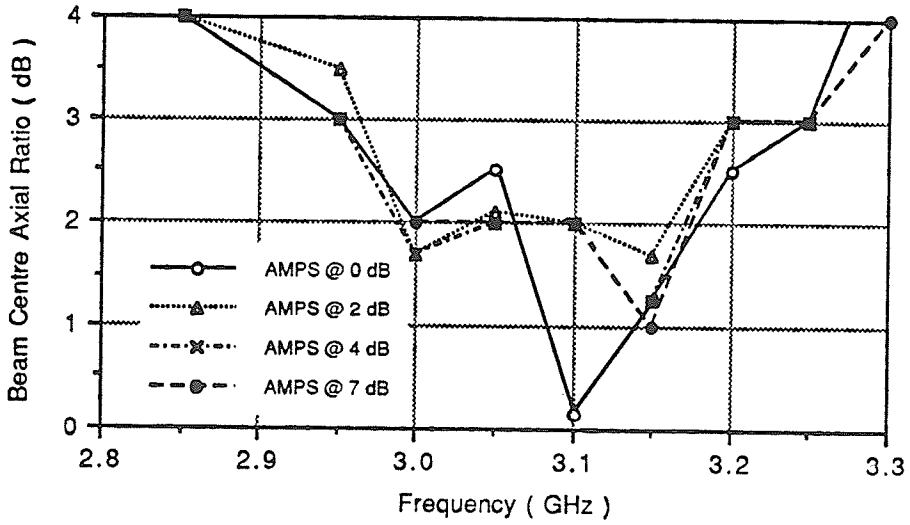

b) Axial ratio

Figure 4.13 : Measured axial ratio and peak gain of active antenna as a function of amplifier gain.

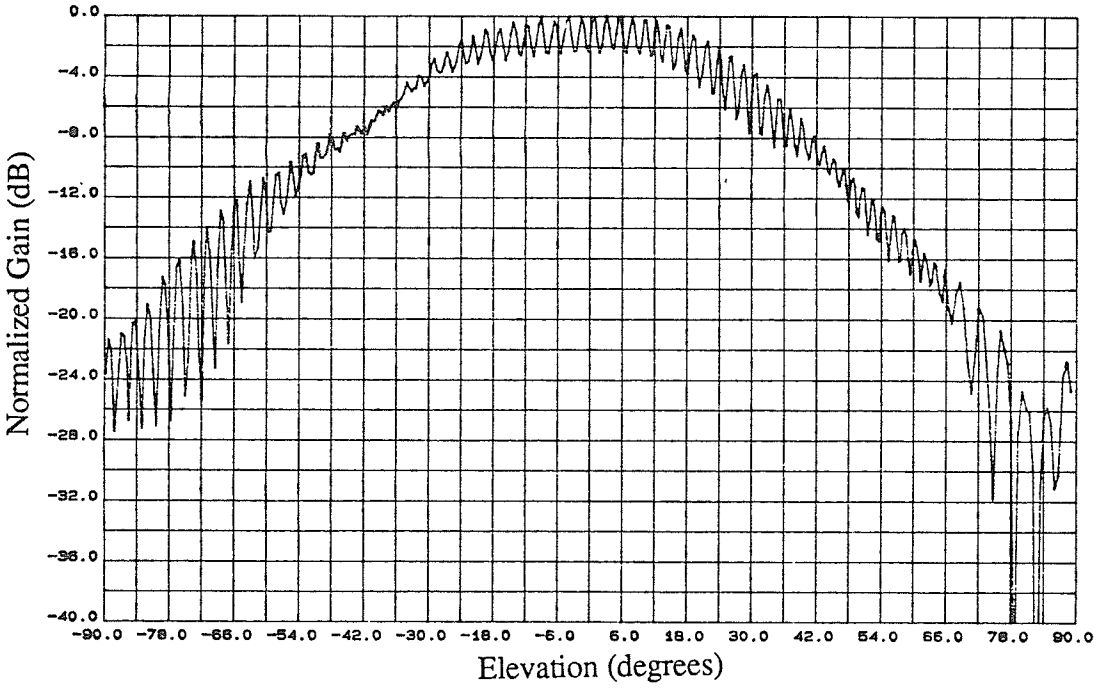

a) amps@ 2dB, f=3.05 GHz, Gp = -0.6 dB, $\phi=0^o$

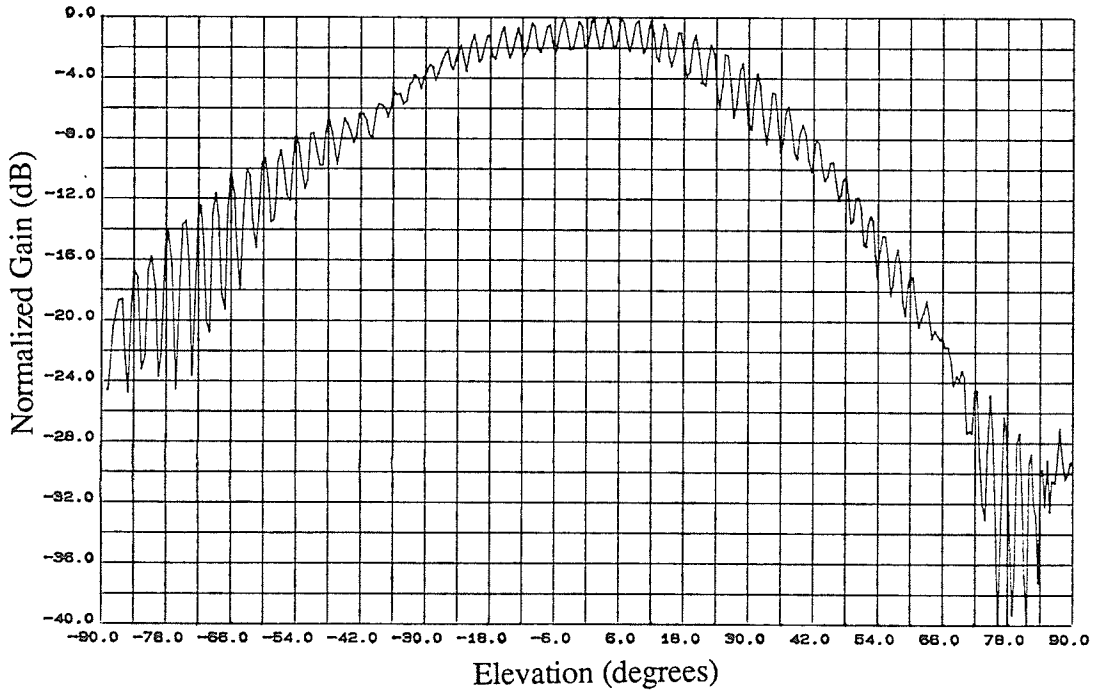

b) amps@ 4dB, f=3.05 GHz, Gp = 3.3 dB, $\phi=0^o$

Figure 4.14 : Measured radiation patterns of active antenna under various bias conditions.

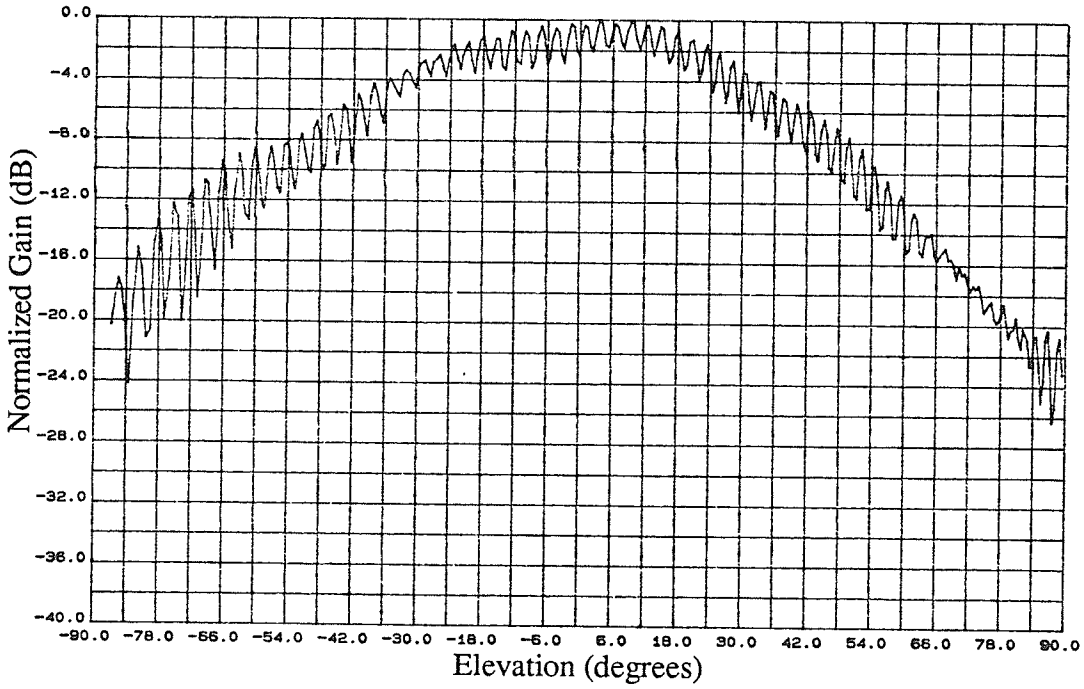

c) amps@ 7dB, f=3.05 GHz, Gp = 10.3 dB, $\phi=0^o$

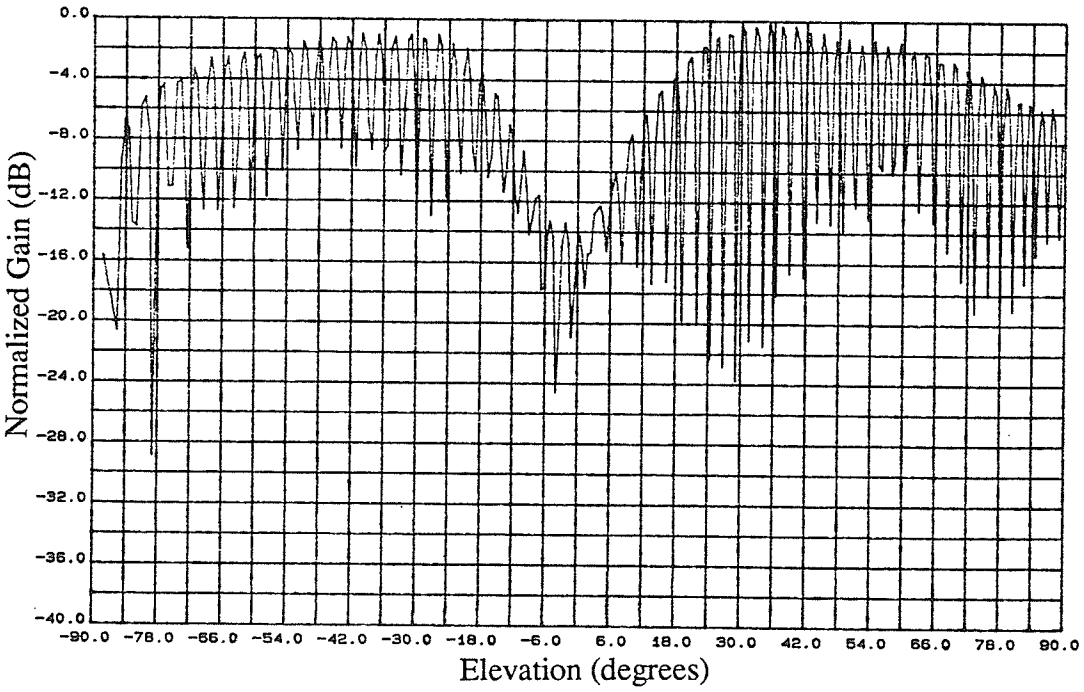

d) amps@ 7dB, f=2.6 GHz, $\phi=0^o$

Figure 4.14 : (cont.)

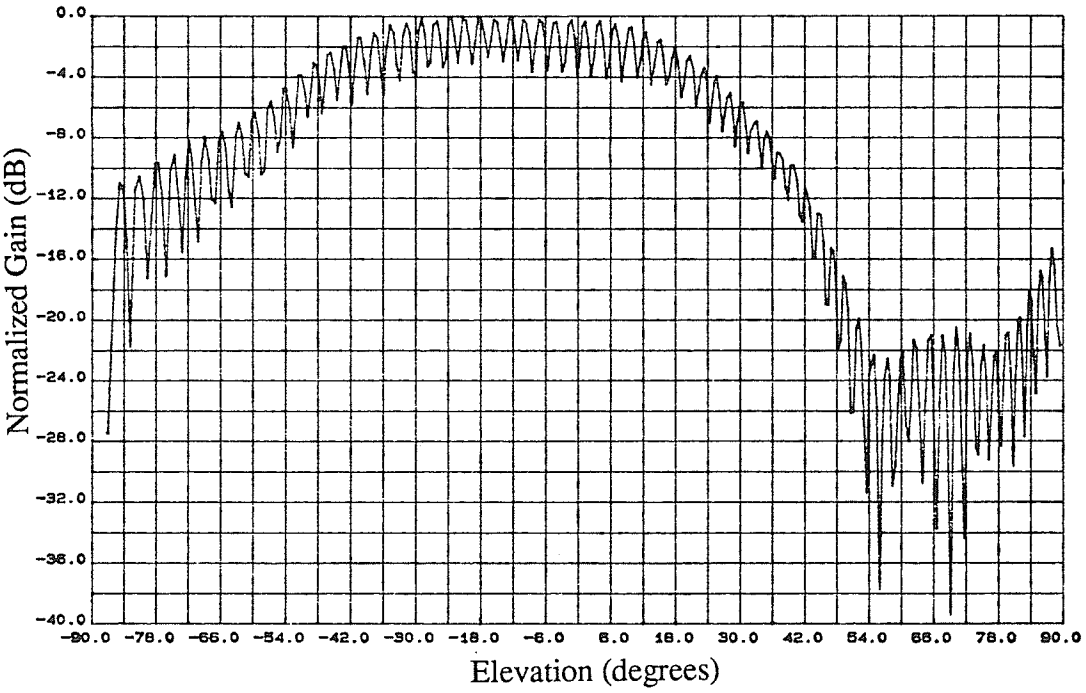

e) amps@ 7dB, f=2.95 GHz, Gp = 8.6 dB, $\phi=0^o$

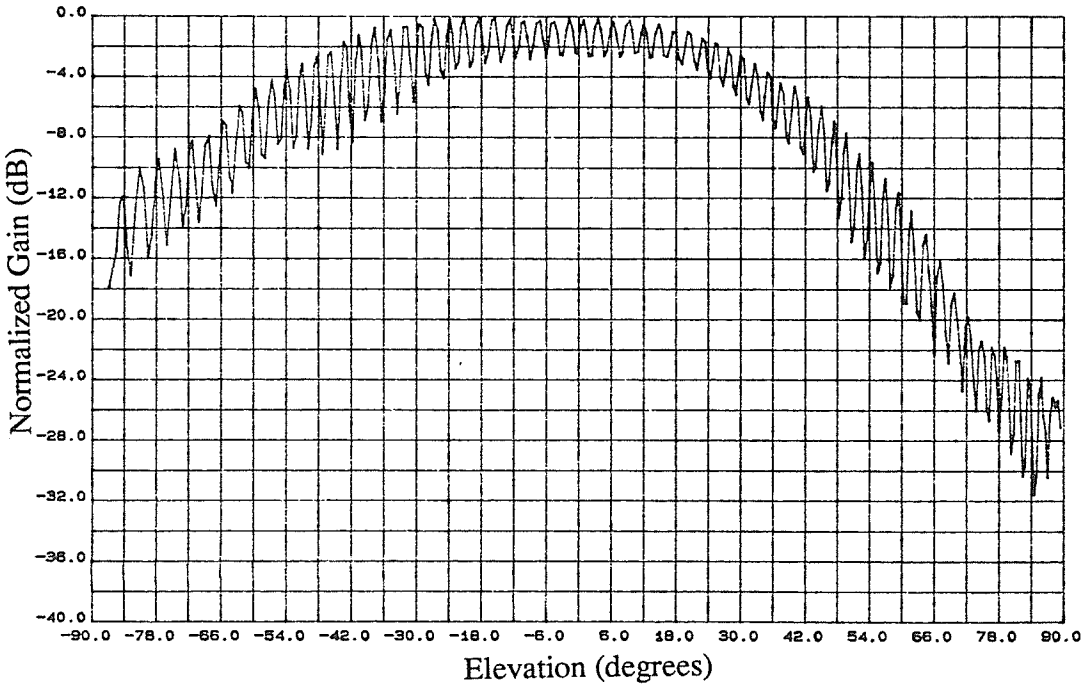

f) amps@ 7dB, f=3.0 GHz, Gp = 10.4 dB, $\phi=0^o$

Figure 4.14 : (cont.)

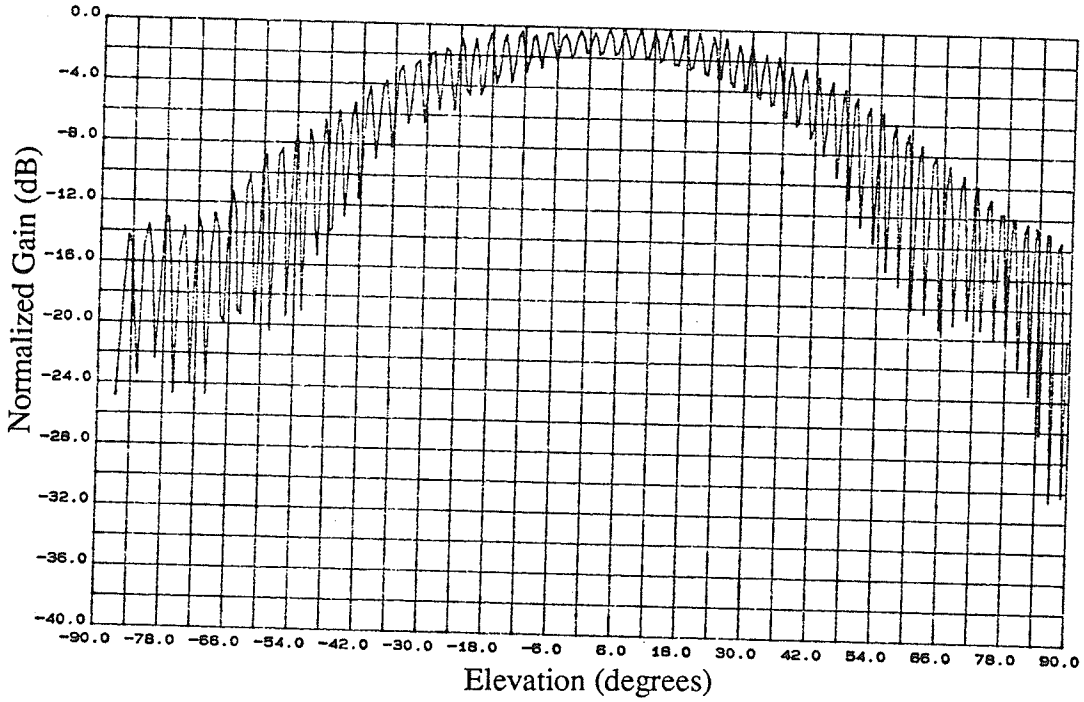

g) amps@ 7dB, f=3.1 GHz, Gp = 11.9 dB, $\phi=0^o$

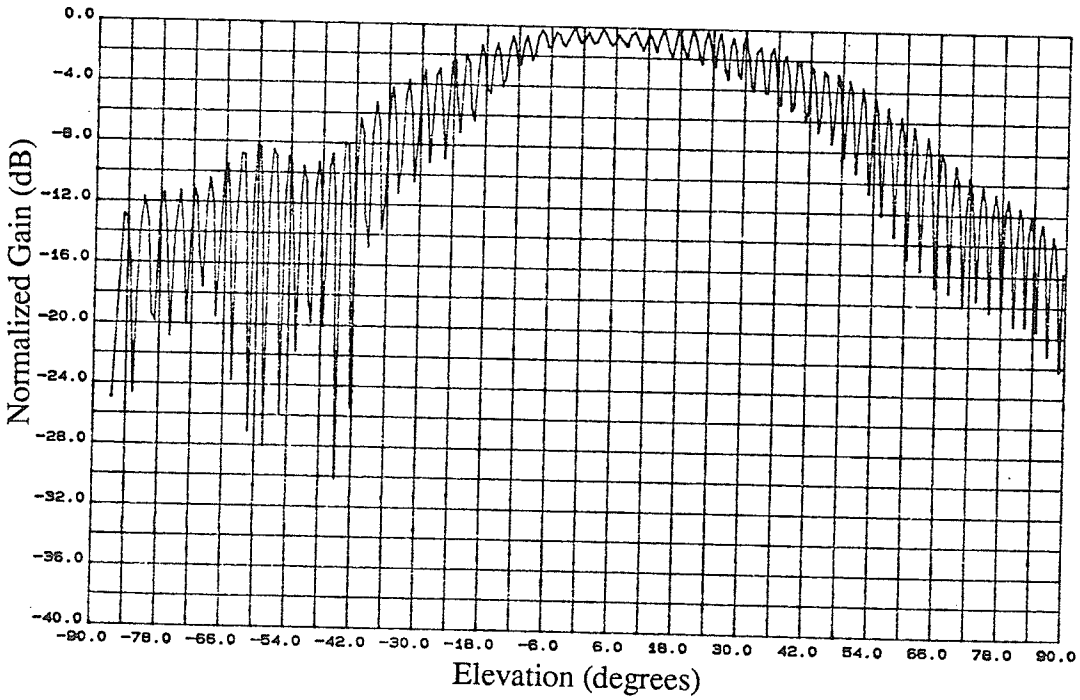

h) amps@ 7dB, f=3.15 GHz, Gp = 12.1 dB, $\phi=0^o$

Figure 4.14 : (cont.)

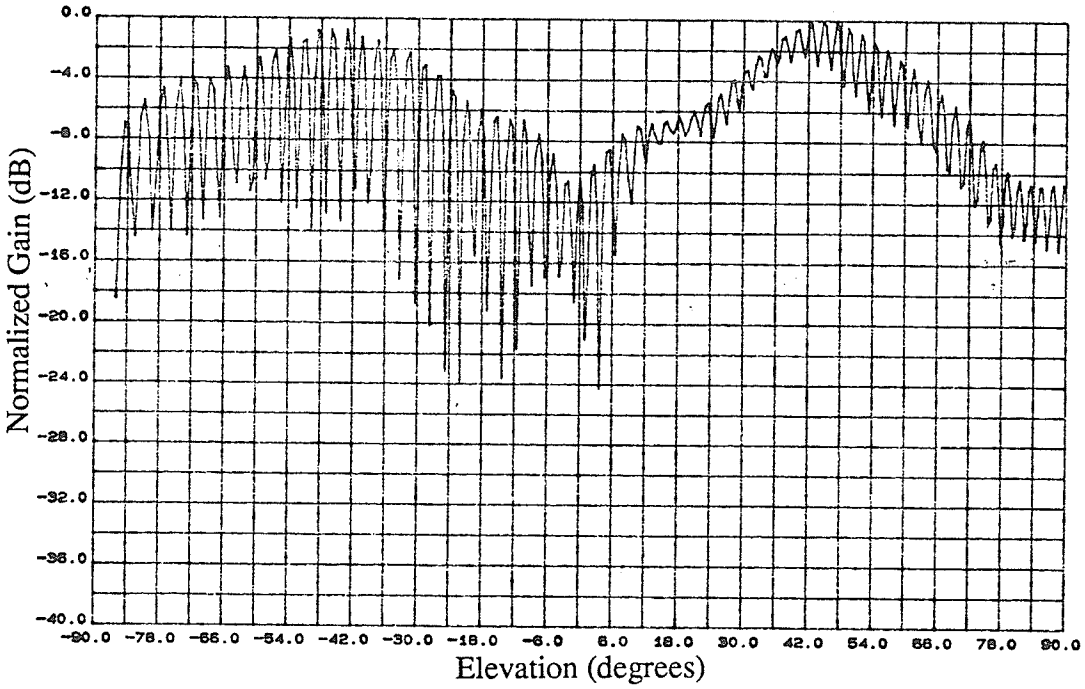

i) amps@ 7dB, f=3.5 GHz,, $\phi=0^o$

Figure 4.14 : (cont.)

4.5 Accuracy of Design Methodology

In this section, a comparison is made between the predicted and measured results of the designed active antenna. The predicted radiation characteristics are presented in section 4.2 while the experimental measurements are presented in section 4.4.

With respect to the modelling approach, some limitations have been outlined in section 3.2, such as the 1λ size restriction to account accurately for coupling. As EMsim^{TM} is based upon the moment method to calculate the current distribution, the structure must be discretized. The discretization of the microstrip transmission line is a parameter which affects the accuracy of the design methodology. This aspect was investigated first. The antenna structure was divided into various segment sizes and the resulting modelled field components were compared with the measured results.

The structure being simulated is identical to the one which was fabricated. The microstrip transmission line of the active antenna was divided into segments according to l=λ/16, λ/24, λ/36 and λ/60. In addition, the case where straight line pieces are divided into λ/16 segments and corners divided into λ/32 segments was studied. Both versions of EMsim^{TM}, 3.0 and 3.5, were evaluated. Initially, f=3.0 GHz was the intended design frequency. Thus a comparison between modelled and experimental measurements was carried out at this frequency. As a function of segment length, the calculated field components are tabulated and plotted with the measured results in Table 4.1 and Figure 4.15. These results are for the case when the amplifiers are biased for 0dB gain. The measured field components are E_θ=-5.67 dBV/m and E_ϕ=-3.67 dBV/m. The radiation patterns in two orthogonal planes were also calculated and are presented in Figure 4.16a). With respect to the two orthogonal planes, the worst case axial ratio is plotted in Figure 4.16b). Based upon Figures 4.15 and 4.16, one can conclude that the optimal segmentation length is λ/36. As can be seen, the calculated results deviate from the

measured when the segmentation length is reduced to λ/60. Under these conditions a very large matrix is generated because of the number of segments. Thus, it is conceivable that numerical errors occur depending on how the large matrix is treated. In addition, the manner in which the singularity is treated makes it sensitive to the segmentation length.

	SEGMENTATION				
	λ/16	λ/16, λ/32	λ/24	λ/36	λ/60
Gain,E_θ(dBV/m)	-5.33	-6.03	-4.83	-4.91	-5.06
Gain,E_ϕ(dBV/m)	-3.62	-3.32	-3.26	-3.63	-3.0

a) : Calculated gain of active antenna, wm350.

	SEGMENTAION				
	λ/16	λ/16, λ/32	λ/24	λ/36	λ/60
Gain,E_θ(dBV/m)	-5.06	-5.74	-4.67	-7.32	-5.71
Gain,E_ϕ(dBV/m)	-3.12	-3.94	-2.84	-5.64	-4.18

b) : Calculated gain of active antenna, wm300.

Table 4.1 : Calculated gain of active antenna, f=3.0 GHz, amps@0dB.

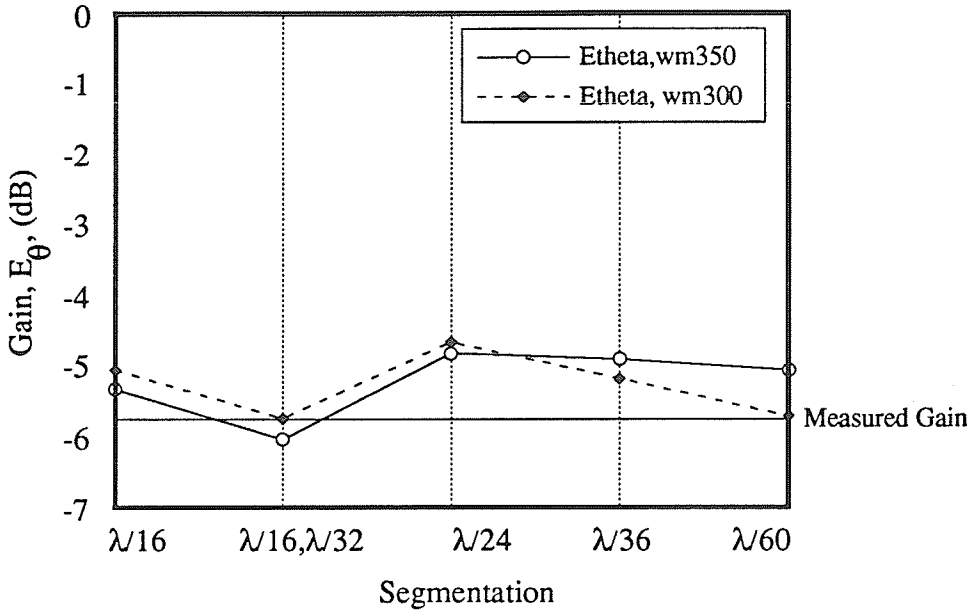

a) E_θ field component

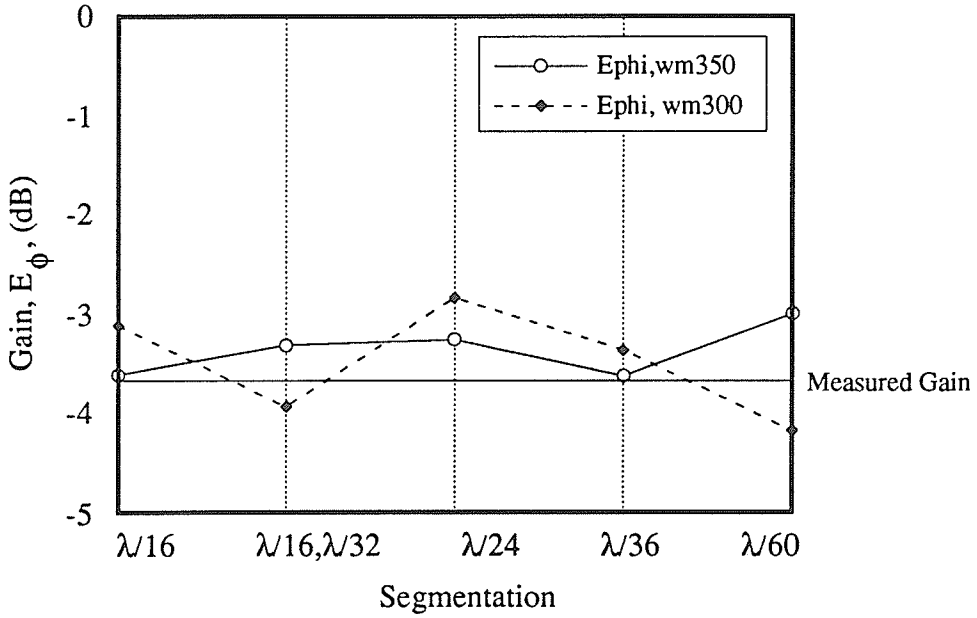

b) E_ϕ field component

Figure 4.15 : Calculated gain (as a function of antenna segmentation) compared to measured gain, E_ϕ.

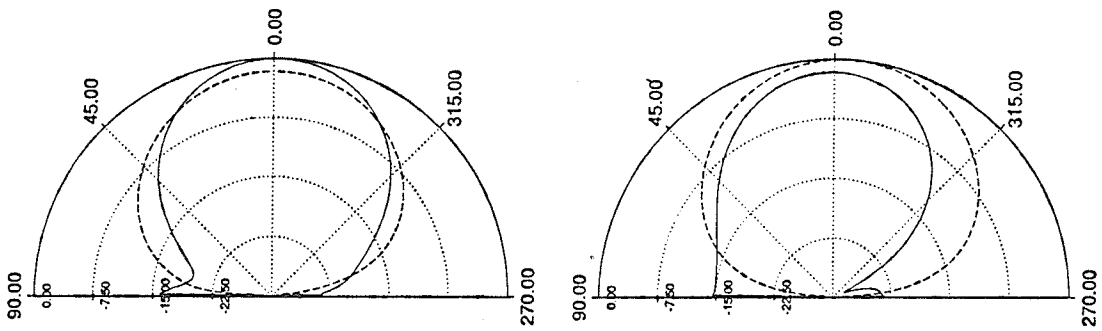

i) $\phi=0^o$ ii) $\phi=90^o$

a) $l=\lambda/16$

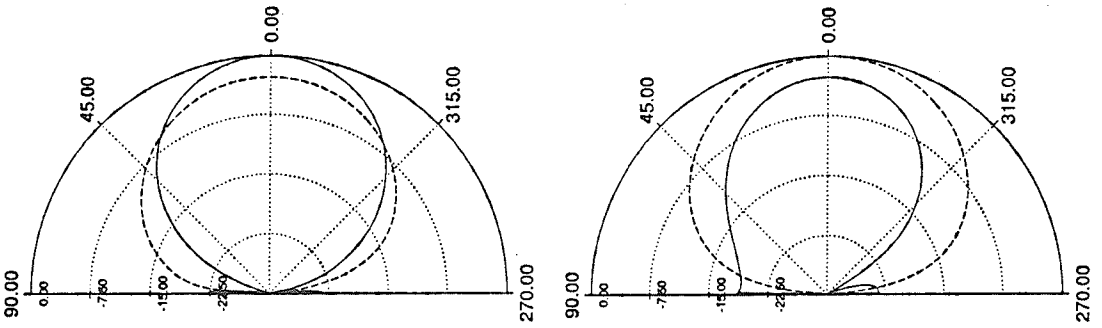

i) $\phi=0^o$ ii) $\phi=90^o$

b) $l=\lambda/16$, $\lambda/32$ corners

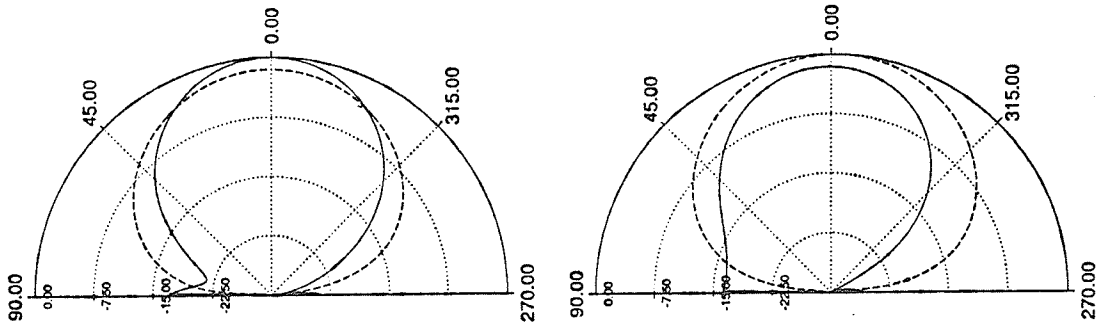

i) $\phi=0^o$ ii) $\phi=90^o$

c) $l=\lambda/24$

Figure 4.16 a) : Calculated radiation patterns as a function of antenna segmentation., —— E_θ, - - - E_ϕ.

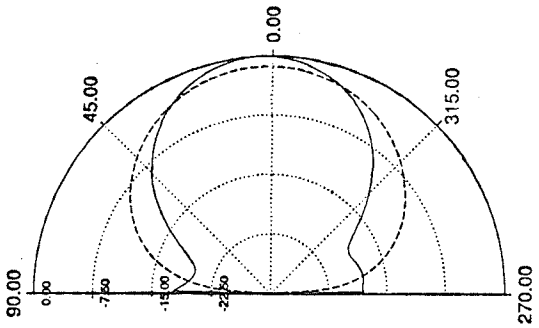

i) $\phi=0^o$

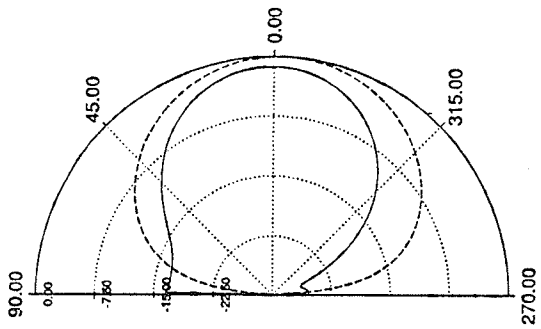

ii) $\phi=90^o$

d) $l=\lambda/36$

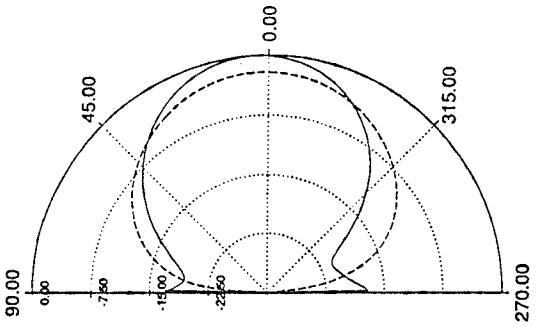

i) $\phi=0^o$

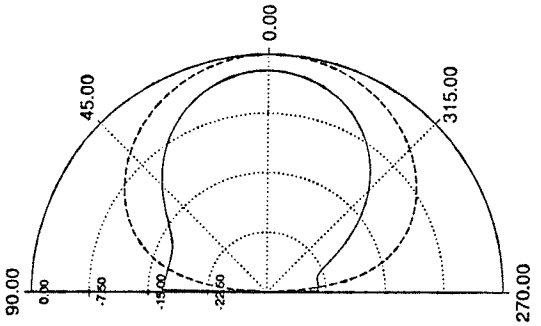

ii) $\phi=90^o$

e) $l=\lambda/60$

Figure 4.16 a): (Cont.)

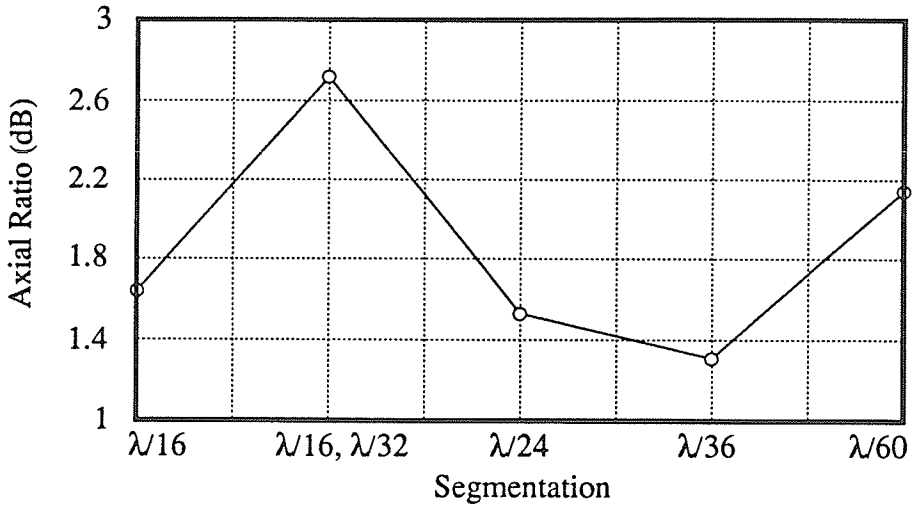

Figure 4.16 b) : Calculated axial ratio as a function of antenna segmentation.

With the optimum segmentation determined to be λ/36, the active antenna was modelled with the results previously presented in section 4.2. Figure 4.7 shows the calculated radiation patterns and the calculated peak gains are summarized in Table 4.2. The calculated gains are plotted with the measured in Figure 4.17. It should be noted that the peak gain values presented here vary slightly from those of Figure 4.13 because the antenna was modified between measurements. An amplifier required replacing, thus slightly altering the available gain for a given bias voltage. The agreement between measured and calculated results is thought to be satisfactory. Although the calculated results deviate from the measured as amplifier gain increases, several factors must be considered. From the measurement perspective, the MMIC amplifiers used generated a substantial amount of heat and the gain/phase were noted to drift with time. Thus it was not possible to accurately set the gain/phase of each amplifier. From the modelling perspective, EMsim^{TM} does not account for the finite ground plane, i.e. an infinite ground plane is assumed. The fabricated antenna has a finite ground plane. Thus any contribution from surface waves and scattering, constructive or destructive, at the substrate edges are not accounted for. In addition, the post-processor calculates fields based upon the spatial wave contribution and contribution from the surface waves is neglected.

Amplifier Gain (dB)	Measured Peak Gain (dB) (f=3.0 GHz)	Calculated Peak Gain (dB) (f=3.0 GHz)
0	E_θ = -5.6 E_ϕ = -3.6	E_θ = -4.92 E_ϕ = -3.63
2	E_θ = -1.9 E_ϕ = 0.1	E_θ = -1.81 E_ϕ = -0.89
4	E_θ = 2.0 E_ϕ = 4.0	E_θ = 1.88 E_ϕ = 2.44
7	E_θ = 9.2 E_ϕ = 11.0	E_θ = 8.11 E_ϕ = 8.08

Table 4.2 :Measured and calculated peak gain of active antenna as a function of amplifier gain.

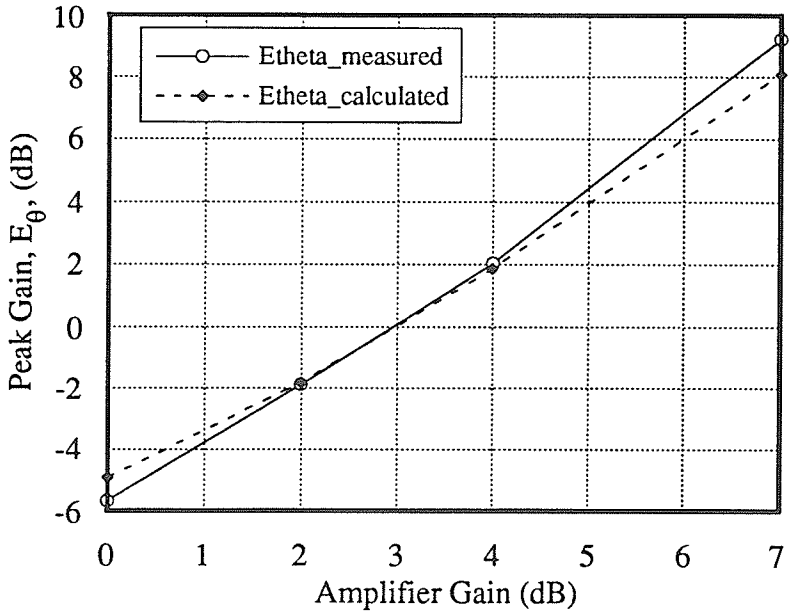

Figure 4.17 a) : Peak gain of active antenna as a function of amplifier gain, f=3.0 GHz, E_θ.

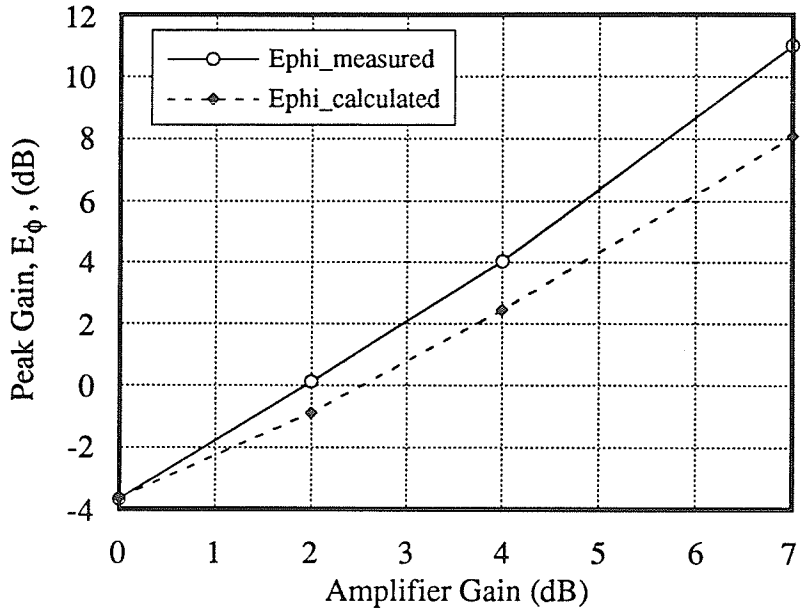

Figure 4.17 b) : Peak gain of active antenna as a function of amplifier gain, f=3.0 GHz, E_ϕ.

Both the modelled and measured results indicate that the centre frequency of the designed active antenna is 3.1 GHz (Figure 4.5 and 4.12 respectively). The predicted and measured patterns are plotted in Figure 4.18. Both field components in the $\phi=0^o$ plane are presented. As can be seen, the calculated and measured field components are in good agreement ($-60^o <$ elevation angle $< 60^o$). At elevation angles between 60^o and 90^o the calculated and measured quantities deviate from one another. This deviation may be attributed to the finite ground plane of the fabricated antenna and the infinite ground plane assumed within the calculation.

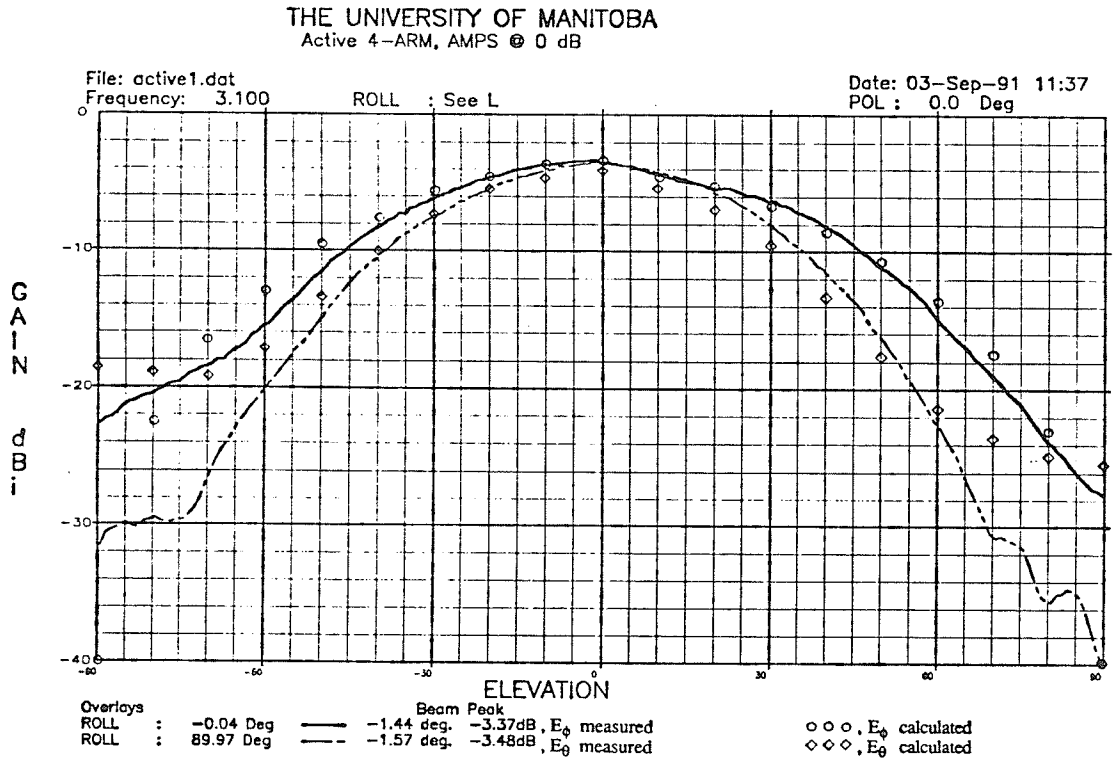

Figure 4.18 : Calculated and measured radiation pattern of active antenna, f=3.1 GHz, $\phi=0^{o}$.

4.6 Noise Temperature

To determine the noise temperature of the developed antenna the noise model presented in section 3.5 was applied. In application to the developed active antenna, G_N and T_{AN} represent the gain and temperature of the integrated amplifiers. Thus the noise model representation is given in Figure 4.19.

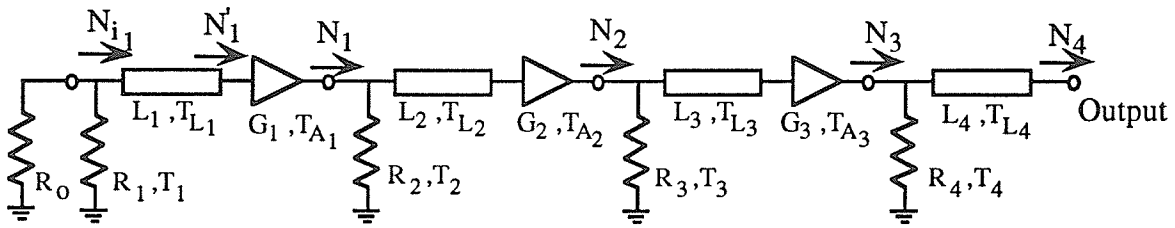

Figure 4.19 : Noise model for fabricated active integrated antenna.

The output temperature can be determined from equation (3.15) yielding

$$T_{out} = \frac{T_{i_4}}{L_4} + \frac{(L_4 - 1)\,T_{L_4}}{L_4} \tag{4.8}$$

where $T_{i_4} = \dfrac{T_{N_3}}{1 + g_{r_4}} + \dfrac{T_4 g_{r_4}}{1 + g_{r_4}}$

$$T_{N_3} = \frac{G_3}{L_3}[T_{i_3} + (L_3 - 1)\,T_{L_3}] + G_3\,T_{A_3}$$

$$T_{i_3} = \frac{T_{N_2}}{1 + g_{r_3}} + \frac{T_3 g_{r_3}}{1 + g_{r_3}}$$

$$T_{N_2} = \frac{G_2}{L_2}[T_{i_2} + (L_2 - 1)\,T_{L_2}] + G_2\,T_{A_2}$$

$$T_{i_2} = \frac{T_{N_1}}{1 + g_{r_2}} + \frac{T_2 g_{r_2}}{1 + g_{r_2}}$$

$$T_{N_1} = \frac{G_1}{L_1}[T_{i_1} + (L_1 - 1)\,T_{L_1}] + G_1\,T_{A_1}$$

and where $T_{i_1} = \dfrac{T_o}{1 + g_{r_1}} + \dfrac{T_1 g_{r_1}}{1 + g_{r_1}}$

The radiation efficiency can be determined from the measured power delivered to the load and the calculated attenuation due to substrate and copper losses [77]. This yields an arm efficiency of 4.6%. Thus the output temperature of the fabricated active antenna was calculated based upon equation (4.8). It is tabulated in Table 4.3 and plotted in Figure 4.23.

A "Y-factor" approach is used where two output noise powers are required to determine the antenna temperature. The Y-factor is the ratio of output noise powers due to two different input noise temperatures [82]. The block diagram is given in Figure 4.20.

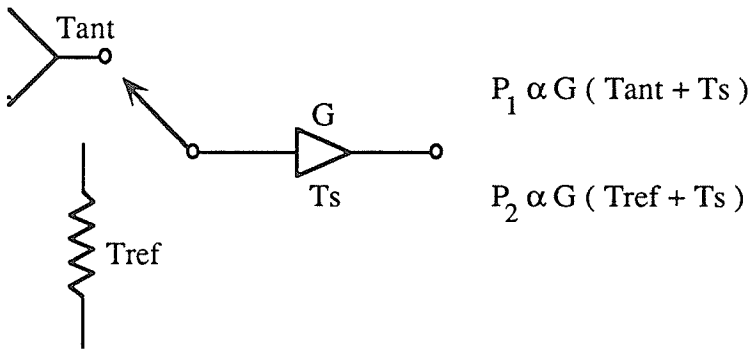

Figure 4.20 : Block diagram of noise temperature measurement.

$$\therefore \frac{P_1}{P_2} = \frac{G(T_{ant}+T_S)}{G(T_{ref}+T_S)} \qquad (6)$$

To control the environment temperature of the antenna, the antenna is placed in a shielded box lined with black absorber. The temperature within the chamber is monitored to ensure a uniform temperature, T_{cham}. Under these conditions, the walls should emit a constant radiation brightness as discussed in [83]. The chamber is constructed such that the antenna is not loaded. This has been verified by measuring the return loss parameter of the antenna in and out of the chamber. Minimal variation was observed as shown for a

passive antenna as well as the active antenna (Figure 4.21). The measurement equipment set-up for Figure 4.20 is given in Figure 4.22 and the procedure is outlined in AppendixV.

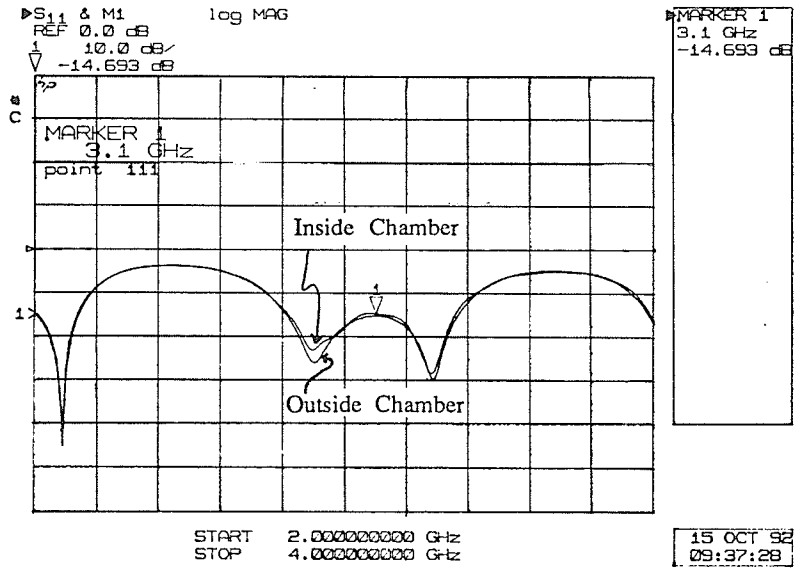

a) Passive antenna

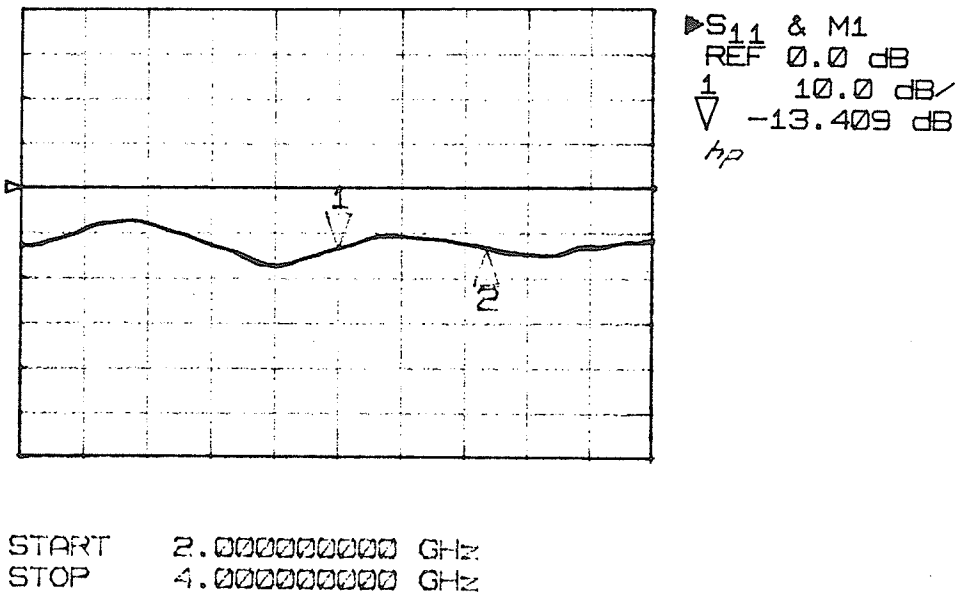

b) Active antenna, amps@7dB

Figure 4.21 : Return loss measurement of antennas inside and outside chamber.

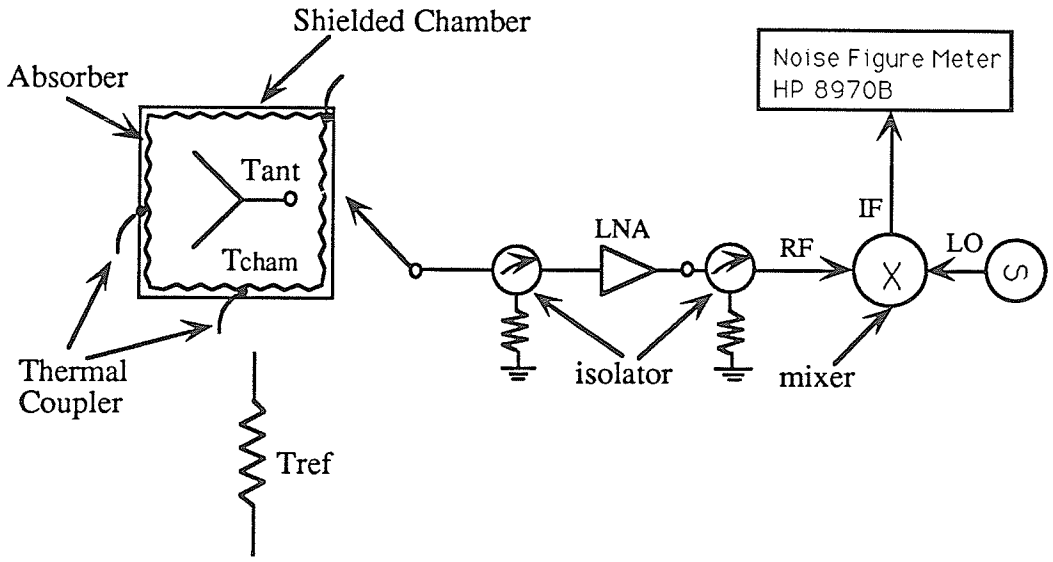

Figure 4.22 : Experimental set-up for antenna noise measurement.

Using the experimental set-up in Figure 4.22, the output noise temperature of the active antenna was measured. The measured temperatures are presented in Figure 4.23 and Table 4.3 along with the calculated temperatures. It should be noted that the amplifiers used in the prototype active antenna have very large noise figures, i.e. NF ~ 12 dB. This translates to temperatures of 4380 K. Thus the output noise temperature is expected to be relatively large. The agreement between the calculated and measured output temperatures is considered to be acceptable, having an average error of 10 %. In addition to the antenna measurement, the noise figure of each amplifier under various bias conditions was measured to facilitate the calculation. The amplifiers were measured using a standard two-port measurement procedure.

$G_1=G_2=G_3$ (dB)	Tout (K) Measured	Tout (K) Calculated
0	12018	13239
2	23865	27557
3	36920	43317
4	62106	68891
5	105746	114655
6	184058	197921
7	328369	352518

Table 4.3 : Calculated and measured output temperature of developed active antenna.

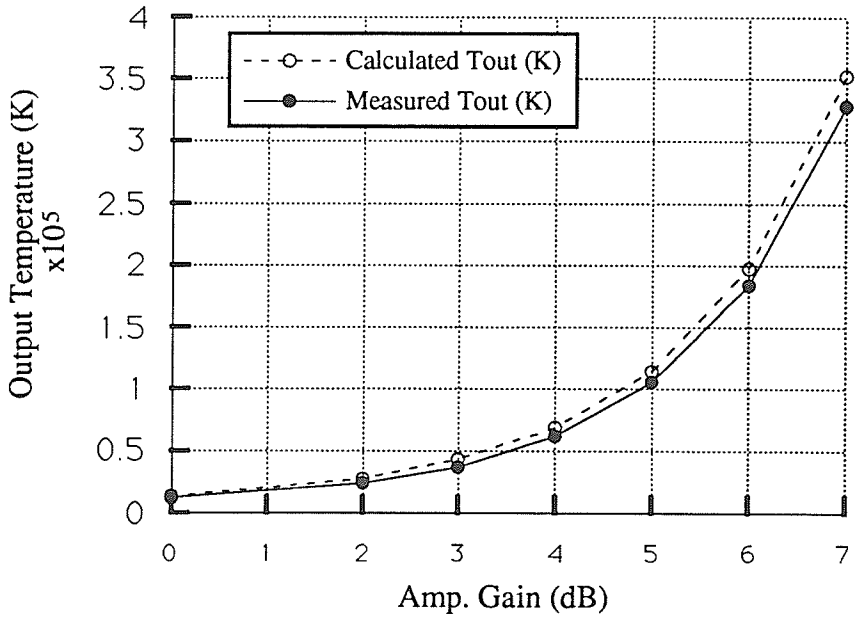

Figure 4.23: Output temperature of active antenna, referenced to 295 K environment, g_r=0.05.

4.7 Discussion

An active integrated antenna has been designed, modelled, fabricated and verified experimentally. The calculated and measured results are in good agreement. The design methodology is versatile and thus allows for the investigation of numerous scenarios. This was demonstrated with the concept of adjusting the internal phase of the active antenna to compensate for the beam squint inherent with travelling wave antennas. Conversely, one could apply this phase adjustment as a means of steering the radiated beam. A model was also developed to calculate the output temperature of an active integrated antenna. This model was verified using a controlled environment. A comparison between experimental and calculated values gives an average error of 10%, which is considered to be satisfactory due to the many variables involved. It should be noted that the developed model can also be applied to other antenna configurations which are composed of active devices and are travelling-wave in nature. The limitation of the model is that a matched system is assumed. Once this condition is violated the model is no longer valid. Provided a matched system is maintained, one can study the effects on system noise temperature due to variations of parameters such as the device gain and noise figure.

CHAPTER 5 : APPLICATIONS OF THE DEVELOPED ACTIVE ANTENNA

As shown in the previous Chapter, the developed active antenna has some interesting characteristics. A patent for this antenna has been filed in the United States [84]. Several operating modes and applications are investigated and presented in this Chapter.

5.1 Phased Arrays

5.1.1 Introduction

A general overview of phased array antennas has been presented in Chapter 2. Here, the developed active antenna is evaluated as a radiating element within an active phased array antenna. An active phased array antenna has been defined as an array where both the supplied current amplitude and phase of each element can be varied. This capability in turns allows the main beam of radiated power to be steered electronically.

The developed active antenna appears to be an attractive element choice because the overall array could be very compact. This is because the amplifiers are integrated within the antenna element itself. It is conceivable that the phase devices could also be integrated either within the antenna or at the output/input. The developed active antenna as is, i.e. four arms, three amplifiers, mode 1 operation, is considered in application to a phased array antenna.

One aspect of the active antenna is that the aperture size is variable. The phase relationship between each arm is partially controlled by the integrated active devices. With the passive structure, the printed transmission line is used to set the phase relationship, thus the minimum aperture size is fixed with a diameter of approximately 1.42 λ [77], where $\lambda=\lambda_o$. The diameter of the active antenna can be reduced to less than 1.42 λ, as well as being increased. This is an interesting aspect when considering scanning properties and grating lobes. This was investigated through computer simulations.

As discussed in Chapter 2 and outlined in [85], the far-field radiation pattern of an array of identical elements is equal to the product of the field of a single element and the array factor of that array. The array factor is a function of the number of elements, their geometrical arrangement, relative magnitudes and phases, and their spacing. The array factor for a planar array is given below with its geometry in Figure 5.1 [85].

$$AF = \sum_{n=1}^{N} I_n \left[\sum_{m=1}^{M} I_{m1} e^{j\,(m-1)\,(k\,dx\,\sin\theta\,\cos\phi + \beta_x)} \right] e^{j\,(n-1)\,(k\,dy\,\sin\theta\,\sin\phi + \beta_y)} \qquad (5.1)$$

where $\beta_x = -k\,dx\,\sin\theta_o\,\cos\phi_o$

$\beta_y = -k\,dy\,\sin\theta_o\,\sin\phi_o$

θ_o, ϕ_o define the direction of the main beam

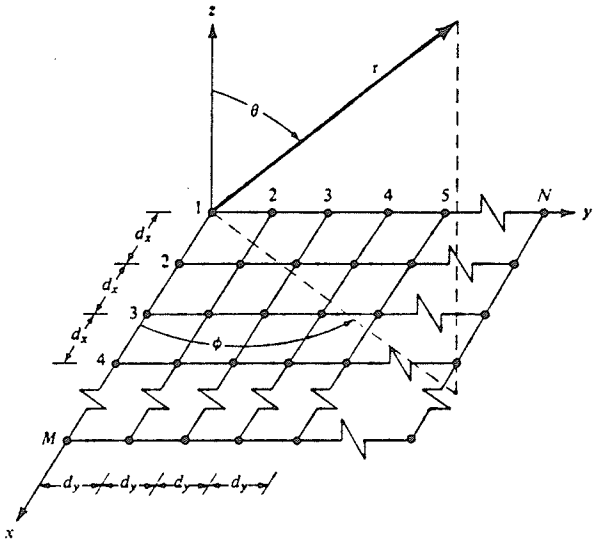

Figure 5.1 : Rectangular grid planar array geometry [85].

The equation for the element pattern used in the calculation is given in Chapter 4, equations 4.5, 4.2 b) and 4.6, 4.3 b) and repeated below

$$E_\theta = f_n(\theta)\, e^{j(n\phi - \frac{\pi}{2})} \qquad (5.2a)$$

$$E_\phi = g_n(\theta)\, e^{jn\phi} \qquad (5.2b)$$

where $f_n(\theta) = -\frac{\omega\mu a}{4}\frac{e^{-jkr}}{r} j^n \cos\theta \left[J_{n+1}(ka\sin\theta) + J_{n-1}(ka\sin\theta)\right]$

$$g_n(\theta) = -\frac{\omega\mu a}{4}\frac{e^{-jkr}}{r} j^n \left[J_{n+1}(ka\sin\theta) - J_{n-1}(ka\sin\theta)\right]$$

Pattern multiplication with the array factor given in equation (5.1) and the element pattern in (5.2) was coded to provide computer simulations of the phased array (Appendix VI). It should be noted that mutual coupling has been neglected to simplify the problem. The loop diameter of equation (5.2) was varied with the results given in Figure 5.2. As can be seen, the grating lobe appears immediately. The maximum scan angle possible is $\pm 15^o$. The radiation pattern of the array when scan angles exceed 15^o are dominated by the grating lobe (Figure 5.2 d)). With the active antenna element, it is possible to reduce the element size, thus reducing the element spacing. This should increase the scan angle of the array. Elements having diameters of 0.4 λ and 0.5 λ were simulated. A 15x15 element array size is required to generate approximately the same gain as the previous array. The scan performance is given in Figure 5.3. As can be seen the maximum scan angle has been increased to $\pm 50^o$. The radiated pattern degrades for scan angles exceeding 50^o.

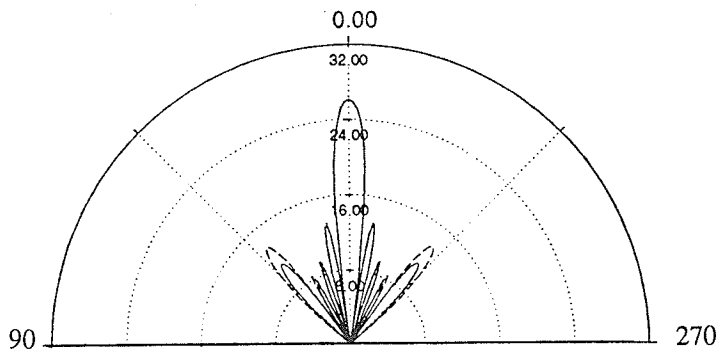

a) beam (0,90)

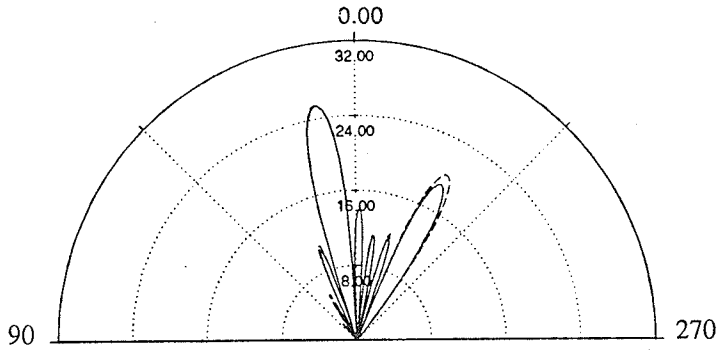

b) beam (10,90)

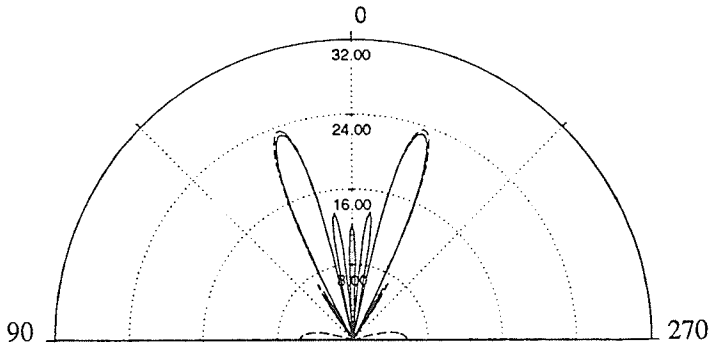

c) beam (20,90)

Figure 5.2 : Calculated elevation pattern, (ϕ=90°), of 5 x 5 rectangular array, element dia.= 1.42λ, - - - E_θ, —— E_ϕ.

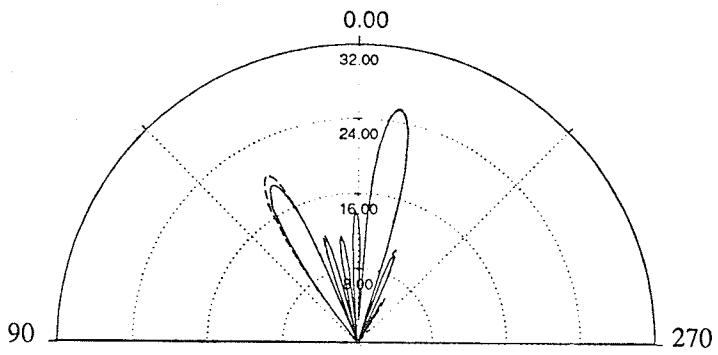

d) beam (30,90)

Figure 5.2 (cont.)

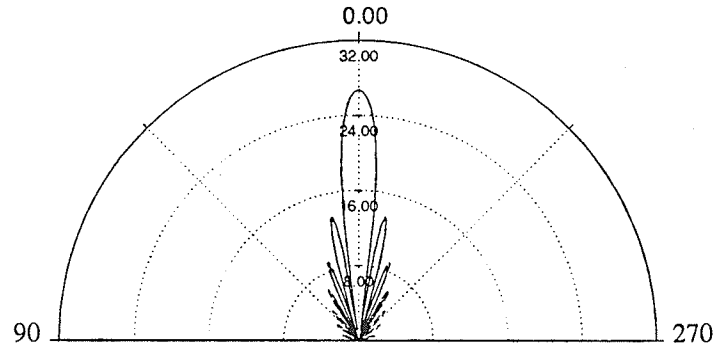

a) beam (0,90)

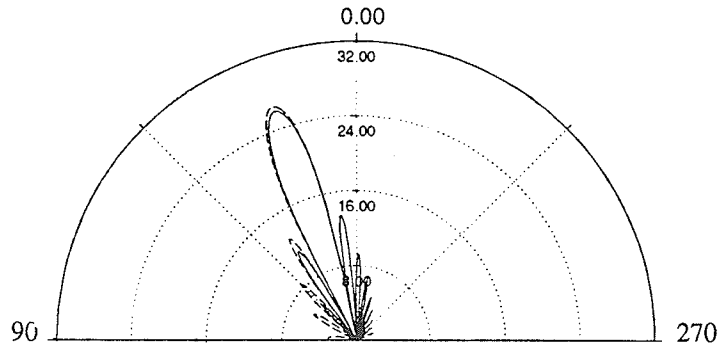

b) beam (20,90)

Figure 5.3 : Calculated elevation pattern, (ϕ=90^o), of 15 x 15 rectangular array, element dia.= 0.4λ, - - - E_θ, —— E_ϕ.

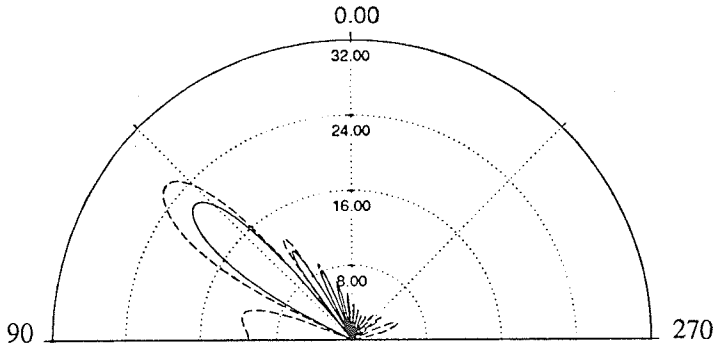

c) beam (50,90)

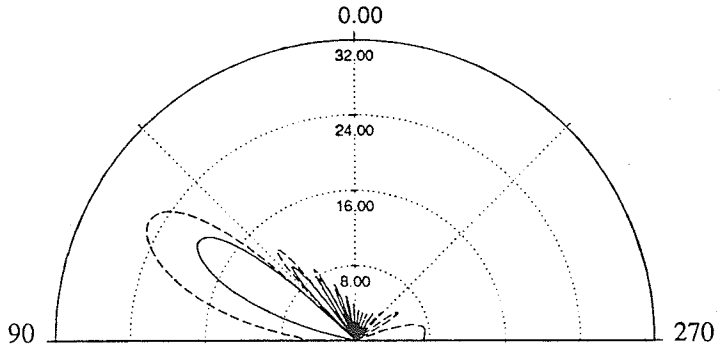

d) beam (60,90)

Figure 5.3 (cont.)

Another control mechanism for grating lobes is the array grid. A proper grid selection can minimize grating lobes and completely eliminate grating lobes in certain locations [45], [86], [87]. For example, a rectangular grid has grating lobes at $n\pi/2$ while triangular grids have grating lobes at $n\pi/3$. Thus to minimize grating lobes in the $\phi=90^{o}$ plane, a triangular grid should be utilized (Figure 5.4, [86]). This has been analysed by separating the triangular array into two interlaced rectangular arrays where the resultant pattern is the sum of the two rectangular array patterns. The scan performance of a triangular array containing 179 elements is presented in Figure 5.5. As can be seen, the grating lobe is suppressed

until a scan angle of 60^{o} is reached. Beam pointing at $\theta=70^{o}$ is possible with this configuration. However there is a large drop in peak gain (Figure 5.5d)).

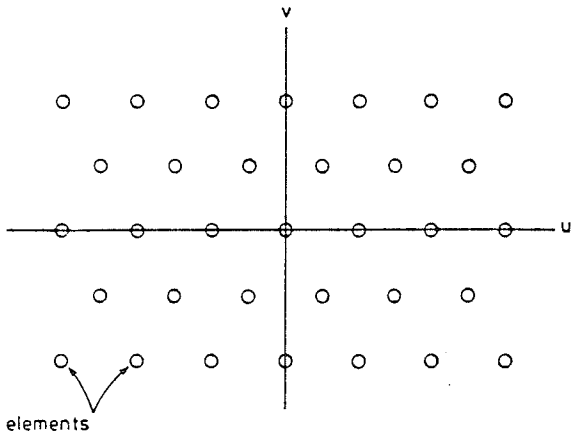

Figure 5.4 : Triangular grid array [6].

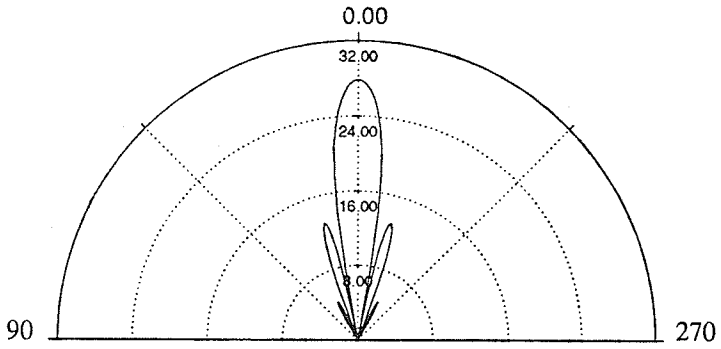

a) beam (0,90)

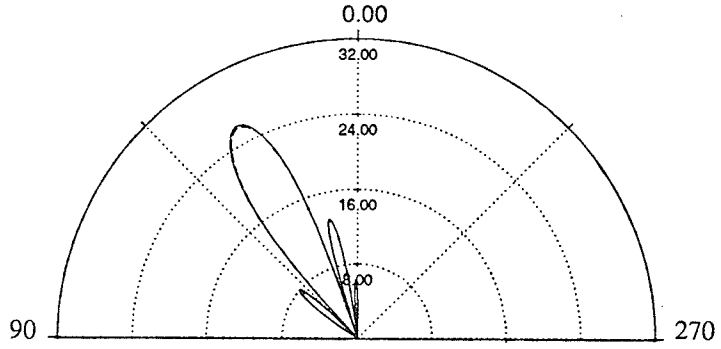

b) beam (30,90)

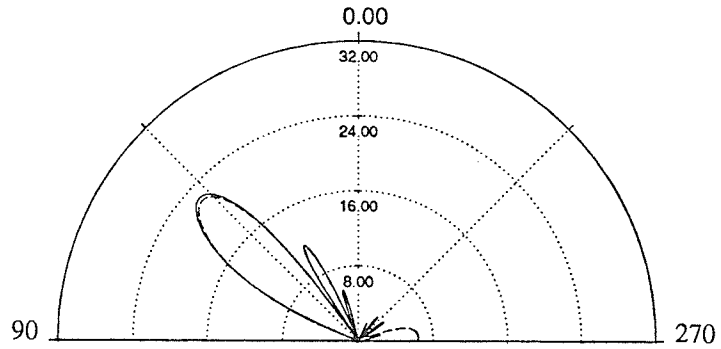

c) beam (50,90)

Figure 5.5: Computed elevation pattern, (ϕ=90^{o}), of 179 element triangular array, element dia.= 0.5λ, - - - E_{θ}, —— E_{ϕ}.

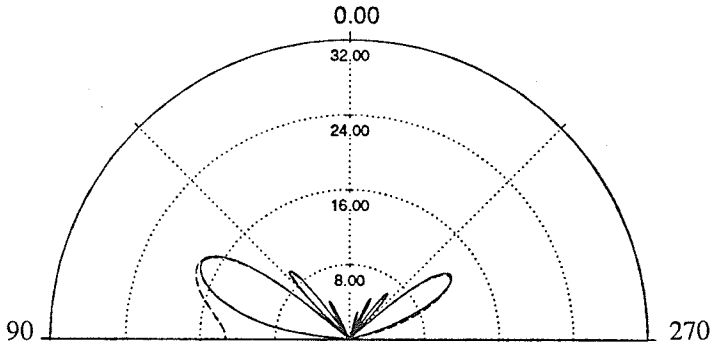

d) beam (70,90)

Figure 5.5 (cont.)

5.1.2 G/T of an Active Phased Array

The gain to noise temperature ratio, G/T, is commonly used as the figure of merit for receive antennas. This is an important consideration when evaluating the active antenna element. A single active antenna element can achieve high gains because of the integrated amplifiers. The gain available at the output of the antenna is considered to be the achievable gain of the antenna. This output gain is a combination of two sources; i) the gain due to the physical aperture, and ii) the gain due to the amplifiers. This explains why high peak gain values are obtained with relatively broad half power beam widths (Figure 4.14 g)). Thus the gain requirements of array applications can be achieved with just a few elements, however, the noise temperature must be addressed to satisfy the required G/T specification. The developed active antenna element was evaluated by comparing it with array architectures which utilize passive radiating elements.

The three array architectures studied are given in Figure 5.6. The structure of Figure 5.6 a) has been classified as "semi-active". This structure uses passive radiating elements, a feed network between these elements, and a single amplifier. This structure is classified as semi-active because each element has phase control only, i.e. no amplitude control. The structure of Figure 5.6 b) is fully active and uses passive radiators. Each element has to supply both amplitude and phase control. The last structure, Figure 5.6 c) is an array utilizing the developed active antenna element.

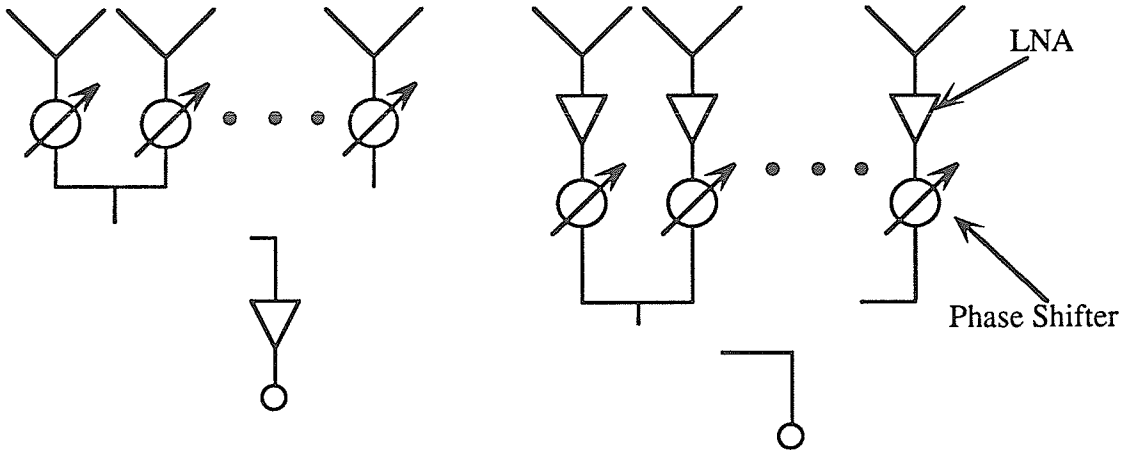

a) Semi-active, passive elements

b) Fully active, passive elements

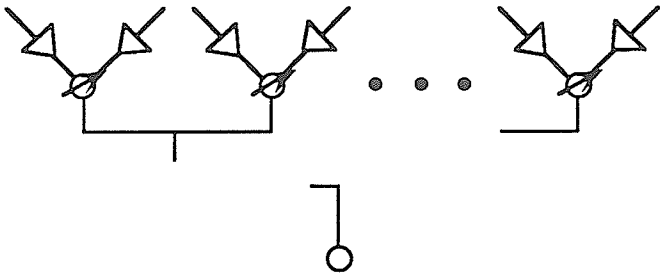

c) Fully active, active elements

Figure 5.6 : Three different array architectures.

The G/T of a single element of each architecture is compared. The noise temperature, T, of these arrays comprises the antenna temperature and the system temperature, i.e. $T = T_{ANT} + T_{CKT}$. The antenna temperature is generated by losses within the antenna, T_{INT}, and the external temperature, i.e. the sky and ground temperature "seen" by the antenna, T_{SKY}. The system temperature, T_{CKT}, is defined as the temperature contributed by the passive and active circuitry, such as the feed network, T_{FN}, phase shifter, T_{PS}, and the low noise amplifier (LNA), T_{LNA}.

$$T = T_{ANT} + T_{CKT}$$

where $T_{ANT} = T_{SKY} + T_{INT}$

$$T_{CKT} = T_{FN} + T_{PS} + T_{LNA}$$

The plane of reference used for the three cases is at the output of the amplifiers. All losses incurred prior to the LNA add directly to the noise figure while losses incurred after the LNA are a second order contribution to the noise temperature provided the LNA has a sufficiently large gain. This can be seen from the following simple generalized example.

Example :

Case i)

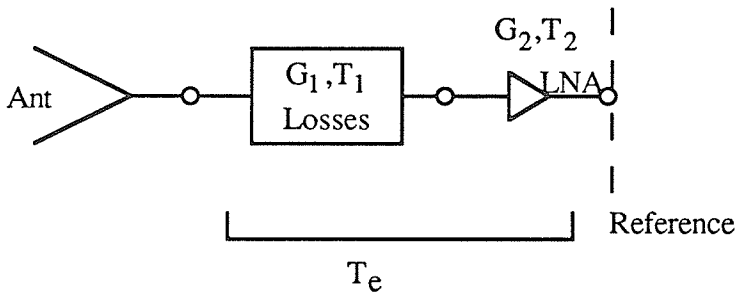

$$T_e = T_1 + \frac{T_2}{G_1}$$

$$T_{Ref} = (T_{ANT} + T_e)G_1G_2$$

$$\therefore T_{Ref} = (T_{ANT} + T_1 + \frac{T_2}{G_1})G_1G_2$$

Case ii)

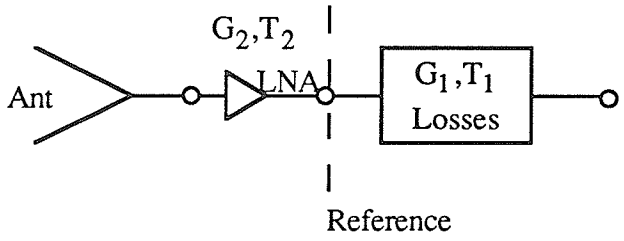

$$T_e = T_2 + \frac{T_1}{G_2}$$

$$T_{Ref} = (T_{ANT} + T_e)G_2$$

$$\text{but } \frac{T_1}{G_2} \cong 0 \text{ if } G_2 >> 1$$

$$\therefore T_{Ref} \cong (T_{ANT} + T_2) G_2$$

Thus an important aspect in array design is to minimize the losses between the antenna element and the LNA. It is apparent that the semi-active architecture is susceptible to poor noise temperatures as the feed network and phase shifter preceed the LNA. To draw some conclusions an example is presented. To compare the three architectures, assume that all elements have the same aperture gain. This is considered to be the peak gain obtained by the active antenna element when the amplifiers are biased for 0 dB gain. Therefore the aperture gain is G_{AP} = -3.6 dB. In addition, parameters such as sky noise and LNA and phase shifter noise figures are assumed to be identical for each scenario. The example utilizing the three array architectures is given below where the G/T of a single element is calculated.

i) Semi-active, passive elements (Figure 5.6 a))

As mentioned above, the phase shifter and feed network are located prior to the LNA. The feed network losses of a corporately fed microstrip array (16x16) is found to vary between 2.6 dB to 45 dB depending upon the impedance of the transmission line and the thickness of the substrate [88]. A 3 dB loss is assumed here for each the feed network and the phase shifter, the microstrip antenuation is assumed to be 10K. Thus the system may be represented as

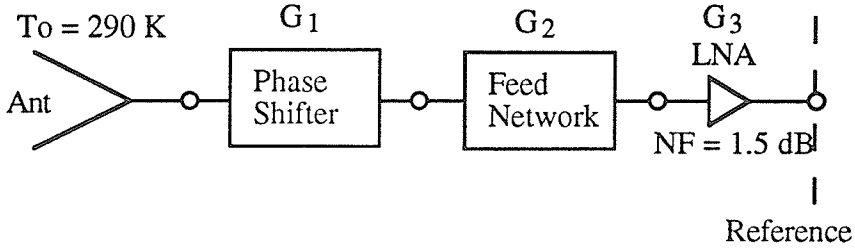

Note : $T = (NF-1)T_o$

$$\therefore T_{CKT} = \left(T_{PS} + \frac{T_{FN}}{G_1} + \frac{T_{LNA}}{G_1 G_2} \right) G_1 G_2 G_3$$

$$T_{CKT} = 2165.9\, G_1 G_2 G_3$$

$$T = (T_{ANT} + T_{CKT})\, G_1 G_2 G_3$$

$$\text{and } T_{ANT} = 290 + 10 = 300 \text{ K}$$

$$\therefore \frac{G}{T} = \frac{G_{ANT}}{T_{ANT} + T_{CKT}} \text{ , where } G_{ANT} = 0.4365$$

$$\boxed{\therefore \frac{G}{T} \cong -37 \text{ dB/K}}$$

ii) Fully-active, passive elements (Figure 5.6 b))

This architecture brings the LNA to the output of the antenna element. Thus the losses due to the phase shifter and feed network are second order. The G/T may be determined to be

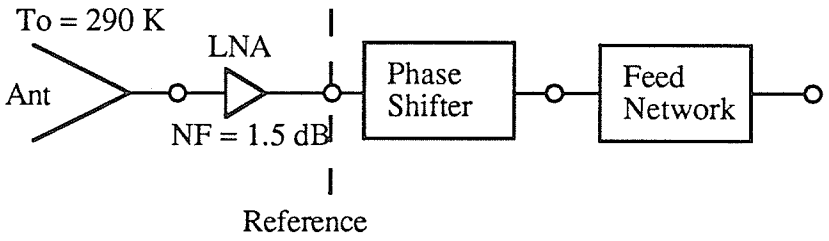

$$T \cong (T_{ANT} + T_{CKT})G$$

$$\cong (T_{ANT} + T_{LNA})G$$

$$\boxed{\therefore \frac{G}{T} \cong -30 \text{ dB/K}}$$

iii) Fully-active, active elements (Figure 5.6 c))

The G/T is calculated based upon measured gain and the developed noise model. The G/T for the developed active antenna having amplifiers with noise figures of 1.5 dB is tabulated in Table 5.1. Again, the phase shifter and feed network introduce second order losses.

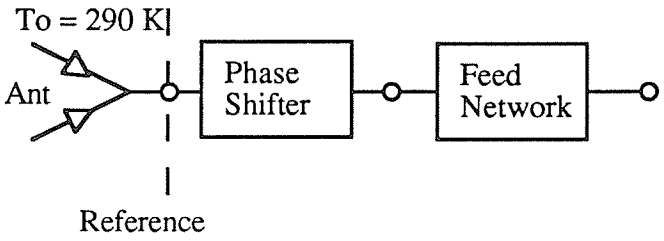

Amplifiers (dB)	Tout (K)	Gpeak (dB)	G/T (dB/K)
0	611.4	-3.6	-31.5
2	1902.5	0.1	-32.5
4	6594.0	4.0	-34.2
7	47328.5	11.0	-35.8

Table 5.1 : G/T of active antenna element, $T_{ref} = 290$ K, $NF_{amp} = 1.5$ dB, $g_r = 0.049$.

As can be seen, as the gain increases, the G/T degrades. This is because the amplifiers are amplifying the noise as well as the signal.

Comparing the G/T of the three architectures it is apparent that the best configuration for optimal G/T performance in an array is the fully active array using passive antenna elements. This architecture has an improved G/T of 1.7 to 5 dB when compared to the array using active elements. However, the fully active array using active elements has a superior G/T when compared to the semi-active array architecture. In fact, in situations

where the feed network loss is greater than 3 dB then the benefit of using active antenna elements is more pronounced. The actual implementation/fabrication of the active array utilizing the developed active antenna element is now considered.

5.1.3 Implementation of an Active Element Phased Array

From a fabrication point of view, phased arrays, whether using active or passive elements, are complex. Fundamental issues governing the fabrication of phased arrays are :

i) array architecture

ii) integration of active devices

iii) bias supply/control to active devices

These issues must be considered when implementing active or passive elements. These issues, related to the implementation of active elements, are discussed.

i. Array Architecture

Three array architectures are considered (Figure 5.7). The planar architecture (Figure 5.7 a)) is one where all circuitry, feed lines, and radiating elements are on the same substrate surface. The drawing in Figure 5.7 a) is not to scale and does not show all details. It should be noted that the bias supply network requires d.c. bias and ground lines. In addition to the amplifiers shown, a phase shifter per element is required along with its control bias network. From an operational view point this architecture could be prone to potential coupling problems from the radiating elements to the bias network. This is an area which would require study if one were to pursue this type of architecture.

The multilayer architecture (Figure 5.7 b)) is one where the radiating elements and circuitry are situated on separate substrates sharing a common ground plane. Coupling

from the circuitry to the radiating elements may be achieved by slots or probes. This architecture eliminates any interference that the circuit network may impose on the antenna performance. This may be difficult from a fabrication view point in that exact alignment is critical for the slot coupling mechanism and the probe coupling mechanism requires many via holes.

The architecture shown in Figure 5.7 c) utilizes a combination of planar and multilayer concepts. The active portion, which consists of amplifiers and microstrip transmission lines are incorporated on the same substrate. The feed and bias networks are situated on a substrate sharing the same ground plane where coupling is achieved with slots or probes. Bias connections require via holes or probes where RF coupling can be achieved with slots or probes. This architecture eliminates potential bias network interference problems and is not as complex as a complete multilayer structure.

The fabricated active element presented in Chapter 4 is based upon the combination architecture illustrated in Figure 5.7 c). This fabrication concept was extended further to incorporate MHMIC technologies. The concept was that all active circuitry could be fabricated on a Alumina substrate using MHMIC technology and this "chip" of active circuitry could then be placed into the centre of each radiating element. The connection of transmission lines would be achieved via wire bonds. This approach was carried out and reported in [89]. The fabricated active element is presented in Figure 5.8. Three amplifiers and a continuous variable phase shifter are fabricated on the Alumina substrate. This "chip" in turn was integrated with the duroid substrate to complete the antenna structure. This process also demonstrates the "mother board" concept where separate components/circuits are fabricated separately and then integrated with a main board. The measured radiation patterns at the centre frequency of 1.8 GHz are presented in Figure 5.9. As with the previous structure, the radiated fields are broadside and circularly polarized.

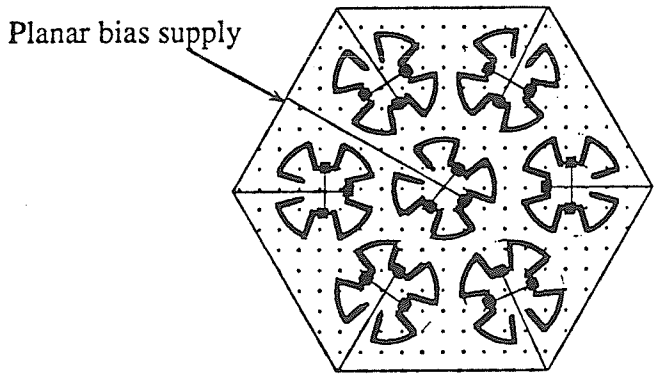

a) Planar architecture

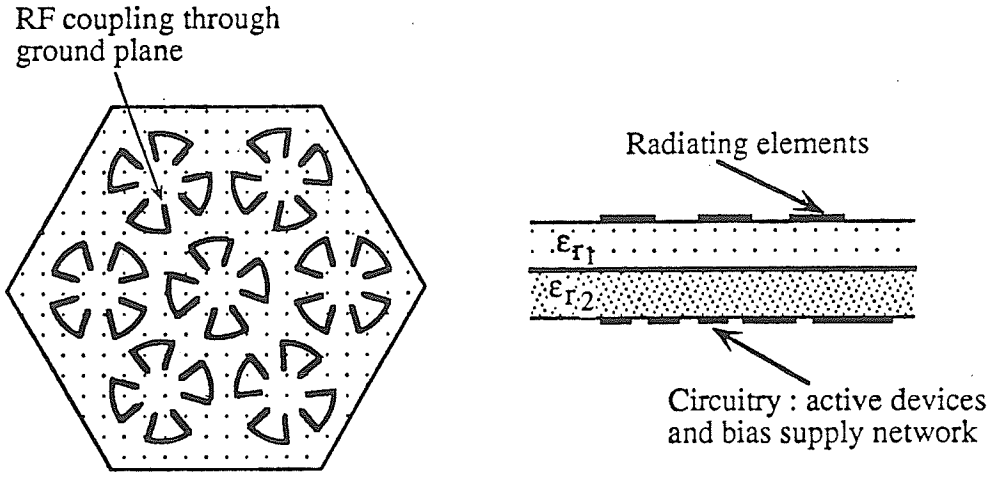

b) Multilayer architecture

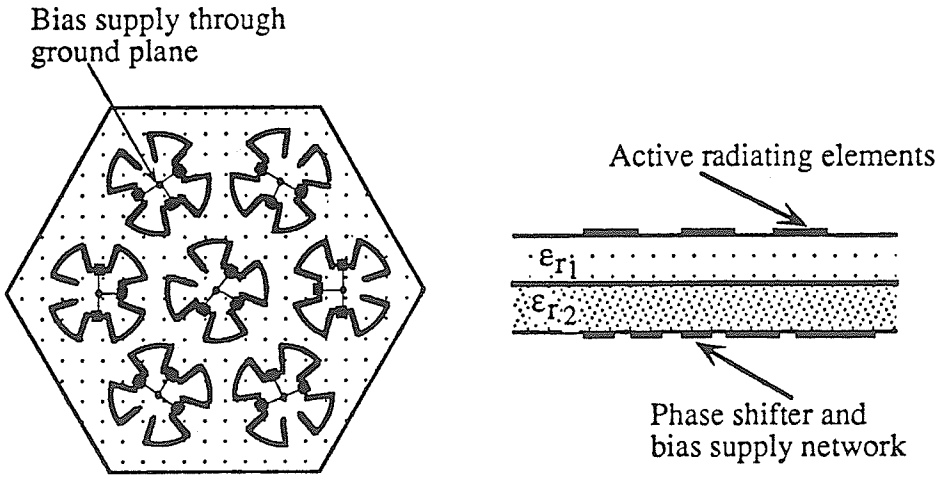

c) Combination architecture

Figure 5.7 : Active element array implementation.

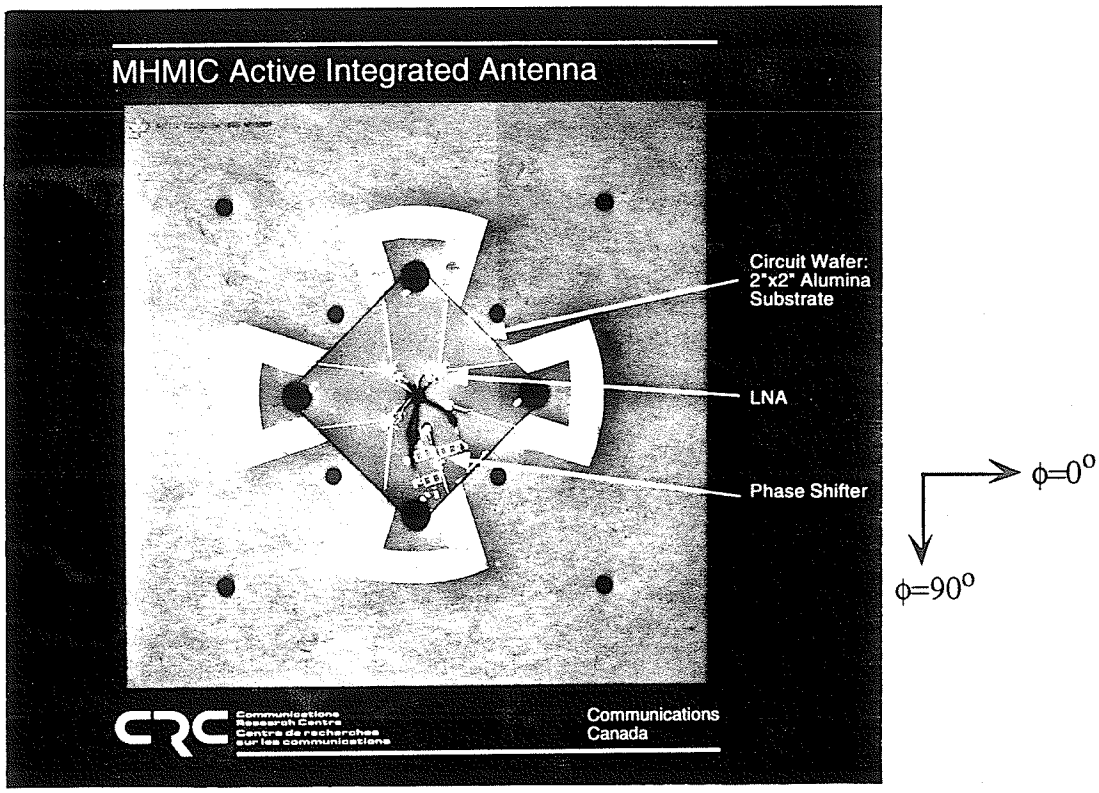

a) MHMIC active antenna

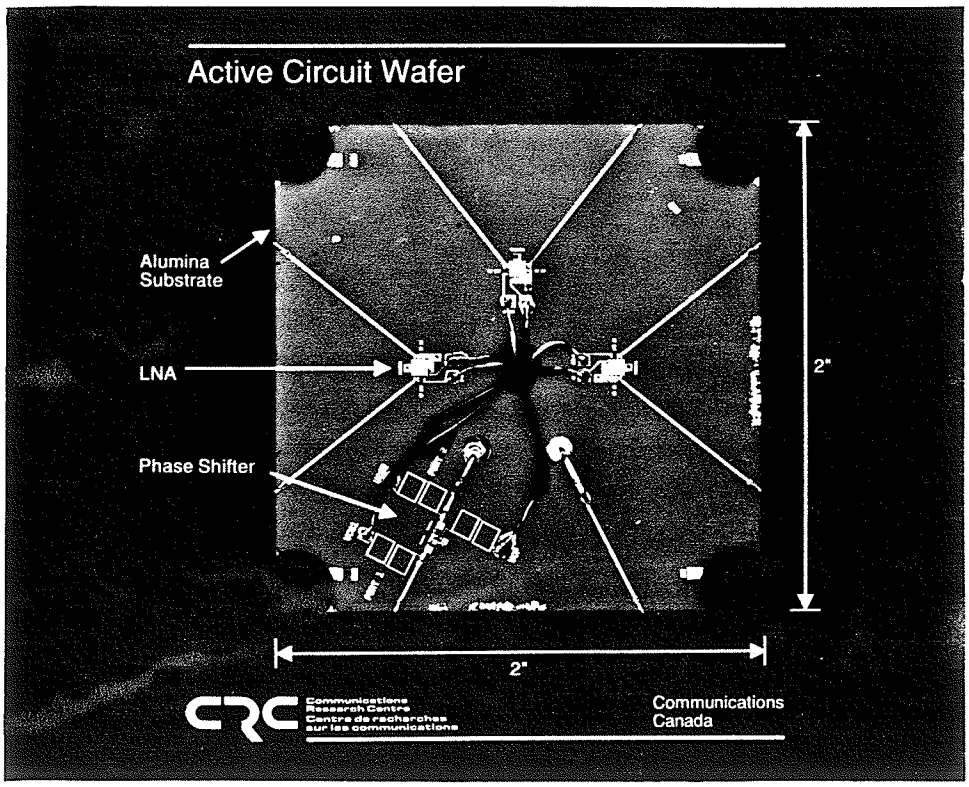

b) Integrated active circuitry

Figure 5.8 : Fabricated MHMIC active antenna.

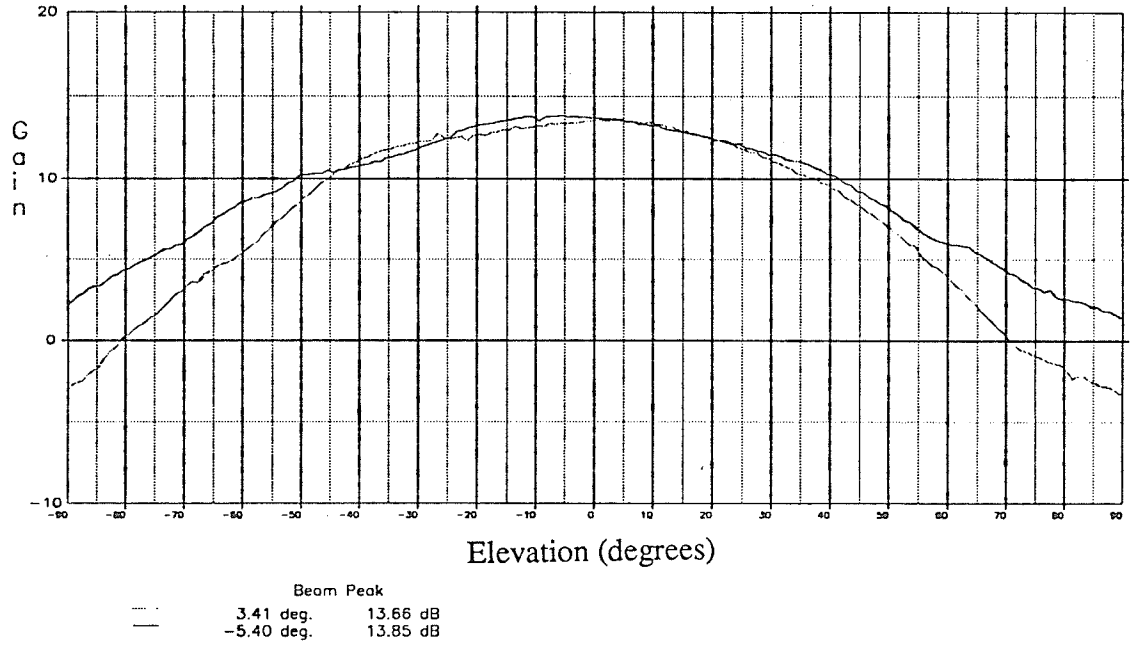

a) $\phi=0^o$

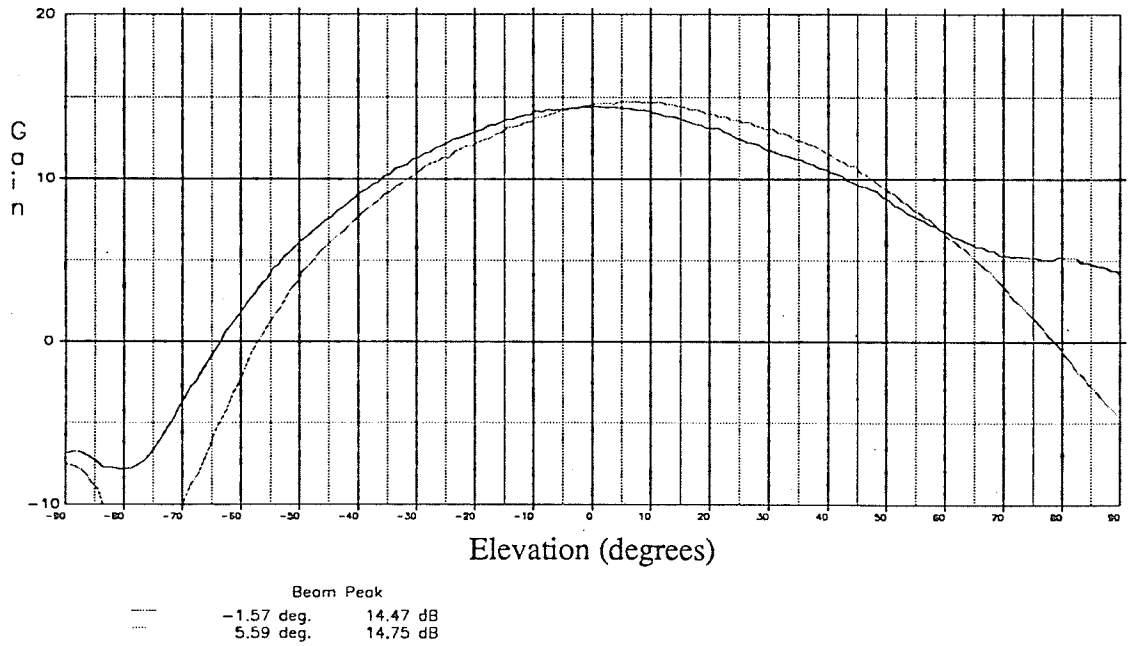

b) $\phi=90^o$

Figure 5.9 : Measured radiation patterns of MHMIC active antenna, f=1.8 GHz, - - - - E_θ, —— E_ϕ.

5.2 Pattern Reconfiguration

5.2.1 Introduction

A unique feature of the developed antenna in its present topology is that the radiated pattern may be reconfigured with the integrated active devices. This may be achieved by altering the current phase distribution along the antenna structure. The fabricated antenna has been demonstrated to operate in its first order broadside mode and a higher order mode where conical shaped patterns are generated. This antenna could have potential applications within mobile communication systems where a minimal antenna size is desired.

5.2.2 Modal Operation

The radiation properties of this active element have been presented in Chapter 4. There it was shown that the developed active antenna is related to a circular loop. It was also shown how the far field is dependent upon the Bessel functions, eq'ns (4.5, 4.6). By selecting various orders of the Bessel function one can change the radiation characteristics of the loop. One technique to do this is to vary the loop circumference according to $n2\pi$. For n equal 1 (mode 1), the zero-order Bessel function is dominant and hence the resultant is a broadside pattern. For other orders of the Bessel function (modes) the resultant is an omni-directional type pattern (i.e. centre null) with varying elevation angles. As the order of Bessel function increases, the radiated beam peak approaches the horizon. A modal investigation of a circularly polarized loop was carried out to determine the radiation characteristics associated with each mode of operation.

A passive circularly polarized loop was analysed numerically with NEC for various modes of operation. The graph in Figure 5.10 a) shows the elevation angle of the beam

peak as a function of modal operation. As can be seen, the elevation angle of the beam peak approaches 30^{o} as the mode of operation increases. However, the circumference of the loop increases by $1\lambda_{eff}$ for every increase in modal operation. Thus if low elevation angles are required, a large circumference and therefore surface area will also be required.

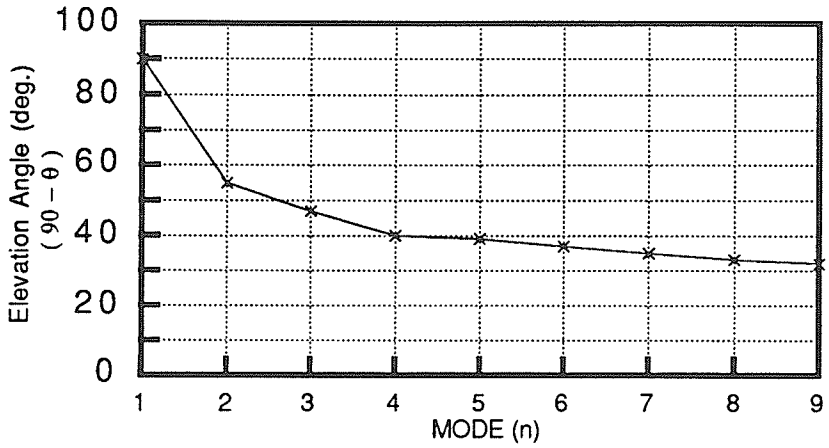

Figure 5.10 a) : Elevation angle of beam peak as a function of loop operational mode.

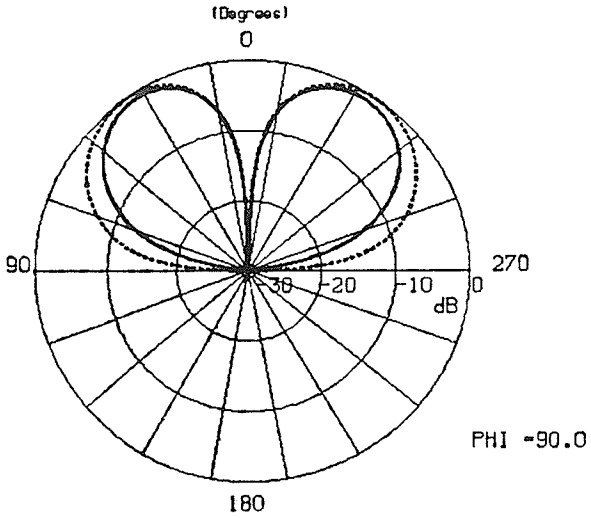

Figure 5.10 b) : Computed elevation pattern of loop operating in mode 2, ——E_{θ}, - - - E_{ϕ}

A unique feature of the developed active antenna is that the pattern can be reconfigured to several different modes at the desired frequency with the single element. By providing phase control devices, located as shown in Figure 5.11, various phase distributions along the outer circumference of the antenna may be obtained by supplying the

necessary bias conditions. Each phase distribution generated corresponds to a mode of operation. The fabricated active antenna utilizes amplifiers to provide both phase and gain control. The antenna was designed such that the phase associated with each amplifier, at the design frequency of 3.1 GHz, produces a 2π continuous phase distribution along the outer circumference of the antenna. This produces a circularly polarized broadside (mode 1) radiated pattern (Figure 5.12 a)). As no phase control devices were integrated in this prototype, other modes of operation can only be observed at other frequencies. By determining the phase response (to frequency) of the amplifiers and accounting for the variations in electrical length of the transmission lines, one can determine frequency points which correspond to other modes of operation. The active antenna presented was determined to operate in mode 2 at f=3.5 GHz. At this frequency, a discrete phase distribution exists along the outer circumference of the antenna such that the total phase distribution of $n2\pi$, where n=2, is satisfied. This was verified experimentally with a pattern measurement as shown in Figure 5.12b). The resultant pattern is circularly polarized and conically shaped with an elevation angle of ~ 47^{o}. These radiation characteristics correspond with the computed pattern given in Figure 5.10 b).

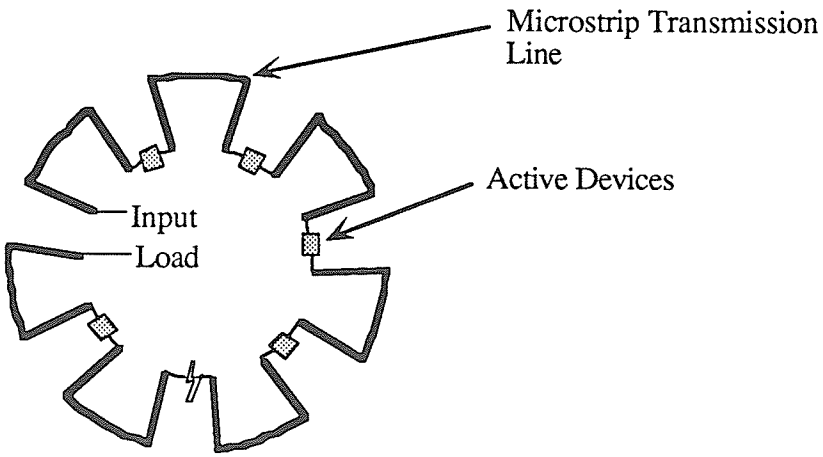

Figure 5.11 : General configuration of active integrated antenna.

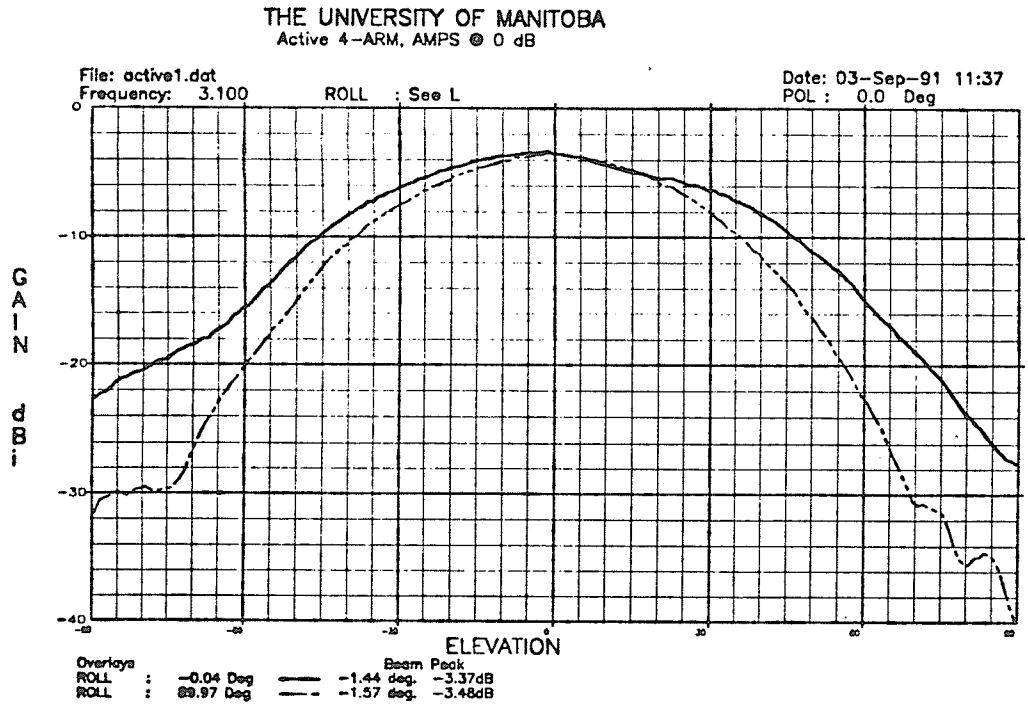

Figure 5.12 a): 4-arm active antenna with amps@0 dB gain, MODE 1 operation, f=3.1 GHz, - - - - E_θ, —— E_ϕ.

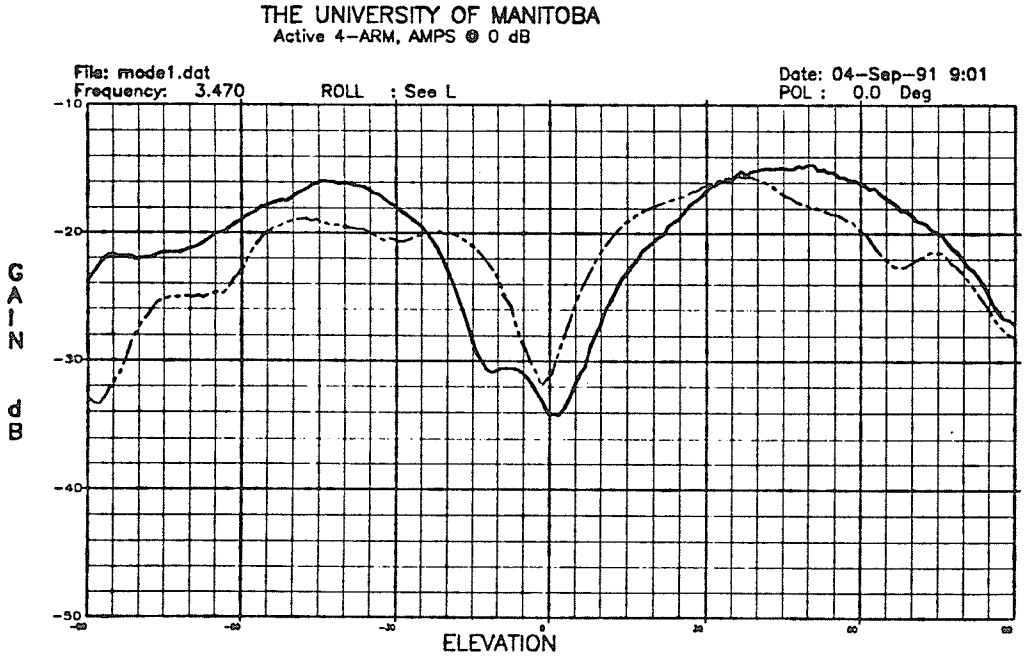

Figure 5.12 b) : 4-arm active antenna with amps@0 dB gain, MODE 2 operation, f=3.47 GHz (note : amplitude axis is not calibrated).

This scenario, i.e. the fabricated active antenna operating at 3.47 GHz, was modelled with the developed design methodology. The active antenna was simulated at this frequency point where the amplifier characteristics at this frequency were included in the scattering parameters. The calculated patterns are given in Figure 5.13. There is relatively good agreement between the calculated and measured patterns (Figure 5.12 b)).

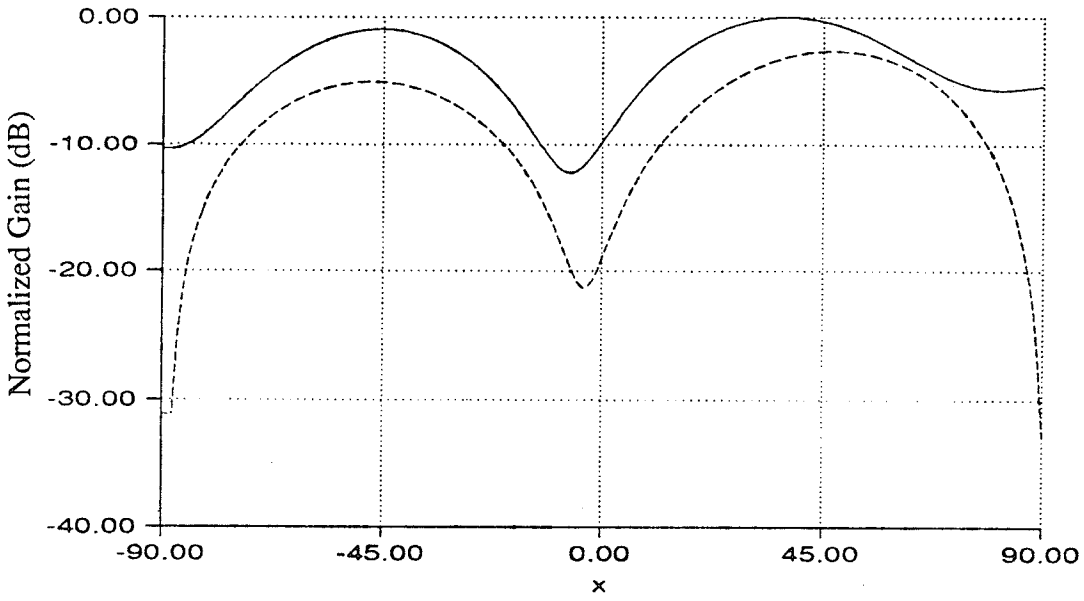

Figure 5.13 : Calculated radiation pattern of active antenna, f=3.47 GHz, —E_θ, - - - E_ϕ.

An active antenna was then modelled where two modes, Mode 1 and Mode 2, can be excited at a single frequency point by varying the phase along the antenna. The second mode was excited at the operating frequency by operating the active devices with an additional phase state. Thus the scattering parameters of the devices were modified such that each device introduced an additional 120^o phase shift, thus the three devices would contribute an additional 360^o. The total phase progression would then be 720^o (or 4π). The calculated pattern for Mode 2 operation at f_c is given in Figure 5.14. As can be seen Mode

2 is not "purely" excited as the centre null is partially filled. It is apparent that Mode 1 is present when Mode 2 is excited. The first mode is present because the fabricated transmission line segments are $\lambda/4$ at the operating frequency. Thus there will always be a continuous phase progression of 2π at the centre frequency. Hence Mode 1 is supported while other modes are excited at this single frequency. In the case of the second mode operation at 3.47 GHz, the conditions necessary to support the first mode do not exist, hence the result is a pattern with a deep centre null (corresponding to Mode 2).

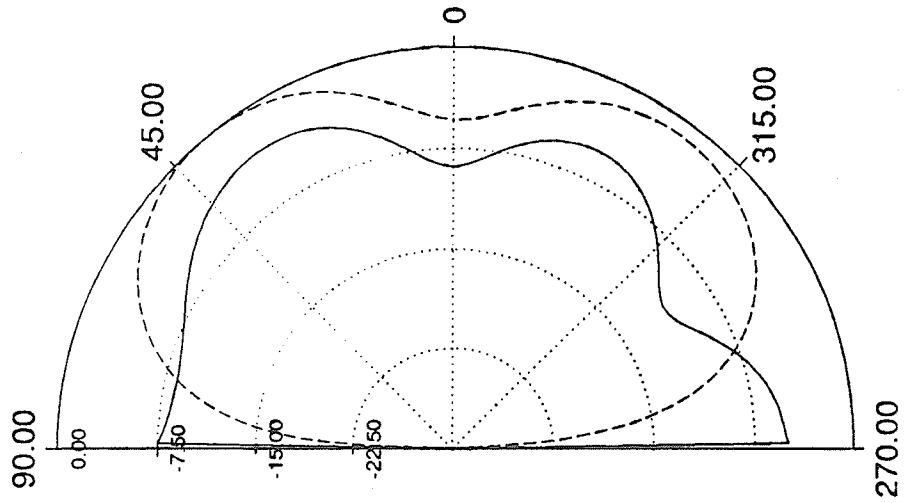

Figure 5.14 : Calculated radiation pattern of active antenna at centre frequency when phase is induced to support Mode 2, — E_θ, - - - E_ϕ.

Thus it is apparent that it would be difficult to excite purely multiple modes of operation at a single frequency point by simply changing the phase conditions along the antenna. In terms of multi-mode operation, depending on the application of course, it may be desirable to design the initial condition of the antenna for a higher order mode and use the phase shifting to excite other higher order modes. This would ensure a deep centre null as the antenna would not be able to support Mode 1 (broadside).

It is also apparent that the active antenna has the capability of beam shaping. That is, by controlling the phase along the antenna, one can excite various modes and shape the radiated pattern. A version of this concept was investigated in application to beam steering.

5.2.3 Beam Steering by Mode Summing

As proposed in [90], [91], the radiated beam of an antenna may be steered by the linear sum of modes. This is briefly summarized in Figure 5.15. Consider an element where four excitation ports are available. Mode 1 can be excited if each port is equal in magnitude and in phase quadrature. Mode 2 can be excited if adjacent ports are equal in magnitude and 180^{o} out of phase. The linear sum of modes 1 and 2 yields an excitation of Figure 5.15 c). As can be seen, the beam will scan in the direction shown. By appropriately weighting each port, one can scan the beam in azimuth or combine other modes to steer the beam in elevation.

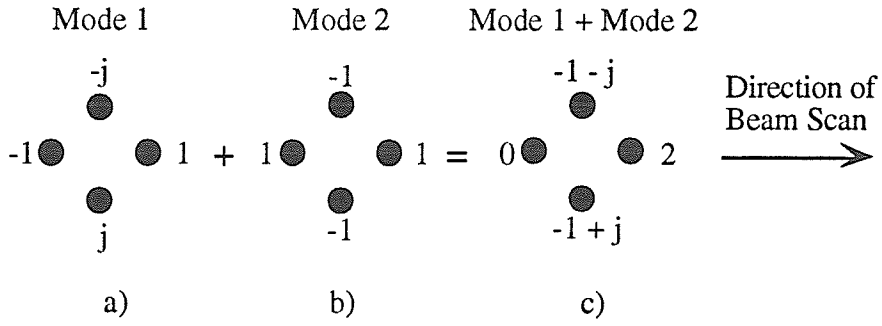

Figure 5.15 : Mode summing.

This concept applied to the active antenna element was investigated by using the developed design methodology. The scattering parameters of the active devices were adjusted such that the four arms would be "weighted" and phased in accordance to the sum of Mode 1 and Mode 2 (Figure 5.15 c)). Because the structure is series distributed , some

devices function as attenuators while others as amplifiers. The induced phase also takes into account the microstrip transmission line. The calculated elevation and azimuth patterns of the active antenna operating in this mode summing condition are presented in Figure 5.16. These patterns show that the beam can be steered by mode summing. As expressed in [90], the beamwidth in the azimuth plane is proportional to $2\pi/N$, where N is the number of modes. Figure 5.16 b) shows a half power beamwidth of approximately 180^{o}. A few irregularities can be seen in the azimuth cut. However, one could probably adjust the distribution along the antenna to "fine tune" the pattern. In addition, because the active antenna is a series structure, an absolute zero current component on the back arm cannot be generated.

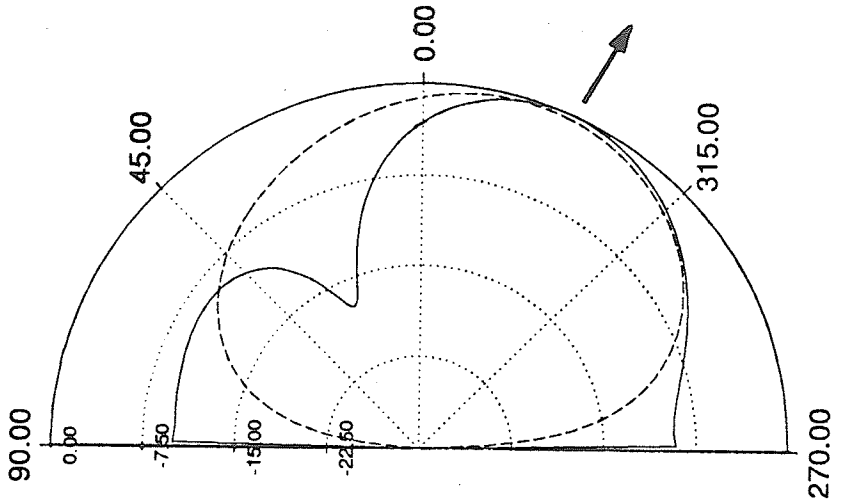

a) Elevation cut, f=3.1 GHz

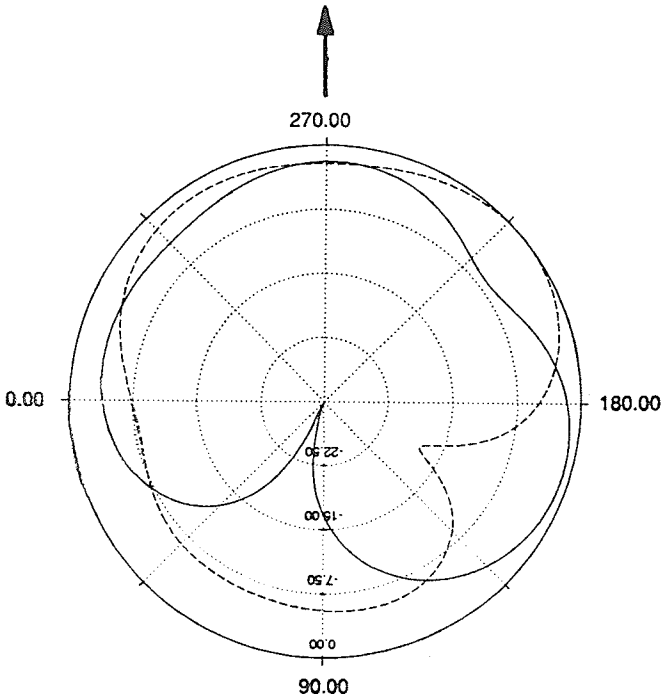

b) Azimuth cut at elevation angle of beam peak, f=3.1 GHz

Figure 5.16:Calculated patterns of active antenna operating Mode 1+Mode 2.—E_θ.- - -E_ϕ.

5.3 Discussion

This chapter has presented some of the applications of the developed active integrated antenna. In application to a receive phased array, it has been shown that the active antenna suffers from an inferior G/T when compared to an array using passive elements, each driven by an amplifier. However, it has also been shown that the active antenna element array is superior to the semi-active array and that using active elements can yield a very compact, single layer array. In addition, because the physical size can easily be varied before fabrication, these elements are amenable to situations where otherwise grating lobes would be a problem.

Pattern reconfiguration/shaping has been investigated and verified experimentally and theoretically. An additional mode of operation has been generated without increasing the circumference of the antenna as required with passive structures. In addition, steering the radiated beam by mode summing was also investigated numerically.

Thus some of the versatility of an active integrated antenna has been demonstrated. As important, the usefulness of the developed design methodology as a design tool has been demonstrated.

CHAPTER 6 : CONCLUSIONS AND RECOMMENDATIONS

6.1 Conclusions

Active integrated antennas have been investigated in this thesis. An active antenna has been defined as a radiating element on which the current distribution along the structure may be altered in a controlled manner. Controlling the current distribution along the antenna is the unique feature of this class of antenna which gives it its primary advantage. This type of radiator includes a control mechanism for antenna performance which is not possible with passive radiators. A literature survey revealed that the majority of work in this field has been confined to resonant type structures and to specific applications which are not suitable for the transmission of communication signals. The structures reported do not permit the alteration of the current distribution along the radiating element itself. In addition, there is no commercially available software package which could be used as a design tool for these type of antennas. This thesis undertook the development of a design tool for an arbitrarily shaped structure and the development of an active integrated antenna which is travelling wave in nature.

The design methodology which was developed is based upon an electromagnetically based circuit simulator which is capable of handling radiation loss and a post-processor. The post-processor was developed to determine the radiation characteristics of the structure analysed by the circuit simulator. A noise model was also developed to determine the output temperature of active integrated antennas which are of the travelling wave type. This was neccessary because in many applications the antenna's G/T is one of the important parameters that need to be known.

The design methodology was successfully applied to the design of active integrated antennas. The developed antenna is travelling wave in nature, thus there is an

associated beam squint with changes in frequency. The predicted radiation characteristics over a frequency band coincided with measured patterns. The calculated and measured results were found to be in good agreement. It was anticipated that the active antenna allows for the correction of the beam squint provided the phase shift due to frequency could be compensated for. This was investigated using the design methodology where the scattering parameters of the devices were altered for this phase correction. The modelled results yielded radiated patterns over a frequency band with virtually no beam squint. The modelling technique was also successfully used to investigate the concepts of multi-mode operation and beam steering by mode summing. In addition, the calculated and measured output temperatures were found to agree to within 10%. Considering the numerous variables involved, this is considered to be an acceptable error.

Thus the developed design methodology and noise model can be considered as effective design tools for passive antennas, active antennas, and circuit design.

The active antenna which was developed and fabricated was studied extensively as a single element and also in application to phased arrays. By altering the current distribution along the structure, variations in peak gain, beam squint, beam shape, i.e. pattern reconfiguration, were noted. Also, altering the device parameters produced beam steering. Thus the developed active antenna falls within the definition given and shows that this antenna has numerous characteristics which are not achievable with passive elements. The results presented indicate that the current distribution along the antenna structure can be altered in a controlled manner. The control mechanisms here are the integrated active devices. It is also concluded that the active antenna suffers from inferior noise temperature performance when compared to passive elements within an array environment. These and other advantages and disadvantages are presented in Table 6.1.

ACTIVE INTEGRATED ANTENNA	
ADVANTAGES	DISADVANTAGES
- compact structure	- variable noise figure, inferior to passive element
- minimizes feed network losses in an array	- complex fabrication
- variable aperture size	- control system could become complex
- variable peak gain	
- ability to reconfigure radiated pattern, i.e. pattern shaping, multi-mode operation	
- ability to correct beam squint	
- ability to steer beam	

Table 6.1 : Advantages and disadvantages of the active integrated antenna.

Thus the class of active integrated antennas developed have been shown to possess numerous unique characteristics unachievable by traditional passive elements. However, some disadvantages have also been identified. The actual implementation of these types of antennas will depend upon whether the advantages out weigh the disadvantages for each application.

The material presented within this thesis has been published in [92]-[99].

6.2 Recommendations

With respect to the active integrated antenna developed and fabricated, further modelling and study is recommended before the multi-mode operation concept could be used in an application. Based upon the developed active antenna, other topologies are recommended for investigation. Some suggested structures are presented in Figure 6.1. The structure in Figure 6.1 e) is of particular interest because three senses of polarization could be achieved with the single structure. That is, depending upon the phase relationship between each radiating section, linear horizontal, linear vertical, or circular polarization could be achieved.

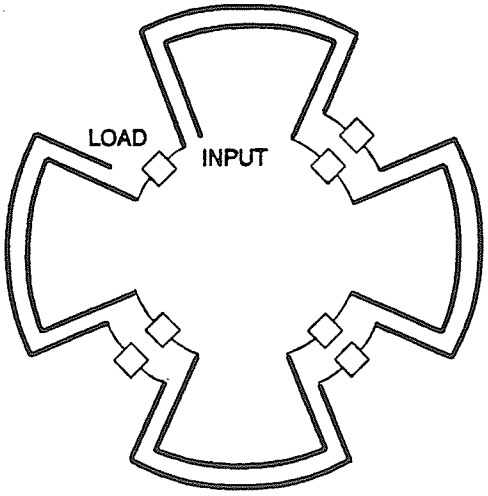

a)

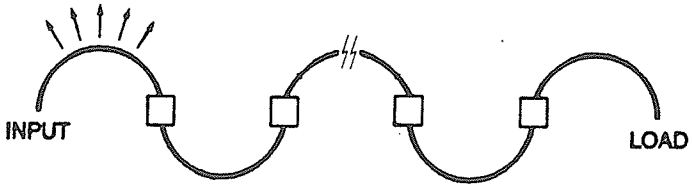

b)

Figure 6.1 : Other active integrated antenna structures based upon the developed antenna.

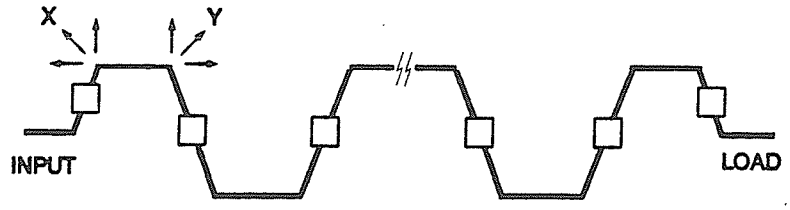

c)

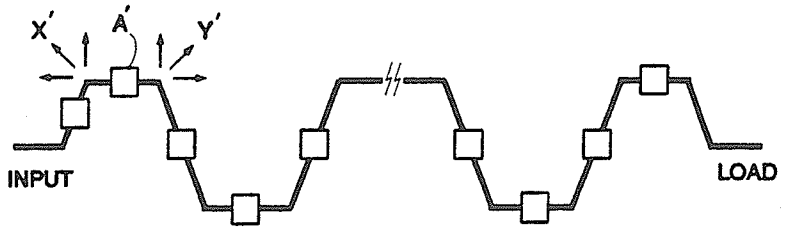

d)

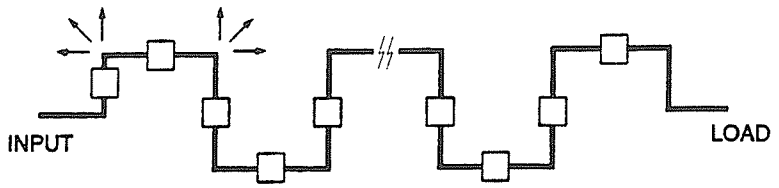

e)

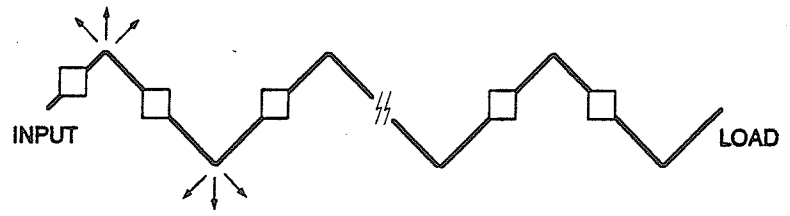

f)

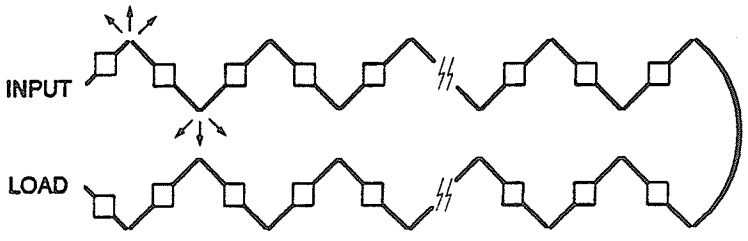

g)

Figure 6.1: (cont.)

Application to EHF is also recommended. With the radiating structures becoming smaller in size due to frequency, designing circuitry to radiate effectively is a preferred option. This is a potential application for the active integrated antenna. Notwithstanding, the developed design methodology could be used to study the radiation characteristics of the circuit layout itself.

Finally, improvements to the developed design tools are recommended. Calculating the gain of the radiating structure by pattern integration is suggested as one improvement to the post-processor. This approach will provide improvement in terms of accuracy. The development of a more rigourous noise model is also recommended. The noise model developed assumes maximum power transfer between each section. Once this condition is violated, the noise model is not valid. Thus a noise model which is not restricted by this condition is desirable.

Appendix I :

Approximate Green's Function for Thick Substrate

The following has been taken directly from [43]. The approximate Green's function in a closed form for a thick microstrip substrate is given below :

$$G_A^{xx} = G_{A0}^{xx} + G_{A,ci}^{xx} + G_{A,sw}^{xx} \tag{aI-1}$$

$$G_q = G_{q0} + G_{q,ci} + G_{q,sw} \tag{aI-2}$$

where $$G_{A0}^{xx} = \frac{\mu_o}{4\pi}\left(\frac{e^{-jk_o r_o}}{r_o} - \frac{e^{-jk_o r_o'}}{r_o'}\right) \tag{aI-3}$$

$$G_{q0} = \frac{1}{4\pi\varepsilon_0}\left(\frac{e^{-jk_o r_o}}{r_o} + K\frac{e^{-jk_o r_o''}}{r_o''} + \sum_{n=1}^{\infty} K^{n-1}(K^2-1)\frac{e^{-jk_o r_n}}{r_n}\right) \tag{aI-4}$$

where $$r_0' = \sqrt{\rho^2 + (z + z' + 2h)^2}$$

$$r_n = \sqrt{\rho^2 + (z + z' + 2nh)^2}$$

$$r_0'' = \sqrt{\rho^2 + (z + z')^2}$$

$$G_{A,ci}^{xx} = \frac{\mu_0}{4\pi}\sum_{i=1}^{N} a_i \frac{e^{-jk_o r_i}}{r_i} \tag{aI-5}$$

$$G_{q,ci} = \frac{1}{4\pi\varepsilon_0}\sum_{i=1}^{N} a_i' \frac{e^{-jk_o r_i'}}{r_i'} \tag{aI-6}$$

where $$r_i = \sqrt{\rho^2 + (z + z' - jb_i)^2}$$

$$r_i' = \sqrt{\rho^2 + (z + z' - jb_i')^2}$$

$$G_{A,sw}^{xx} = \frac{\mu_0}{4\pi}(-2\pi j)\,\mathrm{Res}_1 H_0^{(2)}(k_{\rho p}\rho)k_{\rho p} \tag{aI-7}$$

$$G_{q,sw} = \frac{1}{4\pi\varepsilon_0}(-2\pi j)\,\mathrm{Res}_2 H_0^{(2)}(k_{\rho p}\rho)k_{\rho p} \tag{aI-8}$$

where $$\mathrm{Res}_1 = \sum_{p(TE)} \left[\frac{e^{-jk_{z0}(z+z')}}{j2k_{z0}}\right]_{k_\rho = k_{\rho p}} \lim_{k_\rho \to k_{\rho p}} (k_\rho - k_{\rho p}) R_{TE}$$

$$\mathrm{Res}_2 = \sum_{p(TE,TM)} \left[\frac{e^{-jk_{z0}(z+z')}}{j2k_{z0}}\right]_{k_\rho = k_{\rho p}} \lim_{k_\rho \to k_{\rho p}} (k_\rho - k_{\rho p})\,(R_{TE} + R_q)$$

Appendix II :

Field Components using a Microstrip Green's Function

The following has been taken directly from [48]. The electric field components using Sommerfeld integrals are given below :

$$E_x(x,y,z) = \frac{-j\omega}{k^2}\left\{\int_L I(l')\, k^2 A_x \cos\alpha dl' + \int_L \frac{\partial A}{\partial x}\frac{dI(l')}{dl'}\, dl'\right\} \qquad \text{(aII-1)}$$

$$E_y(x,y,z) = \frac{-j\omega}{k^2}\left\{\int_L I(l')\, k^2 A_x \sin\alpha dl' + \int_L \frac{\partial A}{\partial y}\frac{dI(l')}{dl'}\, dl'\right\} \qquad \text{(aII-2)}$$

$$E_z(x,y,z) = \frac{-j\omega}{k^2}\left\{\int_L A_t \frac{dI(l')}{dl'}\, dl'\right\} \qquad \text{(aII-3)}$$

where $A = A_x + A_z$

$$A_x(\rho) = \frac{\mu}{2\pi}\int_0^\infty \frac{\eta J_0(\eta\rho)}{D_{TE}} e^{-j\zeta z}\, d\eta \qquad \text{(aII-4)}$$

$$A_z(\rho) = \frac{\mu}{2\pi}(\varepsilon_r - 1)\int_0^\infty \frac{-j\zeta\eta J_0(\eta\rho)}{D_{TE}D_{TM}} e^{-j\zeta z}\, d\eta \qquad \text{(aII-5)}$$

$$A_t(\rho) = \frac{\mu}{2\pi}\int_0^\infty \frac{\zeta_e\eta[\zeta_e + j\zeta\tan(\zeta_e h)]J_0(\eta\rho)}{D_{TE}D_{TM}} e^{-j\zeta z}\, d\eta \qquad \text{(aII-6)}$$

$$\rho = \sqrt{(x - x')^2 + (y - y')^2}$$

$$\zeta = \sqrt{k^2 - \eta^2}$$

$$\zeta_e = \sqrt{\varepsilon_r k^2 - \eta^2}$$

The electric far field components are given below :

$$E_\theta = -j\omega P_0(f_1)\{[\cos\phi I_1 + \sin\phi I_2]\cos\theta - F(\theta)I_3\} \quad \text{(aII-7)}$$

$$E_\phi = -j\omega P_0(f_1)[\cos\phi I_2 - \sin\phi I_1] \quad \text{(aII-8)}$$

where $P_0(f_1) = \dfrac{j\mu k\cos\theta}{2\pi D_{TE}(k\sin\theta)}$ (aII-9)

$$F(\theta) = \frac{k\sin\theta\,(\varepsilon_r - 1)}{D_{TM}(k\sin\theta)} \quad \text{(aII-10)}$$

$$I_1 = \sum_{i=1}^{N} I_i\{\cos\alpha_i J_i + \cos\alpha_{i+1} J_{i+1}\} \quad \text{(aII-11)}$$

$$I_2 = \sum_{i=1}^{N} I_i\{\sin\alpha_i J_i + \sin\alpha_{i+1} J_{i+1}\} \quad \text{(aII-12)}$$

$$I_3 = \sum_{i=1}^{N} I_i\{K_i + K_{i+1}\} \quad \text{(aII-13)}$$

where $J_i = \dfrac{H_i}{H_i^2 + k^2}\left\{[1 - \dfrac{k}{H_i}\cot kd_i]\,W_{i+1} + \dfrac{k}{H_i \sin kd_i}W_i\right\}$ (aII-14)

$$J_{i+1} = \frac{-H_{i+1}}{H_{i+1}^2 + k^2}\left\{[1 + \frac{k}{H_{i+1}}\cot kd_{i+1}]\,W_{i+1} - \frac{k}{H_{i+1}\sin kd_{i+1}}W_{i+2}\right\} \quad \text{(aII-15)}$$

$$K_i = \frac{H_i}{H_i^2 + k^2}\left\{[\cot kd_{i+1} + \frac{k}{H_i}]\,W_{i+1} - \frac{1}{\sin kd_i}W_i\right\} \quad \text{(aII-16)}$$

$$K_{i+1} = \frac{-H_{i+1}}{H_{i+1}^2 + k^2}\left\{[\frac{k}{H_{i+1}} - \cot kd_{i+1}]\,W_{i+1} + \frac{1}{\sin kd_{i+1}}W_{i+2}\right\} \quad \text{(aII-17)}$$

$$H_i = jk\sin\theta\cos(\phi - \alpha_i) \quad \text{(aII-18)}$$

$$W_i = e^{jk\rho_i\sin\theta\cos(\phi - \phi_i)} \quad \text{(aII-19)}$$

$$D_{TE} = jk\cos\theta + k\sqrt{\varepsilon_r - \sin^2\theta}\,\cot(kh\sqrt{\varepsilon_r - \sin^2\theta}) \qquad \text{(aII-20)}$$

$$D_{TM} = j\varepsilon_r k\cos\theta - k\sqrt{\varepsilon_r - \sin^2\theta}\,\tan(kh\sqrt{\varepsilon_r - \sin^2\theta}) \qquad \text{(aII-21)}$$

Appendix III :

Computer Code for Calculating Radiation Characteristics

The following is the source code for the program used as the post processor to the circuit simulator :

```
c
c  Calculation of far field from current distribution
c  of a printed line. Green's function for a microstrip
c  printed transmission line is implemented.
c
c
c  Variable Library
c
c  knt - free space wave number
c  n   - number of nodes (segments)~
c  x,y,z,angle - coordinates and orientation angle of segment
c  Re,Imag - real and imaginary components for Ax,Ay, Atheta,Aphi
c            Etheta,Ephi
c
c
      integer n,i,theta,fi,thetmax1,thetmax2
      real ReET(361,2),ImagET(361,2),ReEP(361,2),th,ph,temp1,phi
      real ETMAG(361,2),EPMAG(361,2),Radint(361,2),radmax,thet
      real ImagEP(361,2),f,c,d(350),phip(350),ETphs(361,2),temp2
      real x(350),y(350),z(350),alpha(350),rowp(350),xx,yy,hh,aangle
      real pi,u,eps,lam,knt,k,nn,len,wid,epsr,w,EPphs(361,2)
      real Imag(350),Iphs(350),Ireal,Iimag,arg,arg1,arg2,eta,sig,sige
      real gain(361,2),gainET(361,2),gainEP(361,2)
      character geometry*20,current*20
      complex DTE,DTM,PP(361),FF(361),H(350),JI,JI1,KKI,KKI1
      complex I1,I2,I3,so
      complex Etheta(361,2),Ephi(361,2),Itot(350),Itotp(350)
      real ETHT,EPHY,abet,abep,Etot,normz,S11mag,S11phs,curin,Rin
      complex Eco(361,2),Ecross(361,2),S11,znorm,Zin
      double precision*16 Ir,Im
c
c  Initialize Variables
c
      c=3.0E08
      pi=3.141592654
      u=4.0*pi*1.0E-07
      eps=8.85E-12
      write (6,*) 'Enter frequency (GHz) : '
      read (5,*) f
      write (6,*) 'Enter relative dielectric constant : '
      read (5,*) epsr
c
c Read Geometry
c
      write (6,*) 'Enter geometry file (units=meter) : '
      read (5,*) geometry
      write (6,*) 'Enter structure height above gnd (m) : '
      read (5,*) hh
      write (6,*) 'Enter number of segments : '
      read (5,*) n
      f=f*1.0E09
      w=2.0*pi*f
      lam=c/f
      knt=2.0*pi/lam
      k=knt
      open (10, file=geometry)
c
c read set-up for emsim file, note: y  and x
c coordinates reversed
c
      do 20 i=1,n
         read (10,*) nn,xx,yy,len,wid,aangle
          x(i)=yy
          y(i)=xx
          z(i)=hh
c
c must 90 degrees to convert EMsim angle to standard
c notation
c
          aangle=-1.0*aangle
         alpha(i)=aangle+90.0
         alpha(i)=(alpha(i)/360.0)*2.0*pi
         d(i)=len
```

```
            write (29,*) i,x(i),y(i)
            if (i.eq.n) then
               alpha(i+1)=alpha(i)
            end if
 20      continue
         do 21 i=1,n
         if (i.eq.n) then
            x(i+1)=x(i)+len/2.0*cos(alpha(i))
            y(i+1)=y(i)+len/2.0*sin(alpha(i))
            rowp(i+1)=sqrt(x(i+1)*x(i+1)+y(i+1)*y(i+1))
            phip(i+1)=atan2(y(i),x(i))
            x(i)=x(i)-len/2.0*cos(alpha(i))
            y(i)=y(i)-len/2.0*sin(alpha(i))
            rowp(i)=sqrt(x(i)*x(i)+y(i)*y(i))
            phip(i)=phip(i+1)
         else
            x(i)=x(i)-len/2.0*cos(alpha(i))
            y(i)=y(i)-len/2.0*sin(alpha(i))
            rowp(i)=sqrt(x(i)*x(i)+y(i)*y(i))
            if (x(i).eq.0.0) then
            phip(i)=0.0
            else
            phip(i)=atan2(y(i),x(i))
            end if
         end if
 21      continue
         do 99 i=1,n+1
            write (31,*) i,x(i),y(i),alpha(i),phip(i),rowp(i)
 99      continue
         close(10)
c
c  Read current distribution
c   ( specific for emsim file )
c
         write (6,*) 'Enter current file : '
         read (5,*) current
         open (11,file=current)
         do 25 i=1,n
            read (11,100) Ir,Im
 100        format (17x,D24.4,1x,D24.4)
            write (123,*) Ir,Im
            Ireal=Ir
            Iimag=Im
            Imag(i)=sqrt(Ireal*Ireal+Iimag*Iimag)
            Iphs(i)=(atan(Iimag/Ireal))*360.0/(2.0*pi)
            Itot(i)=cmplx(Ireal,Iimag)
            Itotp(1)=Itot(1)
c            write (33,*) i,Imag(i),Iphs(i)
c            write (34,*) i,Ireal,Iimag
 25      continue
         close (11)
         do 26 i=2,n
            if (i.eq.n) then
               Itotp(i+1)=Itot(i)
            end if
            Itotp(i)=(Itot(i-1)+Itot(i))/2.0
 26      continue
         do 27 i=1,n+1
            Imag(i)=sqrt(REAL(Itotp(i))*REAL(Itotp(i))+AIMAG(Itotp(i))*
     &AIMAG(Itotp(i)))
            Iphs(i)=(atan(AIMAG(Itotp(i))/REAL(Itotp(i))))*360.0/(2.0*pi)
            write (33,*) i,Imag(i),Iphs(i)
            write (34,*) i,Itotp(i),rowp(i),phip(i)
 27      continue
c        ,
c-----------------------------------------------------------------------
c
c Read information required for gain calculation
c
         write (6,*) 'Enter input current (magnitude) :'
         read (5,*) curin
         write (6,*) 'Enter S11 (real part) :'
         read (5,*) S11mag
```

```
      write (6,*) 'Enter S11 (imag part) :'
      read (5,*) S11phs
      write (6,*) 'Enter normalizing impedance :'
      read (5,*) normz
c
c Calculate input impedance
c
      S11=cmplx(S11mag,S11phs)
      znorm=(1+S11)/(1-S11)
      Zin=znorm*normz
      Rin=REAL(Zin)
c
c-----------------------------------------------------------------------
c
c  Calculate Far-Field Components
c
       so=cmplx(0.0,1.0)
      do 30 theta=2,361
         thet=float(theta)
         th=((thet-1.0)/360.0)*2.0*pi
         temp2=sqrt(epsr-sin(th)*sin(th))
         DTE=cmplx(k*sqrt(epsr-sin(th)*sin(th))/
     &tan(k*hh*sqrt(epsr-sin(th)*sin(th))),k*cos(th))
         DTM=cmplx(-1.0*k*sqrt(epsr-sin(th)*sin(th))*
     &tan(k*hh*sqrt(epsr-sin(th)*sin(th))),epsr*k*cos(th))
         temp1=2.0*k*cos(th)/DTE
         PP(theta)=so*temp1
         FF(theta)=(epsr-1.0)/(k*sin(th)*DTM)
         do 35 fi=1,2
            if (fi.eq.1) then
               phi=0.0
            else
               phi=90.0
            end if
             if ((thet.ge.91).and.(thet.le.271)) then
                PP(theta)=cmplx(0.0,0.0)
                FF(theta)=cmplx(0.0,0.0)
                ETmag(theta,fi)=0.0
                ETphs(theta,fi)=0.0
                EPmag(theta,fi)=0.0
                EPphs(theta,fi)=0.0
                go to 35
             end if
            ph=(phi/360.0)*2.0*pi
            I1=cmplx(0.0,0.0)
            I2=cmplx(0.0,0.0)
            I3=cmplx(0.0,0.0)
            do 40 i=1,n-1
            H(i)=cmplx(0.0,k*sin(th)*cos(ph-alpha(i)))
            H(i+1)=cmplx(0.0,k*sin(th)*cos(ph-alpha(i+1)))
            arg=k*rowp(i)*sin(th)*cos(ph-phip(i))
            arg1=k*rowp(i+1)*sin(th)*cos(ph-phip(i+1))
            arg2=k*rowp(i+2)*sin(th)*cos(ph-phip(i+2))
            JI=1.0/(H(i)*H(i)+k*k)*((H(i)-k/tan(k*d(i)))*
     &(cos(arg1)+so*sin(arg1))+k/sin(k*d(i))*
     &(cos(arg)+so*sin(arg)))
            JI1=-1.0/(H(i+1)*H(i+1)+k*k)*((H(i+1)+
     &k/tan(k*d(i+1)))*(cos(arg1)+so*sin(arg1))-k/sin(k*d(i+1))*
     &(cos(arg2)+so*sin(arg2)))
            KKI=1.0/(H(i)*H(i)+k*k)*((H(i)/tan(k*d(i))+k)*
     &(cos(arg1)+so*sin(arg1))-H(i)/sin(k*d(i))*
     &(cos(arg)+so*sin(arg)))
            KKI1=-1.0/(H(i+1)*H(i+1)+k*k)*((k-H(i+1)/
     &tan(k*d(i+1)))*(cos(arg1)+so*sin(arg1))+H(i+1)/sin(k*d(i+1))*
     &(cos(arg2)+so*sin(arg2)))
            I1=I1+Itotp(i+1)*(cos(alpha(i))*JI+
     &cos(alpha(i+1))*JI1)
            I2=I2+Itotp(i+1)*(sin(alpha(i))*JI+
     &sin(alpha(i+1))*JI1)
            I3=I3+Itotp(i+1)*(KKI+KKI1)
c           write (444,*) Itotp(i),rowp(i),phip(i)
 40         continue
         Etheta(theta,fi)=-2.0*pi*f*1.0E-7*PP(theta)*so*
```

```
     &(cos(th)*(cos(ph)*I1+sin(ph)*I2)-FF(theta)*I3)
          Ephi(theta,fi)=-2.0*pi*f*1.0E-7*PP(theta)*so*
     &(cos(ph)*I2-sin(ph)*I1)
          Eco(theta,fi)=Etheta(theta,fi)*cos(ph)+Ephi(theta,fi)
     &*sin(ph)
          Ecross(theta,fi)=Etheta(theta,fi)*sin(ph)-Ephi(theta,fi)
     &*cos(ph)
          write (7,*) theta,DTM,DTE,PP(theta),FF(theta),I3
          ReET(theta,fi)=REAL(Etheta(theta,fi))
          ImagET(theta,fi)=AIMAG(Etheta(theta,fi))
          ETmag(theta,fi)=sqrt(ReET(theta,fi)*ReET(theta,fi)+
     &ImagET(theta,fi)*ImagET(theta,fi))
          ETphs(theta,fi)=atan(ImagET(theta,fi)/ReET(theta,fi))
          ReEP(theta,fi)=REAL(Ephi(theta,fi))
          ImagEP(theta,fi)=AIMAG(Ephi(theta,fi))
          EPmag(theta,fi)=sqrt(ReEP(theta,fi)*ReEP(theta,fi)+
     &ImagEP(theta,fi)*ImagEP(theta,fi))
          EPphs(theta,fi)=atan(ImagEP(theta,fi)/ReEP(theta,fi))
c
c Radians -> Degrees
c
          ETphs(theta,fi)=(ETphs(theta,fi)*360.0)/(2.0*pi)
          EPphs(theta,fi)=(EPphs(theta,fi)*360.0)/(2.0*pi)
           gainET(theta,fi)=10.0*log10(ETmag(theta,fi)*ETmag(theta,fi)
     &/(30.0*curin*curin*Rin))
           gainEP(theta,fi)=10.0*log10(EPmag(theta,fi)*EPmag(theta,fi)
     &/(30.0*curin*curin*Rin))
           gain(theta,fi)=10.0*log10((ETmag(theta,fi)*ETmag(theta,fi)+
     &EPmag(theta,fi)*EPmag(theta,fi))/(30.0*curin*curin*Rin))
 35       continue
             write (777,*) theta,th,KKI,KKI1,I3,PP(theta),FF(theta)
             write (778,*) FF(theta)
 30    continue
c
c Determine max for normalization
c
       do 55 theta=2,361
          thet=theta
          do 60 fi=1,2
             radint(theta,fi)=sqrt(ETmag(theta,fi)*ETmag(theta,fi)+
     &EPmag(theta,fi)*EPmag(theta,fi))
             if (radint(theta,fi).gt.radmax) then
                radmax=radint(theta,fi)
                if (fi.eq.1) then
                thetmax1=theta
                else
                 thetmax2=theta
                end if
             end if
 60       continue
 55    continue
       Etot=cabs(Eco(357,2))*cabs(Eco(357,2))+
     &cabs(Ecross(357,2))*cabs(Ecross(357,2))
       do 37 theta=2,361
        do 38 fi=1,2
         abet=cabs(Eco(theta,fi))
         if (abet.eq.0.0) then
           ETHT=-100.0
         else
         ETHT=10.0*log10(abet*abet/Etot)
         end if
         abep=cabs(Ecross(theta,fi))
         if (abep.eq.0.0) then
          EPHY=-100.0
         else
         EPHY=10.0*log10(abep*abep/Etot)
         end if
         if (fi.eq.1) then
           write(11,*) theta,ETHT,EPHY
          else
           write(22,*) theta,ETHT,EPHY
         end if
 38     continue
```

```
 37   continue
c
c Output field data for phi=0, phi=90 cut
c and 3-d pattern ,
c file 1,2,3 normalized to maximum field point
c
c file 8&9 are normalized to max point within
c that particular cut (phi=0 and phi=90)
c
       do 72 theta=2,361
          write (1,*) theta,ETmag(theta,1),ETphs(theta,1),
     &EPmag(theta,1),EPphs(theta,1)
          write (2,*) theta,ETmag(theta,2),ETphs(theta,2),
     &EPmag(theta,2),EPphs(theta,2)
          write (3,*) gainET(theta,1),gainEP(theta,1),
     &gain(theta,1)
          write (4,*) gainET(theta,2),gainEP(theta,2),
     &gain(theta,2)
 72    continue
       write (779,*) thetmax1,thetmax2
       stop
       end
```

Appendix IV :

Data Sheet for MMIC Amplifier

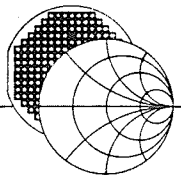

PACIFIC MONOLITHICS
GALLIUM ARSENIDE SYSTEMS

DATA SHEET

MODEL PM-AP0602

2-6 GHz MEDIUM-POWER MMIC AMPLIFIERS

FEATURES

0.25W OUTPUT POWER
10 dB GAIN
ON-CHIP GAIN CONTROL
SINGLE SUPPLY VOLTAGE
SMALL SIZE

Pacific Monolithics medium-power amplifier chips are small, highly reliable and operate well within the thermal limits currently accepted as industry standards. Applied in cascades, both as drivers and output stages, these MMICs provide good VSWR and flat broadband gain across the entire 2-6 GHz band. Class A operation at 1/2 I_{DSS} operation provides good linearity and intermod performance up to the 1-dB gain compression point. The PM-AP0602 also features a single supply voltage and on-chip gain control.

MIL-STD 883 screening available

PERFORMANCE SPECIFICATIONS

PARAMETER	MIN	TYP	MAX	UNITS
Small Signal Gain	9	10		dB
Gain Flatness		±1.0	± 1.5	dB
Input VSWR		2.0:1	2.2:1	
Output VSWR		2.0:1		
Power Output (1-dB compression)	23	24		dBm
Noise Figure*			10	dB
Gain Control On/Off Ratio		30		dB
Gain Control Voltage		+1 to -5		Vdc
Harmonics at 1-dB Compression	-10	-15		dBc
Third-Order Intercept Point		33		dBm
Bias Voltage		8	9	Vdc
Current*	190	220	250	mA
Operating Temperature	-54		+125	^{o}C
Thermal resistance		23		^{o}C/W

*Biased for maximum power
Specifications measured at 25^{o}C

245 Santa Ana Court, Sunnyvale, CA 94086 • TWX 510-600-3726 • (408) 732-8000

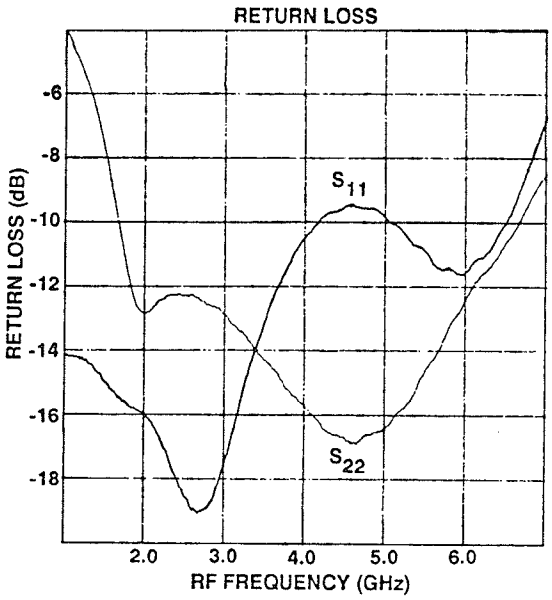
RETURN LOSS
RETURN LOSS (dB)
-6
-8
-10
-12
-14
-16
-18
S_{11}
S_{22}
2.0
3.0
4.0
5.0
6.0
RF FREQUENCY (GHz)

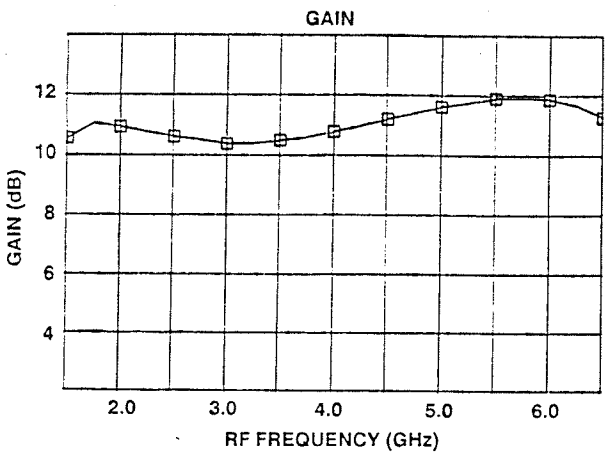
GAIN
GAIN (dB)
12
10
8
6
4
2.0
3.0
4.0
5.0
6.0
RF FREQUENCY (GHz)

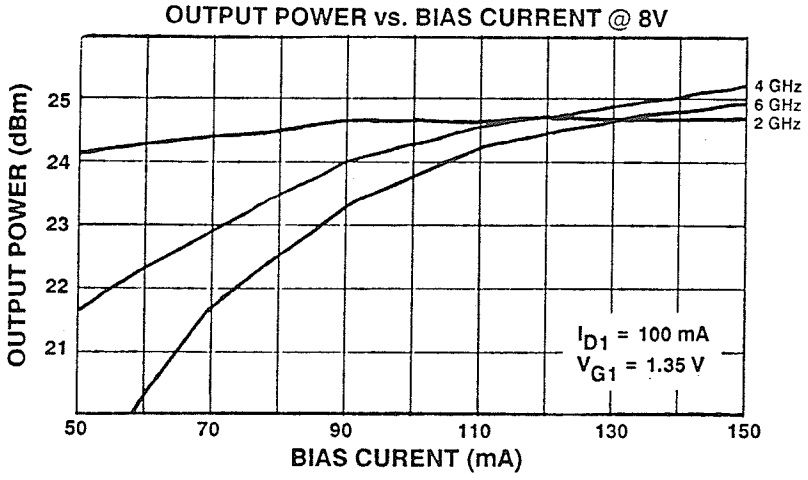
OUTPUT POWER vs. BIAS CURRENT @ 8V
OUTPUT POWER (dBm)
25
24
23
22
21
4 GHz
6 GHz
2 GHz
I_{D1} = 100 mA
V_{G1} = 1.35 V
50
70
90
110
130
150
BIAS CURENT (mA)

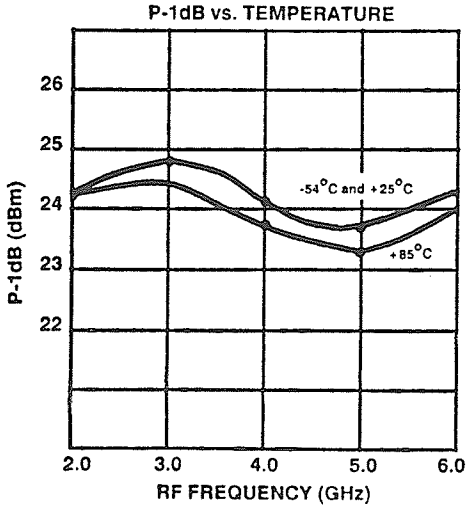
P-1dB vs. TEMPERATURE
P-1dB (dBm)
26
25
24
23
22
-54°C and +25°C
+85°C
2.0
3.0
4.0
5.0
6.0
RF FREQUENCY (GHz)

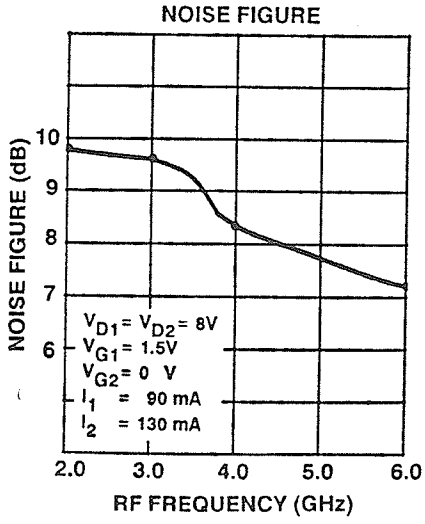
NOISE FIGURE
NOISE FIGURE (dB)
10
9
8
7
6
V_{D1} = V_{D2} = 8V
V_{G1} = 1.5V
V_{G2} = 0 V
I_1 = 90 mA
I_2 = 130 mA
2.0
3.0
4.0
5.0
6.0
RF FREQUENCY (GHz)

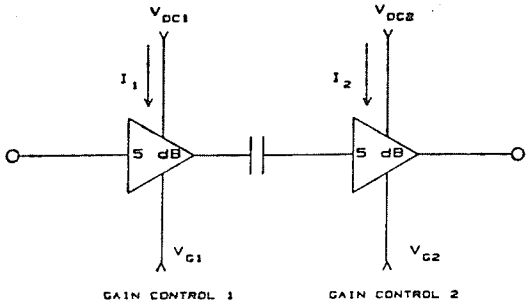

NOTE: Neither output nor input is AC coupled.

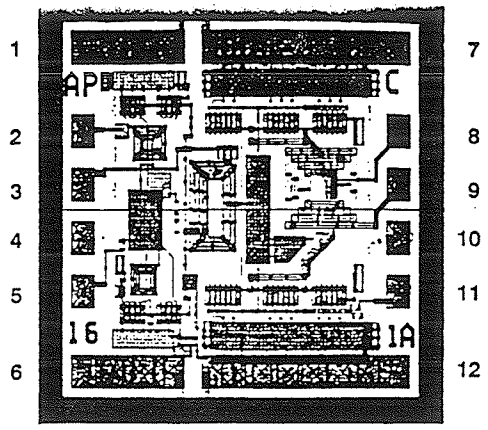

I_1 = 90 mA $\quad V_{G1} \simeq +1.5\,V^*$
I_2 = 130 mA $\quad V_{G2} \simeq 0\ V$

1. GND
2. RF IN
3. V_{DC1}
4. N/C
5. V_{G1}
6. GND
7. GND
8. RF OUT
9. V_{DC2}
10. N/C
11. V_{G2}
12. GND

* For optimum performance, I_1 and I_2 can be set using control voltage to V_{G1} and V_{G2}. Once the desired values of V_{G1} and V_{G2} have been measured, a single resistor from V_{DC1} and V_{DC2} can be used to set the voltages on pads 5 (VG_1) and 11 (VG_2). The DC resistance to ground at pads 5 and 11 is typically 6K Ohms.

ASSEMBLY DIAGRAM

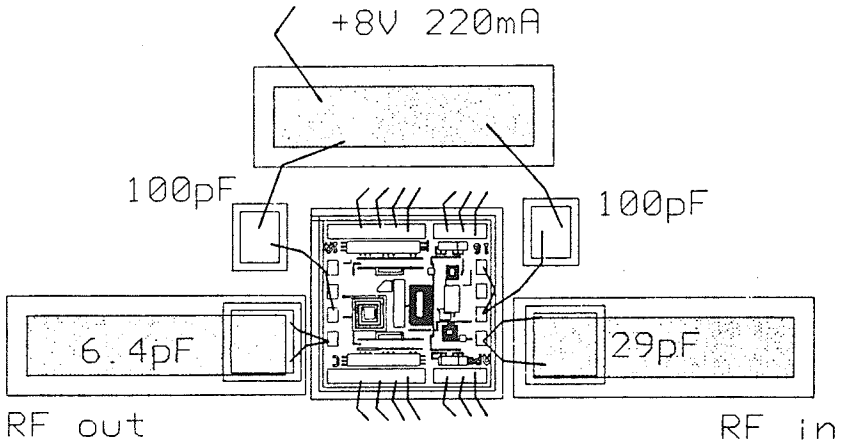

S-PARAMETERS

Frequency	S_{11}	S_{21}	S_{12}	S_{22}
1.50 GHz	0.160 106.11	1.932 90.02	0.002 -165.52	0.423 -165.30
2.00 GHz	0.168 83.68	3.471 19.84	0.005 138.99	0.254 -169.85
2.50 GHz	0.165 52.06	3.500 -27.79	0.007 114.98	0.277 -172.87
3.00 GHz	0.158 10.45	3.477 -62.05	0.006 96.78	0.258 -177.53
3.50 GHz	0.185 - 38.77	3.646 - 92.45	0.006 107.76	0.211 -176.00
4.00 GHz	0.243 - 78.23	3.797 -121.39	0.006 95.26	0.169 -1167.61
4.50 GHz	0.309 -111.40	4.040 -150.94	0.006 101.55	0.138 -153.34
5.00 GHz	0.348 -140.06	4.198 178.58	0.006 97.06	0.133 -136.55
5.50 GHz	0.344 -169.60	4.389 146.57	0.007 97.43	0.155 -125.74
6.00 GHz	0.287 153.79	4.509 111.91	0.006 92.16	0.190 -120.07
6.50 GHz	0.274 103.54	4.507 73.45	0.008 86.92	0.250 -121.85

Handling, Assembly and Storage Recommendations For Pacific Monolithics GaAs MMIC Die

General

The same precautions which apply to discrete GaAs microwave FETs should be observed for GaAs MMICs

Normal ESD protection measures must be observed.

No voltages which exceed the maxima recommended in the device data sheet should ever be applied, even instantaneously. All assembly and test equipment must be constructed to observe this very important precaution.

Assembly

These devices are supplied with backside metalization for eutectic die attachment. They can also be attached using a thin layer of epoxy, with an increase in thermal resistance of approximately $1^{O}C/W$. For optimum performance, the device should be mounted on a carrier with reasonable thermal conductivity (3.9 W/cm ^{O}C), such as copper-tungsten. Kovar can be substituted, but the nominal gain decreases by 1.5 dB.

Thermosonic wedge or ball bonding wire up to 1.3 mil in diameter has been used successfully on GaAs MMICs with epoxy die attach. The same equipment and bonding parameters used on discrete GaAs microwave FETs will generally provide reliable bonds to GaAs MMICs. For epoxy die-attached devices, thermosonic bonding will ordinarily be required to keep the stage temperature below the glass transition temperature of the epoxy. High-purity gold wire with 2-5 percent elongation and 1-mil (25 microns) or smaller diameter is recommended.

Long-Term Storage

Pacific Monolithics' GaAs MMICs are fabricated with a high-integrity, gold-based metalization system, and are glassivated for further environmental protection. No shelf-life problems have been observed, provided that the maximum passive storage temperature is not exceeded and the devices are stored in ordinary clean-room conditions. The customer may wish to store them in a desiccator purged with clean, dry nitrogen as added protection.

Absolute Maximum Ratings

V_{DC}	10 V
I_1	120 mA
I_2	160 mA
V_{GAIN} max	+2 V
V_{GAIN} min	-5 V

890602

PACIFIC MONOLITHICS
245 Santa Ana Court, Sunnyvale, CA 94086 • TWX 510-600-3726 • (408) 732-8000

Appendix V :

Noise Temperature Measurement Procedure

A "Y-factor" approach is used where two output noise powers are required to determine the antenna temperature. The Y-factor is the ratio of output noise powers due to two different input noise temperatures [82]. The block diagram is given in Figure AV-1.

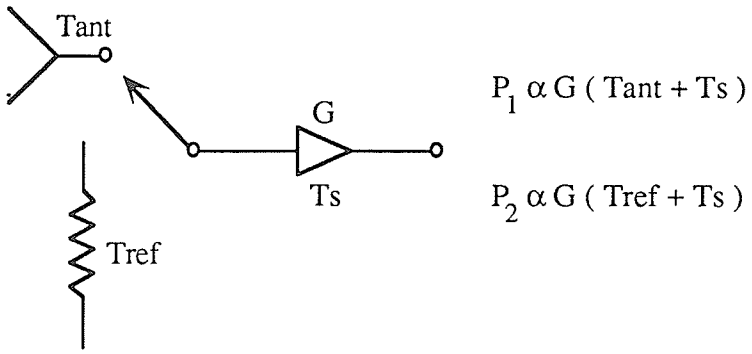

Figure AV-1 : Block diagram of noise temperature measurement.

$$\therefore \frac{P_1}{P_2} = \frac{G(T_{ant}+T_S)}{G(T_{ref}+T_S)} \qquad (1)$$

To control the environment temperature of the antenna, the antenna is placed in a shielded box lined with black absorber. The temperature within the chamber is monitored to ensure a uniform temperature, T_{cham}. Under these conditions, the walls should emit a constant radiation brightness as discussed in [83]. The chamber is constructed such that the antenna is not loaded. This has been verified by measuring the return loss parameter of the antenna in and out of the chamber. Minimal variation was observed as shown for a passive antenna as well as the active antenna (Figure 4.21). The measurement equipment set-up for Figure AV-1 is given in Figure AV-2.

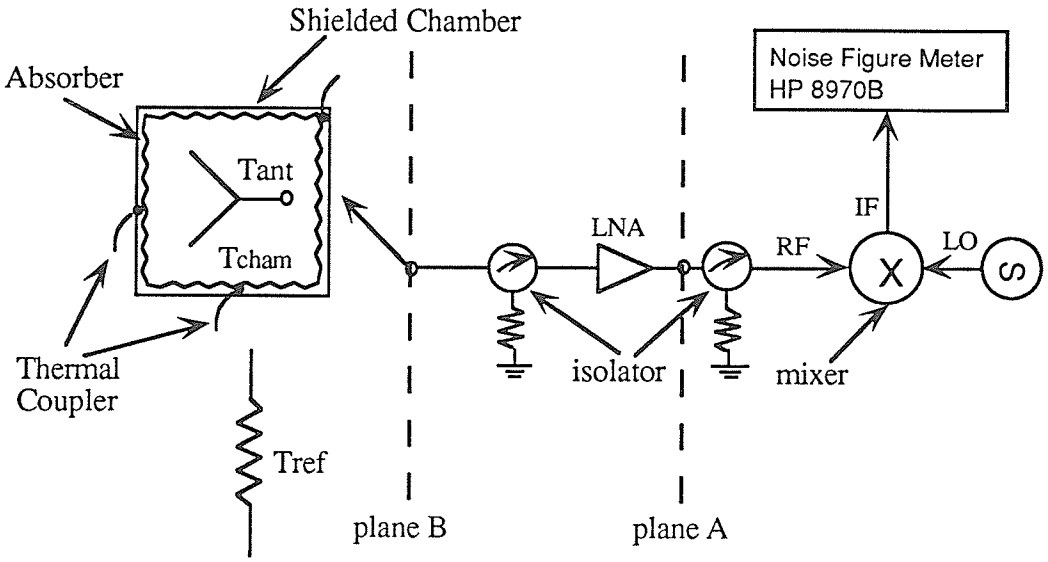

Figure AV-2 : Experimental set-up for antenna noise measurement.

The measurement procedure is presented below :

1. Calibrate at plane A
2. Measure noise temp. at plane B to determine T_s.
3. Connect reference (noise source) at plane B to measure noise power with source either on (special fcn. 9.2) or off (special fcn. 9.1). This will be used for P_2 in eq'n (1).
4. Connect antenna to plane B and measure output power. This will be P_1 in eq'n (1).
5. Input the known parameters into eq'n (1) and calculate the unknown parameter, T_{ant}.

Appendix VI :

Computer Code for Array Simulations

```
c
c
c This program applies pattern multiplication to
c calculate the pattern of a phased array using
c loop-based travelling wave antennas.
c Array grid is rectangular.
c
c  Variable Library
c
c a - loop radius (m)
c Nx - # of elments in pos. x-direction
c Ny - # of elements in pos. y-direction
c thnot, phnot - direction of beam pointing
c k - wave number
c f - centre frequency, f=1.7025 GHz
c dx,dy - centre to centre separation distance (m)
c
c
c
      integer Nx,Ny,n,m,theta,phi
      real th,ph,a,k,thnot,phnot,f,w,dx,dy,u,c,b,d
      real ETmag(181,361),EPmag(181,361),Radint(181,361),pi,lam
      real alphax,alphay,ReSx,ImSx,ReSy,ImSy,sum,dir
      real Refth,Imfth,Refph,Imfph,Imo,Ion,radmax,nrad
      real bessj0,bessj
      complex Sx(181,361),Sy(181,361),fth(181,361),fph(181,361)
      complex Eth(181,361),Eph(181,361)
c
c Intialize Variables
c
      Nx=5
      Ny=5
      thnot=0.0
      phnot=90.0
      Imo=1.0
      Ion=1.0
      f=1.7025E09
      c=3.0E08
      pi=3.141592654
      u=4.0*pi*1.0E-07
      lam=c/f
      a=0.71*lam
      dx=2*a+0.05*lam
      dy=2*a+0.05*lam
      w=2.0*pi*f
      k=2.0*pi/lam
      radmax=0.0
c
c theta cut at phinot
c
      phi=int(phnot)+1
      ph=(phnot/360)*2.0*pi
      phnot=ph
      thnot=(thnot/360.0)*2.0*pi
      do 10 theta=-90,90
        th=(theta/360.0)*2.0*pi
        theta=theta+91
c
c Calculate Array Factor
c
        ReSx=0.0
        ImSx=0.0
        ReSy=0.0
        ImSy=0.0
        do 20 m=1,Nx
          alphax=-1.0*k*dx*sin(thnot)*cos(phnot)
          ReSx=ReSx+Imo*cos((m-1)*(k*dx*sin(th)*cos(ph)+alphax))
          ImSx=ImSx+Imo*sin((m-1)*(k*dx*sin(th)*cos(ph)+alphax))
20      continue
        Sx(theta,phi)=cmplx(ReSx,ImSx)
        do 30 n=1,Ny
          alphay=-1.0*k*dy*sin(thnot)*sin(phnot)
          ReSy=ReSy+Ion*cos((n-1)*(k*dy*sin(th)*sin(ph)+alphay))
```

```
          ImSy=ImSy+Ion*sin((n-1)*(k*dy*sin(th)*sin(ph)+alphay))
 30     continue
        Sy(theta,phi)=cmplx(ReSy,ImSy)
c
c Calculate Element Pattern
c
c
c theta component
c
        b=((-1.0*w*u*a)/4.0)*cos(th)*(bessj(2,k*a*sin(th))
     &+bessj0(k*a*sin(th)))
        Refth=b*-1.0*sin(ph-pi/2.0)
        Imfth=b*cos(ph-pi/2.0)
        fth(theta,phi)=cmplx(Refth,Imfth)
c
c phi component
c
        d=((-1.0*w*u*a)/4.0)*(bessj(2,k*a*sin(th))
     &+bessj0(k*a*sin(th)))
        Refph=d*-1.0*sin(ph)
        Imfph=d*cos(ph)
        fph(theta,phi)=cmplx(Refph,Imfph)
c
c Pattern Multiplication
c
        Eth(theta,phi)=fth(theta,phi)*Sx(theta,phi)*Sy(theta,phi)
        Eph(theta,phi)=fph(theta,phi)*Sx(theta,phi)*Sy(theta,phi)
        ETmag(theta,phi)=sqrt((REAL(Eth(theta,phi)))**2
     &+(AIMAG(Eth(theta,phi)))**2)
        EPmag(theta,phi)=sqrt((REAL(Eph(theta,phi)))**2
     &+(AIMAG(Eph(theta,phi)))**2)
c
c Radiation Intensity
c
        Radint(theta,phi)=sqrt(ETmag(theta,phi)**2
     &+EPmag(theta,phi)**2)
        if (radint(theta,phi).gt.radmax) then
          radmax=radint(theta,phi)
        end if
c       ETmag(theta,phi)=20*log10(ETmag(theta,phi)/1)+0
c       EPmag(theta,phi)=20*log10(EPmag(theta,phi)/1)+0
        write (1,*) theta,ETmag(theta,phi),EPmag(theta,phi),
     &Radint(theta,phi)
     theta=theta-91
 10   continue
c
c Calculate directivity
c
     sum=0.0
     do 33 theta=1,91
       th=(((theta-91)*-1.0)/360.0)*2.0*pi
       nrad=Radint(theta,phi)/radmax
       sum=sum+nrad*sin(th)
 33   continue
     dir=20*log10(4*pi/(2*pi*(pi/90)*sum))
     write (3,*) dir
c
c phi cut at thetanot
c
     thnot=(thnot/(2.0*pi))*360.0
     theta=int(thnot)+1
     th=(thnot/360)*2.0*pi
     thnot=th
     do 40 phi=1,360
       ph=(phi/360.0)*2.0*pi
c
c Calculate Array Factor
c
       ReSx=0.0
       ImSx=0.0
       ReSy=0.0
       ImSy=0.0
       do 50 m=1,Nx
```

```
          alphax=-1.0*k*dx*sin(thnot)*cos(phnot)
          ReSx=ReSx+Imo*cos((m-1)*(k*dx*sin(th)*cos(ph)+alphax))
          ImSx=ImSx+Imo*sin((m-1)*(k*dx*sin(th)*cos(ph)+alphax))
 50     continue
        Sx(theta,phi)=cmplx(ReSx,ImSx)
        do 60 n=1,Ny
          alphay=-1.0*k*dy*sin(thnot)*sin(phnot)
          ReSy=ReSy+Ion*cos((n-1)*(k*dy*sin(th)*sin(ph)+alphay))
          ImSy=ImSy+Ion*sin((n-1)*(k*dy*sin(th)*sin(ph)+alphay))
 60     continue
        Sy(theta,phi)=cmplx(ReSy,ImSy)
c
c Calculate Element Pattern
c
c
c theta component
c
        b=((-1.0*w*u*a)/4.0)*cos(th)*(bessj(2,k*a*sin(th))
     &+bessj0(k*a*sin(th)))
        Refth=b*-1.0*sin(ph-pi/2.0)
        Imfth=b*cos(ph-pi/2.0)
        fth(theta,phi)=cmplx(Refth,Imfth)
c
c phi component
c
        d=((-1.0*w*u*a)/4.0)*(bessj(2,k*a*sin(th))
     &+bessj0(k*a*sin(th)))
        Refph=d*-1.0*sin(ph)
        Imfph=d*cos(ph)
        fph(theta,phi)=cmplx(Refph,Imfph)
c
c Pattern Multiplication
c
        Eth(theta,phi)=fth(theta,phi)*Sx(theta,phi)*Sy(theta,phi)
        Eph(theta,phi)=fph(theta,phi)*Sx(theta,phi)*Sy(theta,phi)
        ETmag(theta,phi)=sqrt((REAL(Eth(theta,phi)))**2
     &+(AIMAG(Eth(theta,phi)))**2)
        EPmag(theta,phi)=sqrt((REAL(Eph(theta,phi)))**2
     &+(AIMAG(Eph(theta,phi)))**2)
c
c Radiation Intensity
c
        Radint(theta,phi)=sqrt(ETmag(theta,phi)**2
     &+EPmag(theta,phi)**2)
        ETmag(theta,phi)=20*log10(ETmag(theta,phi)/10511.13)+26.12
        EPmag(theta,phi)=20*log10(EPmag(theta,phi)/10511.13)+26.12
        write (2,*) phi,ETmag(theta,phi),EPmag(theta,phi),
     &Radint(theta,phi)
40   continue
     stop
     end
```

REFERENCES

[1] Copeland, J.R. and N.J. Robertson, " *Antennafiers and Antennaverters* ", Electronics, vol. 34, pp. 68-71, October 1961.

[2] Copeland, J.R., Robertson, W.J., and R.G. Verstraete, "*Antennafier Arrays* ", IEEE Trans. Antennas and Propagation, pp. 227 -233, March 1964.

[3] Fujimoto, K., " *Tunnel-Diode-Loaded Dipole Antenna* ", IEEE Trans. on Aerospace and Navigational Electronics, vol. ANE - 2, pp. 297-307, April 1964.

[4] Fujimoto, K., " *Active Antennas: Tunnel-Diode-Loaded Dipoles* ", Proc. of the IEEE, pp. 174, February 1965.

[5] Thomas, H.J., Fudge, D.L. and G. Morris, " *Gunn Source Integrated with Microstrip Patch* ", Microwaves & RF, pp. 87-88, February 1985.

[6] Perkins, T.O., " *Active Microstrip Circular Patch Antenna* ", Microwave Journal, Vol. 30, pp. 109-117, March 1987.

[7] Hummer, K.A. and K. Chang, " *Microstrip Active Antennas and Arrays* ", IEEE MTT-S Digest, JJ-4 pp. 963-965, 1988.

[8] Chang, K., Hummer, K.A. and J.L. Klein, " *Experiments on Injection Locking of Active Antenna Elements for Active Phased Arrays and Spatial Power Combiners* ", IEEE Trans. on Microwave Theory and Techniques, Vol. 37, No. 7, pp. 1078-1084, July 1989.

[9] Lam, W.W., Ngan, Y.C., and Y. Saito, " *Millimeter-wave Active Patch Antenna* ", IEEE Antenna and Propagation Symposium, pp. 791-794, 1990.

[10] Chang, K., Hummer, K.A. and G.K. Gopalakrishnan, " *Active Radiating Element using FET Source Integrated with Microstrip Patch Antenna* ", Electronics Letters, vol. 24, No. 21, pp. 1347-1348, October 13, 1988.

[11] York, R.A., Martinez, R.D., and R.C. Compton, " *Active Patch Antenna Element for Array Applications* ", Electronics Letters, vol. 26, No. 7, pp. 494-495, March 29, 1990.

[12] Wu, X. D., Leverich, K., and K. Chang, " *Novel FET Active Patch Antenna* ", Electronics Letters, vol. 28, No. 28, pp.1853-1854, September 24, 1992.

[13] Leverich, K.,Wu, X. D., and K. Chang, " *New FET Active Patch Antenna* ", Electronics Letters, vol. 28, No. 24, pp.2239-2240, November 19 1992.

[14] Wu, X. D., and K. Chang, " *Compact Wideband Integrated Active Slot Antenna Amplifier* ", Electronics Letters, vol. 29, No. 5, pp.496-497, March 4, 1993

[15] Robert, B., Razban, T., and A. Papiernik, " *Compact Amplifier Integration in Square Patch Antenna* ", Electronics Letters, vol. 28, No. 19, pp.1808-1810, September 10, 1992.

[16] Birkeland, J. and T. Itoh, " *Planar FET Oscillators using Periodic Microstrip Patch Antennas* ", IEEE Trans. on Microwave Theory and Techniques, Vol.37, No. 8, pp. 1232-1236, August 1989.

[17] Birkeland, J. and T. Itoh, " *FET - Based Planar Circuits for Quasi-Optical Sources and Transceivers* ", IEEE Trans. on Microwave Theory and Techniques, vol. 37, No. 9, pp. 1452 - 1459, September 1989.

[18] Birkeland, J. and T. Itoh, " *Quasi-Optical Planar FET Transceiver Modules* ", IEEE MTT-S Digest, B-2, pp. 119 - 122, 1989.

[19] Stephan, K.D. and T. Itoh, " *Recent Efforts on Planar Components for Active Quasi-Optical Applications* ", IEEE MTT-S Digest, LL-2, pp. 1205-1208, 1990.

[20] Hwang, V.D. and T. Itoh, " *Quasi-Optical HEMT and MESFET Self-Oscillating Mixers* ", IEEE Trans. on Microwave Theory and Techniques, Vol. 36, No. 12, pp. 1701-1705, December 1988.

[21] Shen, Y. et al., " *Active Radiating Oscillator using a Reflection Amplifier Module* ", Electronics Letters, Vol. 28, No. 11, pp. 991-992, May 21, 1992.

[22] An, H. et al., " *Broadband Active Microstrip Array Elements* ", Electronics Letters, Vol. 28, No. 25, pp. 2277-2279, December 03, 1992.

[23] Avitable, G.F. et al., " *Two-Port Active Coupled Microstrip Antenna* ", Electronics Letters, Vol. 28, No. 11, pp. 991-992, May 21, 1992.

[24] Roy, L., Stubbs, M.G. and J. Wight, " *A 30 GHz, HEMT, Active Antenna Structure in MMIC Technology* ", European Microwave Conference, 1992.

[25] Kawasaki, S., and T. Itoh, " *A Slot Antenna with Electronically Tunable Length* ", IEEE Antenna and Propagation Symposium, pp. 130-133, 1991.

[26] Kawasaki, S., and T. Itoh, " *Electronically and Optically Controlled Active Integrated Antenna* ", Proc. of the International Symposium on Antennas and Propagation, (ISAP), pp. 821-824, 1992.

[27] Birkeland, J. and T. Itoh, " *Spatial Power Combining using Push-Pull Fet Oscillators with Microstrip Patch Resonators* ", IEEE MTT-S Digest, LL-5, pp.1217-1220, 1990.

[28] Mortazawi, A. and T. Itoh, " *A Periodic Second Harmonic Spatial Power Combining Oscillator* ", IEEE MTT-S Digest, LL-4, pp. 1213-1216, 1990.

[29] Hall, P.S., " *Microstrip Active Patch Phased Array* ", Proc. of the International Symposium on Antennas and Propagation, (ISAP), pp. 1125-1128, 1992.

[30] Hall, P.S., and P.M. Haskins, " *Microstrip Active Patch Array with Beam Scanning*", Electronics Letters, Vol. 28, No. 22, pp. 2056-2057, October 22, 1992.

[31] Navarro, J.A., and K. Chang, " *Electronic Beam Steering of Active Antenna Arrays* ", Electronics Letters, Vol. 29, No. 3, pp. 302-304, February 4, 1993.

[32] James, J.R., Evans, G.D., and A. Fray, " *Beam Scanning Microstrip Arrays using Diodes* ", IEE Proceedings-H, Vol. 140, No. 1, pp. 43-51, February, 1993.

[33] Hunton, J.K., " *The Design of an Active Loop Antenna by Optimization* ", Microwave Journal, pp. 84-103, February 1992.

[34] Itoh, T., " *Active Antennas* ", Journees Internationales de Nice sur les Antennas, pp. 435-438, 1990.

[35] York, R.A. and R.C. Comptom, " *Dual-Device Active Patch Antenna with Improved Radiation Characteristics* ", Electronics Letters, Vol. 28, No. 11, pp. 1019-1021, May 21, 1992.

[36] Camilleri, N. and B. Bayraktaroglu, " *Monolithic Millimeter-wave IMPATT Oscillator and Active Antenna* ", IEEE MTT-S Digest, JJ-2, pp. 955-958, 1988.

[37] Chang, K., " *Integrated Circuit Active Antenna Elements for Monolithic Implementation* ", SPIE, Vol. 1475, pp. 164-174, 1991.

[38] Navarro, J.A., Hummer, K.A. and K. Chang, "*Active Integrated Antenna Elements* ", Microwave Journal, pp. 115-126, January 1991.

[39] Fusco, V.F. and H.O. Burns, " *Synthesis Procedure for Active Integrated Radiating Elements* ", Electronics Letters, Vol. 26, No. 4, pp. 263-264, February 15, 1990.

[40] Fusco, V.F., " *Series Feedback Integrated Active Microstrip Antenna Synthesis and Characterisation* ", Electronics Letters, Vol. 28, No.1, pp.89-91, January 02, 1992.

[41] Gillard, R. et al., " *Rigorous Modelling of Receiving Active Microstrip Antenna* ", Electronics Letters, Vol. 27, No. 25, pp. 2357-2359, December 05, 1991.

[42] Hall, P.S., " *Analysis of Radiation from Active Microstrip Patch Antennas* ", Journees Internationales de Nice sur les Antennas, pp. 446-449, 1990.

[43] Hall, P.S., " *Analysis of Radiation from Active Microstrip Antenns* ", Electronics Letters, Vol. 29, No. 1, pp. 127-129, January 7, 1993.

[44] Roscoe, D.J., A. Ittipiboon and L.Shafai, " *The Application of a Circuit Simulator to the Design and Analysis of Passive and Active Microstrip Antennas* ", IEEE AP-S/URSI International Symposium, pp. 1439-1442, Chicago, Illinois, July 1992.

[45] Mailloux, R. J., "*Phased Array Theory and Technology*", Proceedings of the IEEE, Vol. 70, No. 3, pp 246 - 291, March 1982.

[46] Stark, L., " *Microwave Theory of Phased- Array Antennas - A Review* ", Proc. IEEE, Vol. 62, No. 12, pp. 1661-1703, December 1974.

[47] Pozar, D.M. and D.H. Schaubert, "*Comparison of Architectures for Monolithic Phased Array Antennas*", Microwave Journal, pp 93 - 109, March 1986.

[48] Forrest, J.R., "*Assessing Antennas for Small Satcom Terminals*", Microwave System News, pp.77-101, October 1981.

[49] Poirier, J.L. " *An Analysis of Simplified Feed Architectures for MMIC T/R Module Arrays* ", Rome Air Development Center, February 1987, RADC-TR-86-236.

[50] Stutzman, W., L. and G. A. Thielf, "*Antenna Theory and Design*", (Toronto: John Wiley and Sons, Inc., 1987).

[51] Burke, G.J. et al., "*Numerical Electromagnetics Code (NEC)-Method of Moments* ", Lawrence Livermore Laboratory, January 1981.

[52] EEsof, Inc., " *Libra* ", copyright 1987.

[53] Compact Software, Inc., " *Harmonica* ", copyright 1987.

[54] EEsof, Inc., " *EMSim* ", copyright 1991.

[55] Sonnet Software, Inc., " *Electromagnetic Microstrip Design Software* ", copyright 1989.

[56] Hewlett-Packard Company, "*High Frequency Structure Simulator*", copyright 1990.

[57] Chow, Y.L. and I.N. El-Belery, " *An Approximate Dynamic Spatial Green's Function for Microstriplines* ", IEEE Trans. Microwave Theory and Tech., Vol. MTT-26, No. 12, pp. 978-983, December 1978.

[58] Chow, Y.L., " *An Approximate Dynamic Green's Function in Three Dimensions for Finite Length Microstripline* " IEEE Trans. Microwave Theory and Tech., Vol. MTT-28, No. 4, pp. 393-397, April 1980.

[59] Silvester, P., " *TEM Wave Properties of Microstrip Transmission Lines* ", Proc. IEE, Vol. 115, pp. 43-48, January 1968.

[60] Chow, Y.L. et al., " *A Closed-Form Spatial Green's Function for the Thick Microstrip Substrate* ", IEEE Trans. Microwave Theory and Tech., Vol. 39, No. 3, March 1991.

[61] Yang, J.J., Chow, Y.L. and D.G. Fang, " *Discrete Complex Images of a Three-Dimensional Dipole Above and Within a Lossy Ground* ", IEE Proceedings-H, Vol. 138, No. 4, August 1991.

[62] Shubair, R.M., Chow, Y.L. and J.J. Yang, " *A Full Wave Complex Image Solution of Horizontal Electric Dipoles in a Thick Dielectric Sheet* ", IEEE Antenna and Propagation Symposium, pp. 1372-1375, 1991.

[63] Bannister, P.R., "*Applications of Complex Image Theory*", Radio Science, Vol. 21, No. 4, pp. 605-616, July 1986.

[64] Wait, J. R., " *Complex Image Theory - Revisited*", URSI, The Radio Scientist, Vol. 2, No. 3, pp. 44-47, July 1991.

[65] Mahmoud, S.F. and A.D. Metwally, "*New Image Representation for Dipoles Near a Dissipative Earth 1. Discrete Images*", Radio Science, Vol. 16, No. 6, pp. 1271-1275, November 1981.

[66] Mohsen, A., "*On the Evaluation of Sommerfeld Integrals*", IEE Proceedings, Vol. 129, Pt. H, No. 4, pp. 177-182, August 1982.

[67] Hamming, R.W., "*Numerical Methods for Scientists and Engineers*", Dover Publications Inc., New York, pp. 620-622,1973.,.

[68] Omar, A.A., and Y.L. Chow, "*Complex Image Green's Functions for Coplanar Waveguides*", IEEE AP-S/URSI International Symposium, Chicago, USA, pp. 1496-1499, July 1992.

[69] Omar, A.A., and Y.L. Chow, "*Effect of Upper and Lower Shielding on the Elimination of the Slot-Line Mode in Coplanar Waveguides*", IEEE AP-S/URSI International Symposium, Chicago, USA, pp. 1508-1511, July 1992.

[70] Fang, D., Yang, J. and G. Delisle , "*Discrete Image Theory for Horizontal Electric Dipoles in a Multilayered Medium*", IEE Proceedings, Vol. 135, Pt. H, No. 5, pp. 297-303, October 1988.

[71] Harrington, R.F., " *Field Computation by Moment Methods* ", New York, MacMillan, pp.62-81, 1968.

[72] Harrington, R.F., " *Time-Harmonic Electromagnetic Fields* ", McGraw-Hill, 1961.

[73] Ragheb, H.A. and L. Shafai, " *Analysis of Arbitrary Shape Printed Line Microstrip Antennas* ", IEEE Trans. on Antennas and Propogation, Vol. 38, No. 2, pp. 269-274, February 1990.

[74] Ragheb, H.A. and L. Shafai, " *Radiation Characteristics of Curved Microstrip Line Antennas* ", Symposium on Antenna Technology and Applied Electromagnetics (ANTEM), 1988, Winnipeg, Manitoba, August 1988.

[75] Wait, J.R., " *Electromagnetic Radiation from Cylindrical Structures* ", Pergamon Press Inc., New York, N.Y. 1959.

[76] Stutzman, W., and G. Thiele,"*Antenna Theory and Design*", John Wiley and Sons Inc., 1981, pp. 334.

[77] Roscoe, D.J., " *A Study of Compatible Radiating Elements for MMIC/MHMIC Applications* ", M.Sc. Thesis, University of Manitoba, Winnipeg, Manitoba, 1989.

[78] Hall, P.S., " *Microstrip Linear Array with Polarisation Control* ", IEE Proc., Vol. 130, Pt. H., No. 3, pp. 215-224, April 1983.

[79] Carlsan, A.B., "*Communication Systems, an Introduction to Signal and Noise in Electrical Communications*", McGraw-Hill Book Company, 1986, pp. 425.

[80] Rudge, A.W., et al., "*The Handbook of Antenna Design*", IEE, Peter Peregrinus Ltd., 1983, Vol. 2, pp.92.

[81] Shafai, L. and K. Antoszkiewicz, " *Circular Polarized Antennas Employing Linearly Polarized Radiators* ", ANTEM '88, Winnipeg, Manitoba, 1988.

[82] Freeman, R.L., "*Reference Manual for Telecommunications Engineering*", John Wiley & Sons, Inc., 1985, pp.774.

[83] Kraus, J.D., "*Radio Astronomy*", McGraw-Hill Book Company, 1966, pp.98.

[84] U.S. patent filed, " *Active Integrated Microstrip Antennas* ", U.S. serial #07/718,450.

[85] Balanis, C. A., " *Antenna Theory and Design* ", Harper and Row, Publishers Inc., 1982.

[86] Rudge, A. W., et al., " *The Handbook of Antenna Design* ", IEE, Peter Peregrinus Ltd., pp. 147-151, 1983.

[87] Johnson, R. C. and H. Jasik, " *Antenna Engineering Handbook* ", McGraw-Hill Book Company, pp.20.15-20.21, 1984.

[88] Moheb, H., D.J. Roscoe, and L. Shafai, " *Feasibility Syudy on S-Band Phased Array Antenna and Preliminary Design*", prepared for Satlantic Inc., April 1992.

[89] Berini, P., D.J. Roscoe, and M.Cuhaci, " *MHMIC Active Microstrip Travelling Wave Antenna*", Technical Report CRC-RP-92-001, Department of Communications, May 1993.

[90] Shafai, L., "*Scanning Properties of Circularly Polarized Microstrip Antennas*", Symposium on Antenna Technology and Applied Electromagnetics (ANTEM), 1988, Winnipeg, Manitoba, August 1988.

[91] Shafai, L., "*Linear-Sum Mode Arrays and Beam Forming*", Symposium on Antenna Technology and Applied Electromagnetics (ANTEM), 1992, Winnipeg, Manitoba, August 1992.

[92] Roscoe, D.J., A. Ittipiboon, L. Shafai and M. Cuhaci "*Noise Analysis of an Integrated Travelling Wave Antenna*", Elect. Let., Vol. 29, No. 06, March 1993, pp544-545.13.

[93] Roscoe, D.J., A. Ittipiboon, L. Shafai and M.Cuhaci, "*Noise Model of Series Distributed Active Antennas*", IEEE AP-S/URSI International Symposium, Ann Arbor, Michigan, June 1993.

[94] Roscoe, D.J., A. Ittipiboon and L. Shafai, " *The Application of Active Integrated Antennas to Phased Arrays* ", ISAP (International Symposium on Antennas and Propagation), pp. 485-488, Sappro, Japan, Sept. 1992.

[95] Roscoe, D.J., A. Ittipiboon and L. Shafai, " *Pattern Reconfiguration with an Active Integrated Antenna* ", ANTEM - Symposium on Antenna Technology and Applied Electromagnetics, pp. 643-647, Winnipeg, Manitoba, August 1992.

[96] Roscoe, D.J., A. Ittipiboon and L.Shafai, " *The Application of a Circuit Simulator to the Design and Analysis of Passive and Active Microstrip Antennas* ", IEEE AP-S/URSI International Symposium, pp. 1439-1442, Chicago, Illinois, July 1992.

[97] Shafai, L. and D.J. Roscoe, "*Survey of L-Band Antenna Technologies for Digital Radio Reception*", Final Report, DSS Contract 36001-1-3547/01-ST, Dept. of Communications, September 1991.

[98] Roscoe, D.J., A. Ittipiboon and L. Shafai, " *Antenna Performance of an Active Integrated Antenna*", Progress in Electromagnetics Research Symposium (PIERS), July 1991, Cambridge, Massachusetts.

[99] Roscoe, D.J., A. Ittipiboon and L. Shafai, " *The Development of an Active Integrated Antenna*", IEEE AP-S/URSI International Symposium, London, Ontario, June 1991.